

Influence of magnesium-based material degradation on cancer hallmarks of an osteosarcoma-fibroblast coculture

Dissertation zur Erlangung des Doktorgrades
an der Fakultät für Mathematik, Informatik und
Naturwissenschaften
Fachbereich Chemie
der Universität Hamburg

vorgelegt von Philipp Globig

Hamburg, 2021

Erstgutachter: Prof. Dr. Hartmut Schlüter
Zweitgutachterin: Prof. Dr. Regine Willumeit-Römer

Prüfungskomitee: Prof. Dr. Hartmut Schlüter
Prof. Dr. Regine Willumeit-Römer
Dr. Maria Riedner
Dr. Markus Perbandt
Dr. Thomas Hackl

Tag der mündlichen Prüfung: 26.11.2021
Druckfreigabe: 03.12.2021

Diese Arbeit wurde in der Zeit von Januar 2018 bis einschließlich März 2021 an der Helmholtz-Zentrum hereon GmbH (bis 30.03.2021 unter der Firmierung Helmholtz-Zentrum Geesthacht Zentrum für Material- und Küstenforschung GmbH), Institut für Metallische Biomaterialien in der Abteilung für Biologische Charakterisierung unter der Anleitung von Frau Prof. Dr. Regine Willumeit-Römer angefertigt.

Die Arbeit wurde im Rahmen einer Helmholtz-RSF Joint Research Group „Materials based on magnesium alloys for bioresorbable implants with anti-tumor activity“ (Helmholtz-Russian Science Foundation Joint Research Groups 0025) angefertigt. Auf Seiten des Helmholtz-Zentrums gab es zwei Wissenschaftler, die dieses Projekt bearbeitet haben. Khausik Narasimhan war für die Produktion der schnell degradierenden Mg-6Ag Proben aus langsam degradierenden Materialien verantwortlich. Teil dieser Arbeit war dann unter anderem die Bestimmung der mittleren Degradationsgeschwindigkeit dieser Materialien und die Evaluation des Einflusses auf die Zellviabilität.

Abstract

Conventional osteosarcoma therapies include surgery combined or not with different chemotherapies, but all approaches failed to increase the survival rates over the past 20 years. Therefore, it is not surprising that an efficient targeted approach is demanded to increase the therapy outcome and ameliorate the patients' quality of life during the treatment time. A novel approach combining temporary bone replacement after surgery and targeted cancer therapy for residual cancer cells may be degradable and biocompatible magnesium (Mg)-based materials. Those materials are already in successful clinical use for orthopedic applications for small bone fractures. Owing to their degradability and degradation associated surface-near effects such as hydrogen gas evolution and increasing Mg concentration, pH and osmolality, Mg-based materials are also discussed for cancer therapy. *In vitro* studies that aim to investigate such anticancer activity should be performed with tumor models that can mimic the complex communication of cancer and stromal cells in the tumor microenvironment. Therefore, tumor models are needed that are more complex than cancer cell monocultures to reflect *in vivo* situations better.

This thesis aims to increase the knowledge of the influence of Mg-based materials on cancer cells in a complex environment. For this purpose, fluorescently labeled osteosarcoma cells and fibroblasts were directly seeded on degrading Mg and Mg-6Ag surfaces as a coculture in a 1:1 cell ratio (cancer to healthy cell ratio). In the first part of this work, the degradation associated surface-near effects (pH, osmolality, Mg and silver (Ag) ions) and the cytocompatibility of slow-degrading Mg and Mg-6Ag were analyzed. The cells were visualized on the material by fluorescence microscopy and counted in order to evaluate the cytocompatibility. This revealed constantly remaining cancer cell numbers, while healthy cell numbers (fibroblasts) increased on Mg and Mg-6Ag, which was Mg degradation-dependent. This phenomenon was traced back to a diminished proliferation since the slow degrading materials (Mg, Mg-6Ag) did not show a cytotoxic potential.

In the second part of the thesis, the osteosarcoma-fibroblast coculture was used to investigate the influence of Mg-based materials and their degradation-related effects on selected cancer hallmarks such as sustaining proliferative signaling, activating invasion and metastases, avoiding immune destruction, and inducing angiogenesis. Mg and Mg-6Ag induced tumor-specific proliferation inhibition, decreased cell migration and invasion, and reduce cancer-induced angiogenesis. The Mg degradation-dependent increase in pH and osmolality were identified as critical Mg degradation-dependent surface-near effects that inhibited cell proliferation tumor-specifically and reduced cell migration.

In the last part, the degradation rate, pH and osmolality of T6 heat-treated Mg-6Ag were analyzed and tailored to a degradation rate range between 1.0-2.4 mm/a. The materials within this degradation rate range caused - a decrease in overall cell number with increasing degradation rate indicating scalable cell effects with tailored degradation rates. However, this preliminary analysis also showed a higher cancer cell sensitivity to the environmental changes during Mg-6Ag degradation compared to the healthy cells.

This thesis showed that already slow-degrading Mg-based materials exert anticancer activity *in vitro*. With different material treatments, the degradation rate can be tailored to the application requirements, and therefore Mg-based materials may be promising candidates for osteosarcoma therapy.

Zusammenfassung

Osteosarkome werden herkömmlicherweise mittels Operation und dem Einsatz verschiedener Chemotherapeutika behandelt, was jedoch die Überlebenswahrscheinlichkeit der Patienten in den letzten 20 Jahren nicht wesentlich verbesserte. Das erfordert einen gezielten Ansatz, um den Therapieerfolg zu erhöhen und die Lebensqualität der Patienten während der Behandlungsdauer zu verbessern. Ein neuartiger Ansatz könnten abbaubare, biokompatible Magnesium (Mg)-basierte Materialien sein, die eine Kombination aus vorübergehenden Knochenersatz und gezielter Tumorbehandlung sein können. Diese Materialien werden bereits erfolgreich in der Orthopädie für die Knochenheilung kleiner Knochenbrüche eingesetzt. Mg-basierte Materialien sind auch Kandidaten für die Krebstherapie. Ihre Degradierbarkeit und damit verbundene oberflächennahe Effekte wie der Freisetzung von Wasserstoffgas und Anstieg der Mg Konzentration, des pH-Werts und der Osmolalität sind vielversprechende Eigenschaften. Um die krebsbekämpfende Aktivität Mg-basierter Materialien zu untersuchen, sollten geeignete Tumormodelle in *in vitro* Studien verwendet werden, welche die komplexe Kommunikation von Krebs- und Gewebszellen in der Tumorumgebung imitieren. Dafür werden Tumormodelle benötigt, welche komplexer sind als herkömmliche Krebszellmonokulturen, um *in vivo* Gegebenheiten besser widerzuspiegeln.

Diese Arbeit soll das Wissen über den Einfluss von Mg-basierten Materialien auf Krebszellen in einer komplexen Umgebung erhöhen. Dafür wurden Fluoreszenz-markierte Osteosarkomzellen und Fibroblasten als Kokultur in einem Verhältnis von 1:1 direkt auf die Materialoberfläche von abbaubarem Mg und Mg-6Ag gesät. Im ersten Teil der Arbeit wurden die Degradations-assoziierten oberflächennahen Effekte (pH-Wert, Osmolalität, Mg und Ag) sowie die Zytokompatibilität langsam degradierender Mg und Mg-6Ag Proben analysiert. Die Zellen wurden auf den Materialoberflächen mittels Fluoreszenzmikroskopie visualisiert und gezählt. Dies ergab konstant bleibende Krebszellzahlen, währenddessen die Zellzahlen der Fibroblasten auf Mg und Mg-6Ag anstiegen, was degradationsabhängig war. Dieses Phänomen wurde auf eine verminderte Zellproliferation zurückgeführt, da die langsam degradierenden Mg und Mg-6Ag Materialien keine Zytotoxizität zeigten.

Im zweiten Teil der Dissertation wurde die Kokultur verwendet, um Effekte der Mg-basierten Materialien auf ausgewählte Krebscharakteristika u.A. die Aufrechterhaltung der proliferativen Signalübertragung zu untersuchen. Mg und Mg-6Ag führten zu einer tumorspezifischen Hemmung der Proliferation der Krebszellen. Dies war verbunden mit einer verminderten Zellmigration und -invasion und verringerter tumorinduzierter Angiogenese. Der Mg degradationsabhängige Anstieg des pH-Wertes und der Osmolalität wurden als die oberflächennahen Effekte identifiziert, die die Zellproliferation tumorspezifisch hemmten und die Zellmigration reduzierten.

Weiterhin wurden die Degradationsrate, der pH-Wert und die Osmolalität von T6 behandelten Mg-6Ag Proben analysiert und an eine Degradationsspanne zwischen 1,0-2,4 mm/a angepasst. Innerhalb dieser Spanne induzierten Materialien einen Rückgang der Zellzahl mit steigender Degradationsrate, was auf skalierbare Zelleffekte mit angepassten Degradationsraten hinwies. Dennoch zeigten auch diese vorläufigen Analysen, dass die Krebszellen sensitiver gegenüber Umgebungsänderung durch Mg-6Ag Degradation waren als die gesunden Zellen.

Es konnte gezeigt werden, dass bereits langsam degradierende Mg-basierte Materialien eine krebsbekämpfende Aktivität *in vitro* aufweisen. Durch verschiedene Materialbehandlungen kann die Degradationsrate an die Erfordernisse der geplanten Anwendung angepasst werden, weshalb Mg-basierte Materialien vielversprechende Kandidaten für eine neuartige Osteosarkomtherapie darstellen.

List of publications

Globig, P.; Willumeit-Römer, R.; Martini, F.; Mazzoni, E.; Luthringer-Feyerabend, B.J.C. Optimizing an Osteosarcoma-Fibroblast Coculture Model to Study Antitumoral Activity of Magnesium-Based Biomaterials. *Int. J. Mol. Sci.* 2020, 21, 5099. <https://doi.org/10.3390/ijms21145099>

Impact factor: 4.556 (2019)

Table of content

Abstract	I
Zusammenfassung	II
List of publications	III
Table of content	IV
List of abbreviations	VI
1 Introduction	1
1.1 Mg-based materials in biomedicine	1
1.2 Influence of Mg-based material degradation products on cancer cells.....	2
1.3 Cancer and conventional cancer therapy	4
1.4 Cancer biology	6
1.4.1 Cancer Hallmarks.....	6
1.4.2 Tumor microenvironment/cancer associated cells	12
2 Motivation and objectives	14
3 Materials and methods	15
3.1 Production of Mg-based materials	15
3.2 Cell culture and proliferation	16
3.3 In vitro tests.....	17
3.3.1 Degradation rate of Mg-based materials.....	17
3.3.2 Biological tests	20
3.4 Cytotoxicity tests of Mg-based materials	20
3.5 Coculture proliferation with Mg-based materials	23
3.5.1 Proliferation status of the coculture	23
3.5.2 Impact of Mg degradation on cell proliferation with special focus on varying selected surface-near effects.....	25
3.6 Analysis of the metastatic potential of the coculture	26
3.6.1 Cell movements and invasion-related cytokines	26
3.6.2 Analysis of cell migration under specific surface-near effects	28
3.7 NK cell-coculture interaction with Mg-based materials.....	29
3.7.1 NK cell activation during Mg degradation	29
3.8 Analysis of cancer cell induced angiogenesis.....	29
3.8.1 Preparation of conditioned media	29
3.8.2 Endothelial cell permeability and proliferation - VEGF content	30
3.8.3 Endothelial cell migration and tube formation	31
3.9 Statistical analyses.....	32
4 Results	33

4.1	Characterization of an osteosarcoma-fibroblast coculture on slow degrading Mg-based materials	33
4.2	Cytotoxicity of Mg-based materials	36
4.3	Influence of Mg-based materials on cancer cell proliferation	39
4.3.1	Visualization of proliferation marker Ki-67	39
4.3.2	Investigation of the cancer cell proliferation inhibition signaling pathway	41
4.3.3	Studying the influence of surface-near effects of Mg degradation on cell proliferation	43
4.4	Influence of Mg-based materials on cancer cell migration and metastases	46
4.4.1	Determination of cell migration and invasion	46
4.4.2	Quantification of metastases-associated cytokines	49
4.4.3	Studying the influence of single parameters of Mg degradation on cell migration	51
4.5	Influence of Mg-based materials on cancer cell immune evasion	53
4.5.1	Natural killer cells affecting the coculture cell ratio	53
4.5.2	Quantification of natural killer cell activation	54
4.6	Influence of Mg-based materials on cancer cell induced angiogenesis.....	57
4.6.1	Conditioned media used for HUVEC incubation	57
4.6.2	Endothelial cell permeability and proliferation - VEGF expression.....	58
4.6.3	Endothelial cell migration	60
4.6.4	Formation of an endothelial cell network	62
4.7	Degradation tailoring of Mg-6Ag to adjust anticancer activity.....	63
5	Discussion.....	66
5.1	Suitable model for testing anticancer activity of Mg-based materials	66
5.2	Cytotoxic potential of Mg-based materials	67
5.3	Influence of slow degrading material on cancer cell hallmarks	68
5.4	Degradation tailoring for anticancer applications	75
5.5	Suitability of Mg-based materials for osteosarcoma therapy.....	75
6	Conclusion.....	77
	References.....	78
	List of Figures.....	96
	List of Tables	98
	Appendix.....	99
	Danksagung.....	107
	Eidesstattliche Versicherung / Declaration on oath.....	108

List of abbreviations

AAS	atomic absorption spectroscopy
ADP	adenosine diphosphate
AgNP	silver nanoparticles
α -MEM	alpha minimal essential medium
α -SMA	alpha smooth muscle actin
ATP	adenosine triphosphate
CAF	cancer-associated fibroblasts
CC	coculture
CDK	cyclin-dependent kinase
cLSM	confocal laser scanning microscope
CTC	circulating tumor cell
CTCF	corrected total cell fluorescence
CTFF	corrected total field fluorescence
DAPI	4',6-diamidino-2-phenylindole
DMEM	Dulbecco's Modified Eagle Medium
DNA	deoxyribonucleic acid
DNAM-1	DNAX Accessory Molecule-1
ECGM	endothelial cell growth medium
ECM	extracellular matrix
EDTA	ethylenediaminetetraacetic acid
eGFP	enhanced green fluorescent protein
ELISA	enzyme-linked immunosorbent assay
EMT	endothelial-mesenchymal transition
FBS	fetal bovine serum
FITC	fluorescein isothiocyanate
FP602	fluorescent protein 602
h	hour
HIF	hypoxia inducible factor
HUVEC	human umbilical vein endothelial cell
ICP-MS	inductively-coupled plasma mass spectrometry
IFN- γ	interferon gamma
I κ B	nuclear factor of kappa light polypeptide gene enhancer in B-cells inhibitor, alpha
IL	interleukin

LDH	lactate dehydrogenase
LOD	limit of detection
LOQ	limit of quantification
MAPK	mitogen activated protein kinase
MCF	monoculture RF Fibroblasts
MCS	monoculture Saos-eGFP
MHC	major histocompatibility complex
min	minute
MMC	mitomycin c
MMP	matrix metalloproteinase
NF- κ B	nuclear factor 'kappa-light-chain-enhancer' of activated B-cells
NK	natural killer cell
NKG2D	natural killer group 2D
NO	nitric oxide
PEG	polyethylene glycol
PERK	protein kinase RNA-like endoplasmic reticulum kinase
pH _e	extracellular pH
pH _i	intracellular pH
RF	red fluorescent
ROS	reactive oxygen species
TAM	tumor-associated macrophages
TGF- β	tumor growth factor beta
TIMP	tissue inhibitor of metalloproteinase
TMB	tetramethylbenzidine
TME	tumor microenvironment
TNF- α	tumor necrosis factor alpha
VEGF	vascular endothelial growth factor

1 Introduction

1.1 Mg-based materials in biomedicine

Due to their advantageous biocompatible and biodegradable properties, Mg-based materials get increasing attention for biomedical applications. Their biocompatibility arises from the natural occurrence of Mg in the human body. Mg^{2+} is the second most abundant intracellular cation after potassium and is involved in multiple processes of cell physiology. These include cell proliferation, metabolism, ion channel activity and various enzyme-dependent reactions as Mg acts as a cofactor or activator of more than 600 enzymes [1-4]. Mg enters the body through dietary intake and accounts for approximately 24 g in an average adult [5,6]. Over half of the total Mg content is stored in the bone [5,7], whereas the rest is located in the muscle, soft tissue and 1 % in serum [8-10]. Mg in serum can be split into free/ionized (55-70 %), protein bound (20-30 %), and anion complexed (5-15 %) forms further [9,11]. The total intracellular Mg concentration varies between 5-30 mM dependent on the tissue type [4], while the serum concentration ranges between 0.7-1.2 mM [12]. Due to its important biological function, a highly efficient regulation system is needed to maintain the Mg concentration in a physiological range. If Mg intake and following the Mg serum level is temporarily too low, Mg can partly be released from the large storage in the bone or reabsorbed in the intestine and kidney [1,13]. With too high Mg concentrations, as a result of Mg rich diet, Mg is excreted via the urine, indicating that the kidney plays a major role in Mg homeostasis [1,2]. Although it was speculated that Mg degradation might pathologically increase the Mg concentration (hypermagnesemia) in patients with renal failure, Wang *et al.* [14] could show that Mg levels in serum, urine and feces did not significantly changed in a chronic renal failure rat model after Mg alloy implantation.

Owing to their ability to degrade in fluids, Mg-based materials are especially interesting for the use as a temporary implant material. This temporary use may be desired in cardiovascular or orthopedic applications. There, the supportive function of Mg in wound healing or tissue regeneration is only needed temporarily and a second surgery would be no longer necessary [15,16].

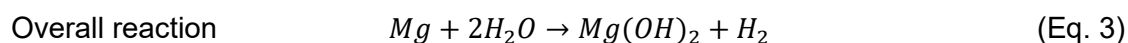
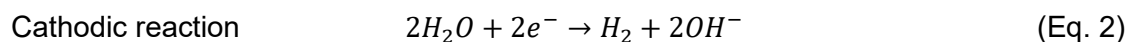
In fact, the earliest use of Mg as a biomaterial dates back to 1878, when Edward C. Huse applied Mg wired to stop bleeding in surgery [17]. Later, Mg experienced further research as a biomaterial by the work of Erwin Payr [18], who employed Mg for various surgical applications. While suturing of organs with Mg was proven to be quiet effective, Mg in orthopedic applications implanted as pins or nails remained unsuccessful due to missing understanding of mechanical properties and corrosion [19]. This changed in the following decades based on novel studies [20-24]. Mg-based materials got increasing attention due to their osteopromotive properties [20-23] and comparable mechanical characteristics to that of bone [24]. These characteristics can reduce stress shielding effects after implantation and are advantageous over conventional orthopedic implants made from titanium, stainless steel and cobalt-chromium materials [24]. Owing to their low thrombogenic properties, Mg-based materials are also attractive for cardiovascular applications as stents [25].

Mg-based implants are already in clinical use. This includes screws such as the MgYReZr (“MAGNEZIX®”) screw fabricated by Syntellix AG [26,27], the Mg-Ca-Zn screw “K-MET” (Korea U&I company) for radius fracture repair [28], or the Mg-based stent “Magmaris” from Biotronik AG [29]. With growing knowledge on the corrosion behavior of Mg-based materials, the predictability of the degradation and safety of Mg implants will be enhanced. This may lead to a growing number of approved and clinically used Mg-based implants, which are not limited to screws and stents. In fact, Mg-based materials can be attractive as a novel cancer therapy

approach, especially in excised bone tumors. As such, those materials can combine bone growth and healing inducing function with their mechanical properties, which cannot be fulfilled by conventional bone grafts. Mg-based materials already have been tested for anticancer activity [30-32]. In these studies, tumor cell cytotoxicity was shown when bone tumor cells (MG63 and U2OS) were seeded on pure Mg. However, to date, there are no in-depth analysis on the molecular mechanisms how Mg materials exert their observed cytotoxic activity. Those analyses are essential to predict, whether a certain material is effective as cancer therapy. Moreover, the studies on Mg anticancer activity were only conducted with monocultures. Yet, the cancer progression is mainly influenced by the conditions in the tumor microenvironment (TME) and interaction with stromal cells, as described in chapter 1.4.2. Therefore, the inclusion of stromal cells in the tumor model e.g., as a tumor-stromal cell coculture, is indispensable.

1.2 Influence of Mg-based material degradation products on cancer cells

The desired application and implantation site dictate the degradation rate of Mg-based material. Different treatments can be applied to tailor this degradation rate and alter the degradation-dependent effects. Therefore, the influence of the individual degradation-dependent effects on the cancer cells has to be understood and is discussed in this chapter. The degradation of Mg-based materials in aqueous solution leads to the formation of magnesium hydroxide ($Mg(OH)_2$) on the surface accompanied with hydrogen gas (H_2) evolution (Eq. 1-3) [33]:



Besides H_2 evolution, $Mg(OH)_2$ dissolves further into $Mg^{2+}+2OH^{-}$ that increases the solution pH, since $Mg(OH)_2$ is only stable at $pH > 8.5$ [34]. With increased ion dissolution the osmolality elevates, which is the molality of osmotically relevant substances e.g., ions, which influence the osmotic pressure. The Mg degradation is additionally influenced by interactions with inorganic ions, organic components, and cells. These interactions represent another broad research field with a growing number of new insights. Despite these interactions, the Mg degradation accompanied surface-near effects (increase of pH and osmolality, constant release of H_2 and Mg, alloying element ions) that can affect cells, remain. The influence of H_2 on cancer cells is not discussed in this work.

Magnesium

The role of Mg in cancer is still ambiguous. Clinical data indicates that Mg deficiency may favor the development of several cancers. At the same time, Mg presence appears to promote cancer growth at an advanced stage [35]. This may be due to its cofactor function for various enzymes. Mg^{2+} stabilizes the deoxyribonucleic acid (DNA) structure and acts as a protection against hydroxyl radicals that can damage the DNA. Moreover, Mg^{2+} reduces the risk of mutations during DNA replication because of its cofactor function in DNA synthesis and proof reading function of the DNA polymerase [36]. Though once a tumor has formed, Mg^{2+} can contribute to its energy metabolism and growth by adenosine triphosphate (ATP) stabilization and ATP hydrolysis to adenosine diphosphate (ADP) with subsequent energy release [37].

Introduction

However, Mg may also exhibit some activity to reduce carcinogenesis. Mg²⁺ also acts as a cofactor for the tumor growth factor- β receptor type II subunit, which phosphorylates and binds to the type I subunit upon ligand binding and activate the whole receptor [38-40]. This may lead to phosphorylation and activation of the SMAD2/SMAD3 complex which translocates in the nucleus and induces the expression of the tissue inhibitor of metalloproteinases 1 (TIMP-1), matrix metalloproteinase (MMP)-2 and to a lesser extent MMP-9, as shown by Kwak *et al.* with human fibrosarcoma cells [41]. The proteinases MMP-2 and MMP-9 were shown to increase tumor invasiveness and metastasis. Yet, the simultaneous presence of TIMP-1 can inhibit their function [41,42]. Similarly, cancer cells can exploit stromal cells such as fibroblast to secrete MMP-2 and MMP-9 [43,44]. However, with Mg being present, the MMP-2 secretion from fibroblasts was shown to be reduced [45]. Moreover, SMAD2/SMAD3 signaling can lead to cyclin-dependent kinase (CDK) inhibitor p21 expression and subsequent proliferation inhibition [46]. Additionally, low Mg concentration has also been associated with increased interleukin 8 (IL)-8 release. An increased IL-8 release in turn is associated with increased proliferation and angiogenesis transduced via mitogen activated protein kinase (MAPK), Src kinase and focal adhesion kinase signaling [47].

Cancer cell induced angiogenesis may also be affected by Mg. An intracellular increase in Mg²⁺ was reported to reduce the nitric oxide (NO) release in endothelial cells [48,49]. NO is associated with increased proliferation and migration of endothelial cells and increased vascular permeability [50,51]. NO itself was also reported to potentially induce expression of the vascular endothelial growth factor (VEGF) during hypoxia, increasing angiogenesis further [52]. However, Bernardini *et al.* [49] reported increased endothelial migration and proliferation with high Mg levels, underlining the ambiguous function of Mg in angiogenesis.

Mg was also shown to affect the interaction of the immune system with the cancer cells [53,54]. Sugimoto *et al.* [53] showed that Mg supplementation reduces the release of proinflammatory cytokines tumor necrosis factor (TNF)- α and IL-6 *in vivo*. This anti-inflammatory activity of Mg was confirmed *in vitro* with decreased cytokine production although the toll-like receptors on monocytes were stimulated. The authors concluded that Mg inhibits the degradation of the nuclear factor of kappa light polypeptide gene enhancer in B-cells inhibitor, alpha (I κ B α) degradation. The factor I κ B α is the inhibitor of the nuclear factor 'kappa-light-chain-enhancer' of activated B-cells (NF- κ B), leading to reduced NF- κ B levels and subsequent cytokine production [53]. Furthermore, Mg deficiency was associated with a decreased expression of the activation receptor natural killer group 2D (NKG2D) on natural killer (NK) cells. With Mg supplementation, the receptor expression was recovered [54]. This has the potential to increase the cytolytic activity of NK cell towards cancer cells.

Alloying element: Silver

Silver (Ag) has previously been associated with antibacterial activity against gram-positive and gram-negative bacteria based on cell wall destruction [55,56]. Such an antibacterial activity can likewise be beneficial for a potential Mg-based material osteosarcoma therapy, as it could prevent excessive immunological reactions or sepsis after surgery and Mg implantation. Nanosilver, in the form of silver nanoparticles (AgNP), has also been linked to increased oxidative stress, impairment of the membrane integrity, cell cycle arrest, DNA damage, and eventually apoptosis induction in cancer cells [57]. While AgNP are known to enter the cell via endocytosis, the exact mechanism of Ag entry is still not very well known. However, a recent report showed an involvement of the voltage-gated potassium channel Kv [58]. Moreover, Ag⁺ in solution quickly binds to other ions such as chloride and sulfide or complexes with thiol groups of proteins in the cell membrane [59], which may hinder cell entry.

Inside the cell, nanosilver dissolves into Ag^+ which initiates the production of reactive oxygen species (ROS) and a subsequent potential damage to DNA and proteins. DNA damages have direct consequences on cell proliferation. The treatment of human glioblastoma cells with nanosilver resulted in a G2/M cell cycle arrest provoked by decreased and inactive forms of cyclin-dependent kinase 1 and cyclin B, which both regulate the transition from the G2 to the M-phase and thus cell division [60]. Silver, which binds to proteins with thiol groups outside the cell can cause lipid peroxidation that increases the permeation of the cell membrane. Silver can initiate apoptosis via lipid peroxidation, increased intracellular ROS production, induction of caspase-3 activity or via p53 activation [61]. However, this cytotoxic action against cancer cells may be attributed to the nanosilver rather than to ionic silver [62,63].

pH

The alkalization of the surrounding environment during Mg degradation has the potential to neutralize the acidic TME and hence counteract some of the tumor growth initiating signaling pathways. An acidic extracellular pH (pH_e) was recently linked to increased tumor invasiveness and angiogenesis through the increased expression of platelet-derived endothelial growth factor [64], inducible NO synthase [65], and IL-8 [66] in diverse cancer cell lines through NF- κ B or activator protein-1 signaling. Acidic environments were also shown to stabilize the hypoxia inducible factor (HIF) under hypoxic conditions and stimulate VEGF expression via this pathway [67]. Therefore, alkalization may inhibit these pathways. Furthermore, Kato and colleagues [68] could show an increased MMP-9 expression in mouse melanoma cells cultured in acidic medium most likely via activated phospholipase D, MAPK and NF- κ B signaling. Moreover, an acidic pH_e disrupts cell-cell adherences through Src kinase activation and E-cadherin degradation and increases cancer cell motility [69]. The decreased pH_e does not only support cancer cell growth and spreading, moreover, it also protects cancer cells from external elimination. Ibrahim-Hashim and Estrella [70] concluded in their review that tumor acidosis can inhibit immunosurveillance. A reduced activity of lymphokine-activated killer cells, NK cells and cytotoxic T-cells as well as reduced TNF- α production by monocytes were shown in an acidic environment [71-74]. In contrast to this, increased H_2O_2 production and subsequent cancer cell cytotoxicity by neutrophils and monocytes in an alkaline pH_e were reported [75,76]. Besides, the efficacy of chemotherapeutic agents may also be increased with increased pH_e [77,78]. The acidic TME activates the p-glycoprotein that subsequently increases the drug efflux from cancer cells and contributes to chemoresistance [79,80].

Osmolality

The influence of extracellular osmolality, as observed during Mg degradation, on cancer cells is not yet very well investigated. The previous research focused only on the effect of hypotonic solutions on cancer cells *in vitro* and *in vivo*, showing cancer cell rupture after hypotonic shock [81]. This lack of in-depth knowledge highlights the necessity for a detailed analysis of individual influencing factors once more.

1.3 Cancer and conventional cancer therapy

Cancer represents one of the leading causes of death all over the world [82]. With 60 % of cancers diagnosed and half of the cancer deaths related to >65 years old patients, cancer can be termed as an age-related disease [83-85]. With the growing life expectancy owing to medical care and prosperity, the frequency of globally diagnosed cancers increases as well.

Cancer is defined as a malignancy characterized by cells that acquire an abnormal growth and invasive phenotype due to changes in the genome (mutations). Spontaneous (non-inherited) DNA mutations can occur as a result of incorrect DNA replication by DNA polymerases or due

to base pair alterations (oxidation, deamination, depurination) induced by external chemical and physical influences (e.g., tobacco and radiation). Such base pair alterations are very common due to the instability of the DNA molecule. However, these alterations can be repaired by special DNA repair mechanisms (homologous recombination repair and nonhomologous end joining) [86]. Likewise, DNA polymerases are equipped with a proof-reading function to detect DNA mutations caused by errors during DNA replication. In fact, alterations in the human genome are part of the natural selection in the evolutionary process and may be advantageous for the cells [87]. Moreover, only 1 % of the DNA is coding and due to codon recognition redundancy, thus many mutations remain silent and do not lead to changes in the proteome [86,88]. Yet, mutations can develop also in the coding regions of the DNA, leading to the malignant transformation of the cell, as the above-named detection and repair mechanisms are not infallibly (error rate of polymerase proof-reading= 1.3×10^{-10} mutations/base/division). Such transformed cells can exhibit a selection advantage to proliferate uninhibitedly and resist other preventive protection mechanisms (apoptosis and senescence), which shall eliminate malignant cells. This leads to an uncontrolled tumor mass growth that compromises normal cells and organ functions as shown in Figure 1.

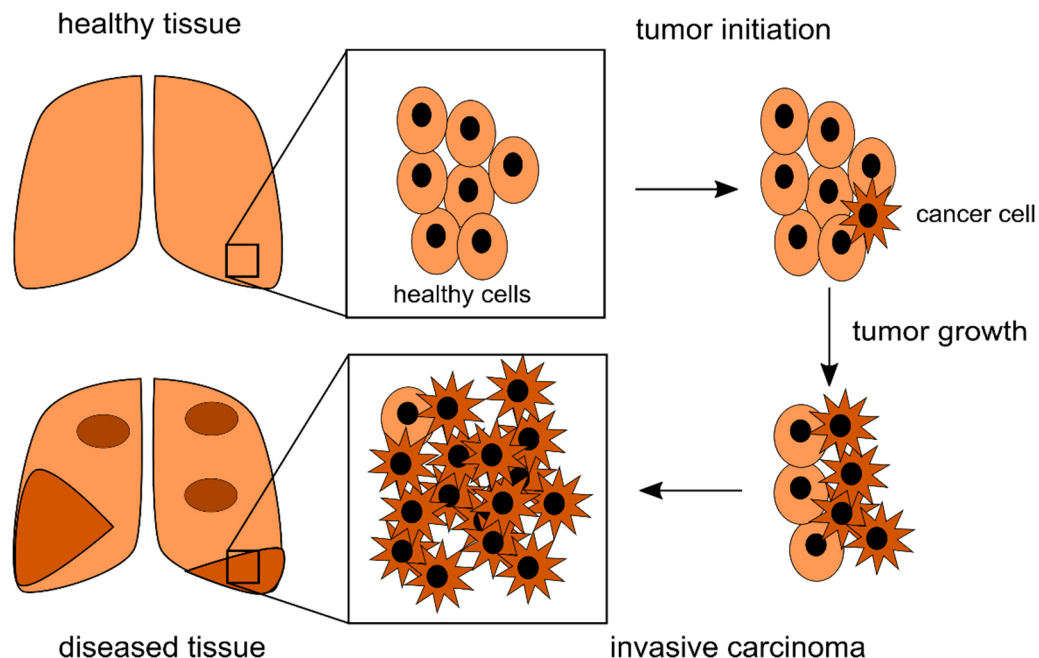


Figure 1. Cancer progression to organ failure.

If the cancer is especially aggressive, it can induce such an organ failure even faster or metastasize to other sites in the human body, which can lead to a multiorgan failure and consequently death. Lung cancers, for instance, compromise the lung function and lead to a reduced oxygen intake, while cancers of the digestive system can physically block the digestion and can lead to a life-threatening malnutrition.

Conventional cancer therapy includes surgery, chemotherapy, and radiation. While surgery alone does not fully reduce the tumor mass, especially at difficult surgical sites, a combination with radiation or chemotherapy goes along with severe side effects such as nausea, vomiting and hair loss. As cancer is treated systemically with these treatment strategies, consequently this also affects healthy cells. Besides, tumors are highly heterogenous in a location and time-dependent manner (spatial and temporal heterogeneity). Therefore, traditional therapies harbor the risk of ineffective cancer treatment and development of resistances [89]. Novel therapy approaches that aim to deliver therapeutic drugs directly to the tumor site or treat specific signaling pathways to reduce the aforementioned side effects and increase the

bioavailability and effective drug concentration, receive growing interest. These novel approaches include small molecule inhibitors and monoclonal antibodies. The personalized therapy receives growing interest due to the cancer heterogeneity. For this, tumor biopsies or blood are taken to identify the relevant mutations or other biomarkers and subsequently initiate an appropriate therapy. Further approaches focus on the support of the immune system to eliminate the cancer cells intrinsically, e.g. the chimeric antigen receptor (CAR) NK cell therapy, and CAR T cell therapy. Such therapies function through the extraction of NK cell and T cells, respectively. Then, those cells are genetically equipped with the CAR and introduced into the patient. Nevertheless, those targeted therapies can also have severe side effects (liver and skin problems) and are usually very expensive [90]. Another promising and cost-effective treatment approach may be Mg-based materials that were recently discussed as alternatives for cancer treatment since Mg and its degradation effects may interfere with the cancer biology on a molecular level [30-32].

1.4 Cancer biology

1.4.1 Cancer Hallmarks

Alternative treatment strategies, such as Mg-based materials, most probably interfere with cancer progression on a molecular level via combined mode of action. In order to elucidate these mechanisms, the strategy in this work was to categorize, select, and study cancer hallmarks. Those cancer hallmarks are characteristics of cancer cells that dictate the malignant progression.

Cancer hallmarks were first postulated by Hanahan and Weinberg [91,92] and include:

- Sustaining proliferative signaling
- Deregulating cellular energetics
- Inducing angiogenesis
- Avoiding immune destruction
- Activating invasion and metastasis
- Evading growth suppressors
- Enabling replicative immortality
- Resisting cell death
- Genome instability and mutation
- Tumor-promoting inflammation

Following, the most promising hallmarks that may be influenced by novel treatment approaches with Mg-based materials are discussed below.

Sustaining proliferative signaling

The ability to sustain proliferative signals, enabling uncontrolled cell divisions, is probably the best-known characteristic of cancer cells. While normal cells strictly regulated the amount of proliferative signals to maintain a homeostasis between cell death and cell proliferation, cancer cells circumvent this regulation by increasing growth factor secretion or exploiting adjacent cells to produce such growth factors. Further, the genomic instability of cancer cells can also lead to increased expression of growth factor receptors or their constitutive activation [92].

The latter is best described for the Philadelphia chromosome, which arises from a reciprocal translocation of the chromosomes 9 and 22 in chronic myeloid leukemia. This leads to a new fusion gene of the breakpoint cluster region (*BCR*) gene and the Abelson (*ABL*) tyrosine kinase gene (*BCR-ABL1*) that codes a constitutively active tyrosine kinase involved in uncontrolled cell divisions [93]. Additionally, mutations of proteins downstream of the growth receptors can lead to constitutive action (oncoprotein) or loss of function (tumor suppressors), as schematically shown in Figure 2.

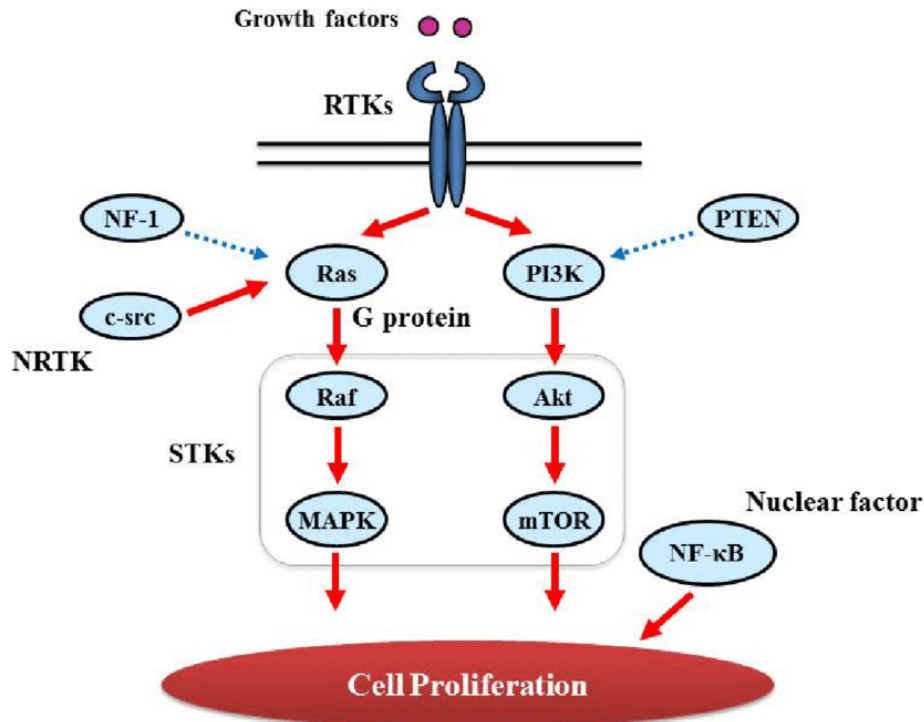


Figure 2. Main proliferation signaling pathways. Growth factor signaling is transduced via Ras or PI3K, which can be negatively regulated by NF-1 and PTEN, respectively. This negative feedback is often disrupted in cancer cells. Figure from Nakada *et al.* [94] (reproduced with permission from MDPI). Akt – protein kinase B, MAPK – mitogen activated protein kinase, mTOR - mechanistic Target of Rapamycin, NF-1 - neurofibromin 1, NF-κB - nuclear factor 'kappa-light-chain-enhancer' of activated B-cells, NRTK - non-receptor tyrosine kinase, PI3K - phosphoinositide 3-kinase, PTEN - phosphatase and tensin homolog, RTK – receptor tyrosine kinase, STK – serine/threonine kinase.

Frequent activation mutations can be observed in the serine/threonine-protein kinase B-raf that merges into the MAPK pathway in melanoma [95]. Another example is the phosphoinositide 3-kinase (PI3-kinase) and its downstream target Akt leading to the activation of the mechanistic Target of Rapamycin (mTOR), which is a kinase involved in cell growth, proliferation and survival [96] (Figure 2).

Loss-of-function mutations affect negative feedback loops, wherefore proliferation signal damping cannot be controlled any longer. Examples for this are neurofibromin 1 (NF-1) that regulates the action of the oncoprotein Ras [97] or the phosphatase and tensin homolog (PTEN), which controls PI3K signaling by degrading its product phosphatidylinositol (3,4,5) trisphosphate (PIP3) [92].

Deregulating cellular energetics

The cell proliferation increased and other cellular mechanisms in cancer cells demands a large amount of glucose and consequently energy equivalents, more precisely ATP. Compared to differentiated cells, cancer cells exhibit very inefficient mechanisms to produce ATP [98]. In

the presence of oxygen, differentiated (non-proliferating) cells produce ATP by glucose conversion to pyruvate during glycolysis which is followed by the tricarboxylic acid cycle and oxidative phosphorylation in the mitochondria. Oxygen supply is a crucial factor for the ATP production via oxidative phosphorylation (aerobic glycolysis). Under oxygen deficiency (hypoxia), the pyruvate is oxidized to lactate (anaerobic glycolysis). This yields a large difference in ATP production: While the aerobic glycolysis leads to 36 mol ATP, the anaerobic glycolysis only produces 2 mol ATP [98] as shown in Figure 3.

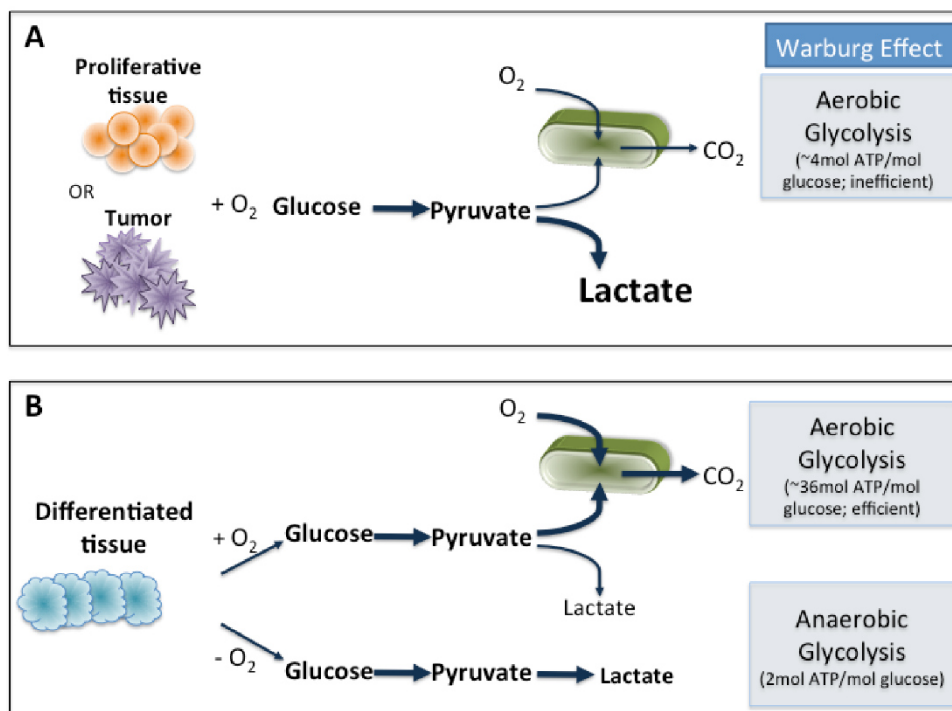


Figure 3. Different energy production of cancer cells and differentiated tissue. Figure is reproduced from [99] with permission from PLOS ONE.

Cancer cells majorly convert glucose into lactate regardless of the surrounding oxygen level (aerobic glycolysis), according to observations from Otto Warburg, a process named “Warburg Effect” [100]. Warburg hypothesized that this arises from impaired mitochondria functions, which has recently been disproved [101-103]. The advantage for cancer cells to conduct this inefficient energy conversion method (4 mol ATP) is still not very well known. One hypothesis is that the ATP generation through the Warburg effect is 10-100 times faster compared to the oxidative phosphorylation. Therefore, a comparable amount of ATP/time is produced [104,105]. Model simulations by Pfeiffer *et al.* showed that cells with a higher synthesis rate but lower ATP yield gain a selection advantage in resource competition over other cells [106].

Another approach that explains the preference of the Warburg effect over oxidative phosphorylation is the creation of a tumor microenvironment that favors carcinogenesis. During aerobic glycolysis and subsequent ATP hydrolysis, large amounts of lactate/ H^+ are produced [107] and excreted from the cell by various transporters to prevent apoptosis by intracellular acidosis [108,109]. Through the action of several (redundant and overexpressed compared to healthy cells) intracellular pH (pH_i) regulating transporters such as monocarboxylate transporters [110], carbonic anhydrases, V-ATPases [111] and sodium dependent proton exchangers [112], cancer cells are able to maintain an intracellular pH of 7.1-7.2 [113], while the extracellular space becomes acidic with pH_e values around 6.5 [114].

Aside from lactate/ H^+ , the generation of CO_2 in the pentose phosphate pathway is also accompanied with increased microenvironmental acidification [115]. However, this

Introduction

extracellular acidification is not only a protection mechanism, but also favors cancer progression as recently shown [116-120]. There, cancer cells in an acidic environment increased the expression of VEGF, IL-8, lactate dehydrogenase (LDH), cathepsin B and MMP-2 and 9 that are all linked to increased tumor growth, invasion, and metastasis *in vivo*.

Inducing angiogenesis

Cells need oxygen and nutrients to grow, proliferate and survive. Hence, they rely on the supply of oxygen and nutrients by blood vessels. In healthy tissue, the *de novo* formation of new blood vessels (vasculogenesis) by endothelial cells is majorly completed after embryogenesis. However, angiogenesis (sprouting of preexisting vessels) is transiently reactivated during e.g. wound healing, whereas cancer cells acquire the capability of a permanent ongoing angiogenesis [121]. This process is also termed “angiogenic switch”, when pro-angiogenic factors are upregulated and surpass downregulated anti-angiogenic signals [122]. Such a permanent powered angiogenic switch is essential for cancer cells to fulfill the nutritional demands during excessive cell proliferation at the tumor edges. Cancer cells residing at the core become isolated from the blood vessels and are thus exposed to oxygen depletion. Hypoxia is a common feature of cancer, and is also stimulated by oxidative stress and local pH changes [123] The oxygen level in tumor tissue ranges between 0.3-4.2 % [124], while the maximum oxygen level in healthy tissue (physoxia) is about 14.5 % in lung alveoli [125].

Hypoxia induces the activity of the transcription factor HIF-1, which is a main regulator of angiogenesis [126]. Under normal oxygenation, the HIF-1 α subunit is regulated by proteasome degradation by the binding of oxygen to the oxygen-dependent degradation domain [127], while HIF-1 α binds to HIF-1 β in the absence of oxygen. This dimer can then translocate into the nucleus and bind to the hypoxic responsive elements (HREs) of the target genes that express e.g., VEGF. Increased expression of both, HIF-1 and VEGF, has been associated with an aggressive and more malignant tumor phenotype [126]. Nevertheless, VEGF can also be activated HIF-independently by NF- κ B and K-ras as well as other oncoproteins [128]. The tumor vasculature is essential for the cancer progression. Thus, vascularization initiates early in highly invasive tumors.

The process of angiogenesis is comparable in normal and tumor tissue. First, the permeability of the blood vessels increases, which allows extravasation of proteins to degrade the basement membrane. Subsequently, interendothelial cell connections diminish to allow endothelial cell migration and proliferation. Finally, the endothelial cells form new connections to adjacent cells forming new lumen [128]. Yet, blood vessels induced by cancer cells significantly differ from that of a normal vasculature. The most obvious difference in appearance is that tumor vasculature is disorganized, while normal vasculature comprises a hierarchal structure of arteries, veins and capillaries [129]. Furthermore, tumor blood vessels are leakier compared to healthy blood vessels, due to loose interendothelial junctions, abnormal pericyte connections to the endothelium, and the absence of a tight endothelial cell monolayer [130]. They also vary in lumen diameter, which can cause uneven blood flow. This and the fact that a high interstitial fluid pressure in tumors can cause blood vessels to collapse is the reason for frequent hypoxic conditions, although the tumor is highly vascularized [130].

Avoiding immune destruction

The immune system is an endogenous defense against foreign material and transformed cells. In the mid-20th century, Thomas [131] and Burnet [132] postulated in their immunosurveillance hypothesis that the immune system regulates the development of malignant cell transformation. With increasing research, this hypothesis was adjusted since the immune system can also act as a natural selector for adapted cancer cells [133,134]. During this process, called immunoediting, the immune system eliminates most of the cancer cells due to

tumor antigen presentation (major histocompatibility complexes, MHC) [133,134]. Since the tumor is heterogeneous and genetically unstable, there are also cancer cells with an impaired antigen presentation (loss of antigenicity) or impaired recognition (loss of immunogenicity). In this phase (equilibrium phase) the immune control against immunogenic cancer cells and the proliferation of non-immunogenic cancer cells are in balance. In the subsequent escape phase, the selected cancer cells further mutate to get invisible for the immune cells. They can also develop an immunosuppressive microenvironment by e.g. macrophages or regulatory T-cells that can induce cell death in immune cells [135]. Further evasion mechanisms include the inhibition of apoptosis induction.

The downregulation or loss of MHC class I molecules is a frequent scenario to evade cytotoxic T-cells (CD8⁺) recognition. Yet, such cancer cells are then preferentially recognized and destroyed by NK cells, immune cells of the innate immunity [136]. NK cell activity is regulated by stimulatory and inhibitory signals that are transduced via activation and inhibition receptors on the NK cell surface. While activation receptors bind to cell surface protein ligands that represent danger and stress signals (MHC class I-related chain A, MICA; or Nectin), inhibitory receptors recognize endogenous ligands such as human leukocyte antigen (HLA) class I molecules HLA-A, HLA-B, and HLA-C [137]. NK cells are predominantly inactive if the inhibitory signal is higher than the stimulatory signal. If activation signaling, initiated by the NK cell receptors e.g. NKG2D or DNAX Accessory Molecule-1 (DNAM-1), surpasses inhibitory signals, the NK cells switches in an active mode to kill the target cell [138]. This killing process predominately initiates the release of granules containing perforin and granzyme B in tumors such as osteosarcoma [139]. Perforin is a cytolytic protein that binds to the membrane of the target cell and forms pores by oligomerization. Subsequently, the apoptosis initiator granzyme B can diffuse through the pore into the cell. Granzyme B is a serine protease that can cleave and activate caspase-3 that initiates a signal cascade ending in cell apoptosis [140]. Other killing mechanisms include the increased expression of death receptor ligands such as TNF-related apoptosis-inducing ligand (TRAIL), Fas, or antibody-dependent cellular cytotoxicity (ADCC). Moreover, NK cells are able to secrete cytokines such as interferon γ (IFN- γ) to activate an immune response of cells of the adaptive immune system and indirectly kill the targeted cells [137].

However, cancer cells also developed mechanisms to evade recognition or killing by NK cells, summarized in Figure 4. The two most obvious strategies are the increased expression of inhibitory receptor ligands and a low expression of activating receptor ligands, such as MICA, on the cancer cell [137]. For example, epigenetic regulation or the release of transforming growth factor β (TGF- β) can downregulate the expression of MICA. The exact opposite, the overexpression of activating ligands, can also protect the cancer cells from NK cell cytotoxicity. The persistent triggering of activating NK receptors leads to the downregulation of the NKG2D receptor. Furthermore, MMPs can cleave the activating ligands from the cancer cell surface, decreasing the ligand number, and soluble ligands can bind to and induce degradation of NKG2D [141]. Additionally, cancer cells can actively affect immune cell function to escape the elimination by the immune system. The TME and the expression of TGF- β by the cancer cells can inhibit the NK cell proliferation, NKG2D expression and the release of granzymes and perforin [142,143].

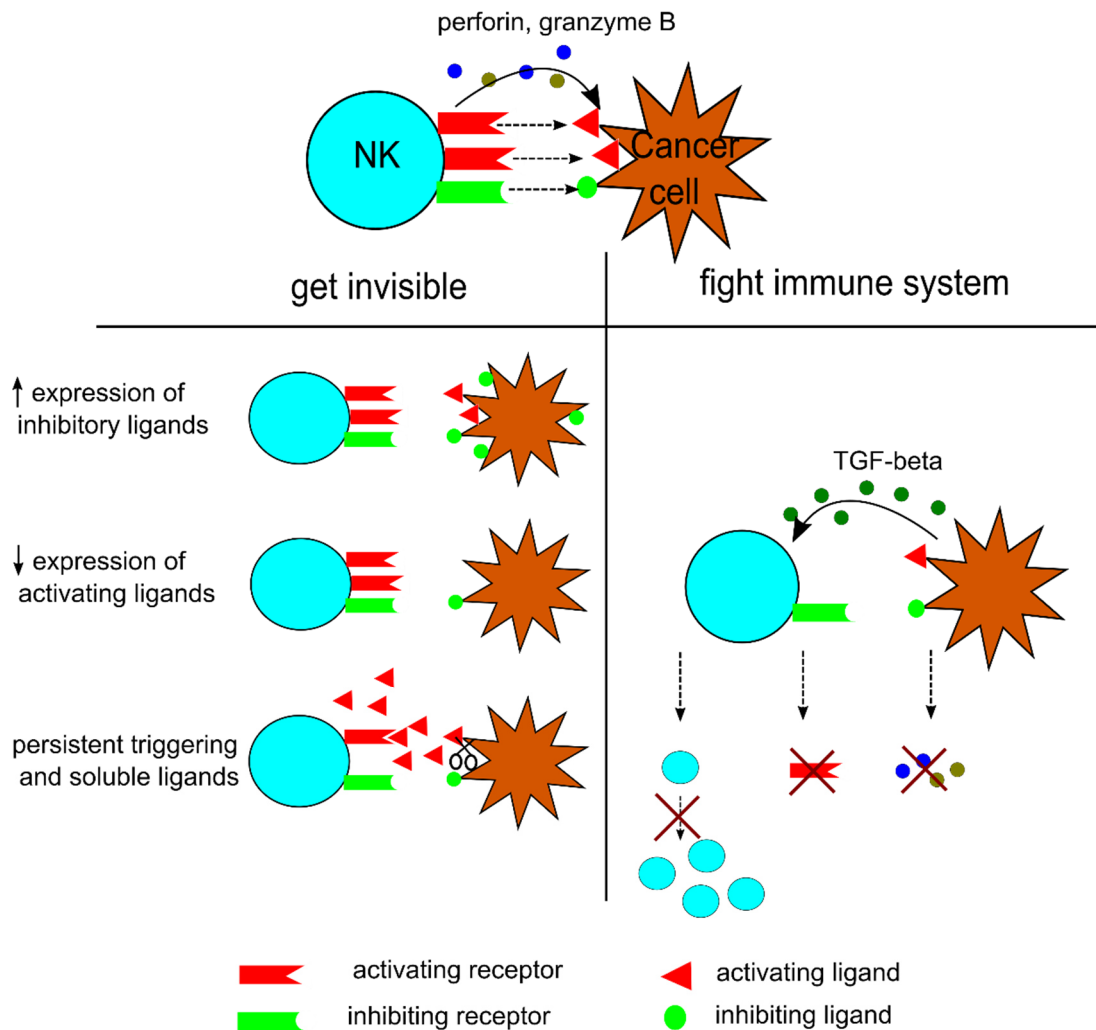


Figure 4. Mechanisms of cancer cell evasion from NK cells.

Activating invasion and metastases

The cancer capability of invasion and metastasis refers to the spreading of tumors to distant sites of the body and the formation of secondary tumors. This process can be divided into several steps: migration and invasion, intravasation, and extravasation. During the first step, cancer cells that are prone to metastasize lose the adhesion to adjacent cancer cells by a downregulation of E-cadherin, the major mediator of cell-cell adhesion [144]. Simultaneously, the expression of N-cadherin, vimentin and MMPs is increased, which changes the cancer cell from an epithelial to a mesenchymal phenotype. Therefore, this process is called epithelial-to-mesenchymal-transition (EMT). Changes in the cytoskeleton cause the formation of cytoplasmic extensions (filopodia) or cytoskeletal extensions (lammelipodia) that are important for the cell motility. Interactions with the stromal cells (fibroblasts, macrophages) of the tumor microenvironment (TME) further lead to increased MMP-2 and MMP-9 expression and therefore degradation of the surrounding extracellular matrix (ECM). This in turn enables migrating cells to reach the blood vessels and intravasate into the blood stream, which can occur a lot of times daily. However, circulating cancer cells are rapidly immobilized and eliminated [145]. The number of circulating tumor cells (CTCs) can be as low as 1-10 cells in 1 mL of the whole blood [146], which makes it difficult to efficiently detect them. The CTCs can extravasate at distant sites with low blood flow to allow sufficient adhesion of the cancer cells to the endothelium at the metastatic site. The adhesion of cancer cells and endothelial cells majorly depends on the matching of adhesion molecules and receptors on both cell populations

[147]. Extravasation is then initiated by endothelial cell permeability and that can be assisted by VEGF and TGF- β expression of exploited cells in circulation such as neutrophils and platelets [148]. Once extravasated into the metastatic site, the metastatic cancer cells are challenged with the adaption to the foreign metastatic environment. Interestingly, some cancer types tend to metastasize to the same selected organ sites, where different types only rarely metastasize at all. The most accepted explanation of this phenomenon is the “seed and soil” hypothesis postulated by Stephan Paget in 1889 [149]. This hypothesis relies on three principles:

- (I) Neoplasms at the primary and secondary site involve cancer cells and infiltrated host cells in the TME. The tumor is heterogeneous and consist of different subpopulations that allows the metastatic cascade for some of the cancer cells.
- (II) The cells that successfully metastasize and grow into secondary tumors at the metastatic site underwent several selection steps from invasion to extravasation, which partly involves stochastic models.
- (III) The outcome of this metastatic process is based on a complex interaction of the cancer cells (seed) and the organ-specific host environment (soil) that should match [145].

Recent studies suggested that no additional genetic mutations are needed for cancer cells to become metastatic [92]. This was also supported by the work of Vogelstein *et al.* [150] who could not distinguish metastatic and non-metastatic cancer cells and concluded that there are no metastatic genes. This led to the assumption and confirmation that epigenetic modifications are the driving force of metastases [151,152].

1.4.2 Tumor microenvironment/cancer associated cells

The tumor itself should not be seen as a mass of proliferating cells, but as a complex network of different cell types that promote carcinogenesis and distinctive capabilities of cancer, as proposed by Hanahan and Weinberg [91]. This complex network is described as the TME and includes not only cancer cells, but also fibroblasts, immune and endothelial cells [153] as shown in Figure 5.

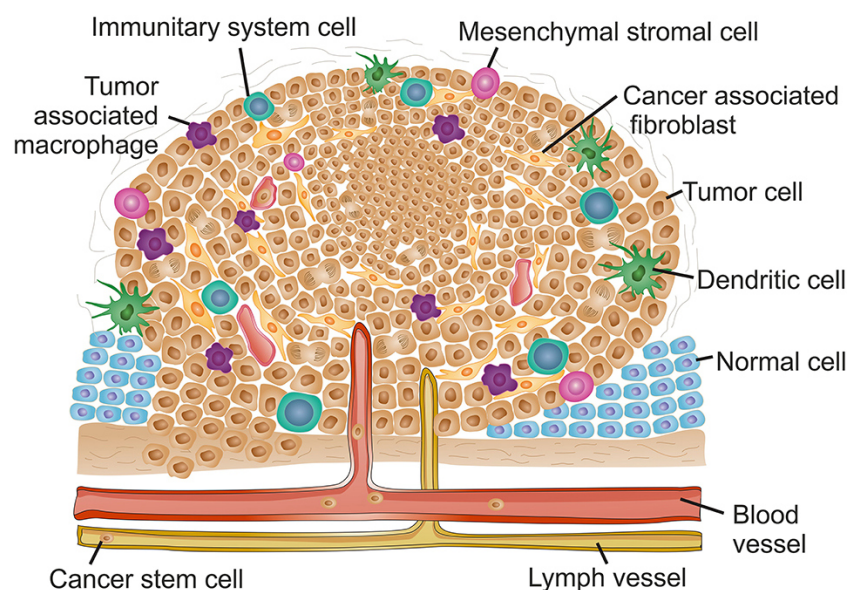


Figure 5. “The complex context of tumor microenvironment”, by Roma-Rodrigues *et al.* [154], licensed under CC BY 4.0. More on <https://creativecommons.org/licenses/by/4.0/>. The original image was not modified.

Introduction

Fibroblasts are the main cell type in the connective tissue. They are majorly responsible for the structure formation by ECM components secretion [155] and degradation through MMPs. In the TME, fibroblasts are irreversibly activated to cancer-associated fibroblasts (CAF) and acquire a phenotype that resembles normal fibroblasts in wound healing (expression of alpha smooth muscle actin, α -SMA) [156]. Once activated to CAF, they assist cancer cells by secreting growths and angiogenesis factors as well as MMP to promote cancer proliferation and invasion [156]. Furthermore, cancer cells recruit immune cells like monocytes that differentiate to tumor-associated macrophages (TAM) in the TME. They promote carcinogenesis by secretion of numerous cytokines and chemokines like VEGF, MMP-2 and IL-8 to stimulate angiogenesis and metastasis [156]. Recent findings suggested a direct correlation between TAM density and poor clinical prognosis [157,158]. Endothelial cells are the main components responsible for oxygen and nutrient supply of the cancer cells [159]. Through their function to form new blood vessels, endothelial cells also participate in immune cell recruiting, cancer growth and metastasis to distinct body sites [153].

Based on the essential cell-cell interaction in the TME, stromal cells are important to consider for cancer cell models for the investigation of novel cancer therapy approaches, such as Mg-based materials. Therefore, a coculture of cancer cells and fibroblasts can enhance the relevance of such investigations.

2 Motivation and objectives

Mg-based materials are potential candidates for osteosarcoma therapy due to their degradability and concomitant bone healing effects. Owing to their degradation-dependent surface-near effects, Mg-based materials have already been investigated for their anticancer activity. However, additional research is needed to isolate and understand the signaling pathways behind the anticancer activity. Previous studies focused only on the Mg material influence on cancer cells in monoculture, however it is known that monocultures are not suitable to reflect *in vivo* situations. Cancer models comprising one or two TME specific cell types aside from the cancer cells are suggested to increase the relevance of the results. Therefore, the present thesis investigates the influence of Mg degradation on an osteosarcoma coculture model consisting of fluorescently labelled osteosarcoma cells and fibroblasts. A promising cancer therapy approach should kill the cancer cells specifically with minimal harm to the adjacent healthy tissue, or at least reduce the tumor growth. Therefore, not only the cytotoxicity of slow-degrading Mg-based materials was tested, but also their influence on selected cancer hallmarks that contribute to the tumor outgrowth. Additionally, the interaction of cancer cells with their environment plays a crucial role in cancer progression. For the design of Mg-based materials for future osteosarcoma therapy, understanding the influence of all individual surface-near effects is essential to tailor the Mg degradation specific to the application.

The following objectives were pursued:

- (I) Development and assessment of the suitability of the fluorescently labeled osteosarcoma-fibroblast coculture model to analyze the cytotoxicity of slow degrading Mg-based materials
- (II) Investigation of the influence of slow degrading Mg-based materials on the selected cancer hallmarks: sustaining proliferative signaling, inducing angiogenesis, avoiding immune destruction, and activating invasion and metastasis.
- (III) Determination of the most probable responsible degradation dependent surface-near effect for the observed influences.
- (IV) Investigation of degradation rate tailored Mg-6Ag for anticancer activity.

3 Materials and methods

3.1 Production of Mg-based materials

This thesis focuses on the influence of Mg and Mg-6Ag materials on osteosarcoma cells. Therefore, slow degrading Mg and Mg-6Ag discs were used to study the influence on different cancer hallmarks. To study the influence of the Mg degradation rate and the accompanied surface-near effects on cancer toxicity, fast degrading (T6 treated) Mg-6Ag samples were used. Table 1 resumes a list of experiments that were conducted with slow or fast degrading materials. To elucidate the influence of the individual Mg degradation-dependent surface-near effect on tumorigenesis, single parameter solutions were prepared (see chapter 3.5.2) and used in selected analyses as indicated in Table 1.

Table 1. Overview of analyses and corresponding used materials

	Used cell types	Slow degrading material (direct)	Fast degrading material (direct)	Single parameter solutions (indirect)
In vitro degradation	Saos-eGFP, RF Fibroblasts	+	+	-
Cell viability	Saos-eGFP, RF Fibroblasts	+	+	+
Cytotoxicity	Saos-eGFP, RF Fibroblasts	+	-	-
<u>Cell proliferation status</u> - Ki-67 expression - Molecular mechanisms	Saos-eGFP, RF Fibroblasts	+	-	+
		+	-	-
<u>Metastatic potential</u> - 2D migration - 3D invasion - Metastatic cytokines	Saos-eGFP, RF Fibroblasts	† (here indirect) † (here indirect) +	- - -	† - -
<u>Influence on NK cell activity</u> - NK cell related cytotoxicity - NK cell related granule proteins	Saos-eGFP, RF Fibroblasts with NK-92	+	-	+
		+	-	-
Cancer induced angiogenesis	HUVEC*	† (indirect: conditioned medium of material and Saos-eGFP/RF Fibroblasts)	-	-

*human umbilical vein endothelial cells

Slow degrading materials

Pure Mg (99.95 %) discs were fabricated at Helmholtz-Zentrum hereon (Helmholtz-Zentrum hereon GmbH, Geesthacht, Germany) by permanent mold gravity casting (K10/S; Nabertherm

GmbH, Lilienthal, Germany). Mg-6Ag (Mg with 6 weight % Ag) discs were prepared by direct chill casting method. The resulting cast ingots were T4 (solution treatment) heat treated and extruded into rods (10 mm diameter). The rods were machined and cut into discs with a diameter of 9 mm and 1.5 mm thickness (Henschel KG, Munich, Germany). The chemical composition of the here used Mg and Mg-6Ag discs (spark spectrometry) is shown in Table 2.

Table 2. Chemical analyses of the used Mg and Mg-6Ag materials. Al - aluminum, Ag - silver, Cu - copper, Fe - iron, Mg - magnesium, Ni - nickel

	Weight %					
	Mg	Fe	Cu	Ni	Al	Ag
Mg	99.94	0.0048-0.0049	0.0002-0.0003	<0.0002	0.013-0.016	<0.00005
Mg-6Ag	≈94	0.0019-0.0021	0.0013-0.0014	0.009-0.0010	<0.0100	5.94-6.34

Fast degrading material

The preparation of fast degrading materials from slow degrading materials was not part of this work and was performed by Khausik Narasimhan (Helmholtz-Russian Science Foundation Joint Research Groups 0025). Slow degrading Mg-6Ag discs were subsequently T6 (aging treatment) treated in a resistance furnace (VulcanTM A-550, Dentsply Ceramco, USA), under argon atmosphere and quenched in water.

3.2 Cell culture and proliferation

Table 3. Used cell lines and specifications.

Cell line	Referred to as	Origin	Provider
Saos-2, genetically modified to constitutively express eGFP	Saos-eGFP	Osteogenic sarcoma	Created and kindly provided by Prof. Dr. Tognon (University of Ferrara, Italy) [160]
Red fluorescent primary human dermal fibroblasts expressing FP602	RF Fibroblasts	Human dermal fibroblasts	Innoprot, Derio, Spain
NK-92	NK or NK cell	Natural killer lymphoma	German Collection of Microorganisms and Cell Cultures GmbH
Human umbilical vein endothelial cells	HUVEC	Endothelial cells of umbilical cord	Agaplesion Bethesda Krankenhaus Bergedorf (Isolation approved by Ethik Kommission der Ärztekammer Hamburg (PV4058) [161])

Materials and methods

Saos-eGFP and RF Fibroblasts were maintained in T75 standard cell culture flasks (Greiner Bio-One International GmbH, Kremsmünster, Austria) in Dulbecco's Modified Eagle Medium (DMEM GlutaMAX-I; Life Technologies, Darmstadt, Germany) supplemented with 10 % fetal bovine serum (FBS, Merck KGaA, Darmstadt, Germany). HUVEC were cultured in endothelial cell growth medium 2 (ECGM) with a respective supplement (Promocell, Heidelberg, Germany) in T25 standard culture flasks (Greiner Bio-One International GmbH, Kremsmünster, Austria). The suspension cell line NK-92 was expanded in T75 suspension cell culture flasks (Greiner Bio-One International GmbH, Kremsmünster, Austria) in NK-medium, consisting of Minimum Essential Medium α (α -MEM, Life Technologies, Darmstadt, Germany) supplemented with 12.5 % FBS, 12.5 % horse serum (HS, Biowest, Nuaille, France) and 5 ng/mL IL-2 (Alfa Aesar, Haverhill, MA, USA). All cells were maintained in an incubator (Heraeus BB 6220, Life Technologies GmbH, Darmstadt, Germany) to ensure constant cell culture conditions of 37 °C, 5 %CO₂ and a humidified atmosphere, 95 % relative humidity). At 80-90 % confluence, all adherent cell lines were passaged by washing once with 0.01 M phosphate buffer saline (PBS, Life Technologies GmbH, Darmstadt, Germany) and detaching the cells using 0.05 % trypsin - ethylenediaminetetraacetic acid (EDTA; Life Technologies GmbH, Darmstadt, Germany) in the incubator for 5 minutes. The dissociation reaction was stopped by the addition of cell culture medium. The cells were then diluted in fresh medium into a new cell culture flask. NK-92 were passaged every 2-3 days. For NK passaging, the cells were counted (CASY Counter, Roche Diagnostics GmbH, Mannheim, Germany), centrifuged at 200g (Rotina 420, Andreas Hettich GmbH & Co. KG, Tuttlingen, Germany) and resuspended in fresh medium in a new cell culture flask at a concentration of 2×10^5 cells/mL.

Proliferation of adherent cells was determined by counting the number of viable cells. Therefore, 5×10^4 cells were seeded into 6-well plates. The cells of two wells were then dissociated and counted (CASY Counter, Roche Diagnostics GmbH, Mannheim, Germany) after 24, 48, 72, 96, 144 and 168 h.

3.3 In vitro tests

In vitro immersion tests are used to determine the degradation rate of a material. The immersion test was conducted under semi-static conditions and the degradation rates were determined by weight loss after removal of degradation products.

3.3.1 Degradation rate of Mg-based materials

Material preparation

Prior to immersion, Mg and Mg-6Ag were wet-ground with SiC 2500 grid paper (Starcke GmbH & Co.KG, Melle, Germany) from both sides using a grinding machine (Saphir 360, ATM GmbH, Mammelzen, Germany). Ground discs were then cleaned in n-hexane, acetone and ethanol for 20 min each in an ultrasonic bath (Branson 1210, Branson Ultrasonics, Danbury, USA). The initial weight of the samples was measured with a micro-scale (Scaltec, Scaltec Instruments GmbH, Göttingen, Germany). Afterwards, the samples were sterilized in 70 % ethanol for an additional 20 min, dried under sterile conditions and transferred into a 24-well plate. Afore, this plate was coated with 1 % agarose to minimize unwanted cell attachment to the tissue culture plastic. The disks were incubated in 2 mL DMEM supplemented with 10 % FBS under cell culture conditions for one, three or seven days.

After immersion, the Mg-based material discs were rinsed in ultrapure H₂O grade I and 100 % ethanol. The degradation layer was removed through chromic acid treatment (180 g/L in

ultrapure water, VWR International, Darmstadt, Germany) for 10 min per side. To remove residual chromic acid, the samples were again rinsed in ultrapure water and ethanol. Then, the mass of the dried samples was determined to calculate the degradation rate using Eq. 4 [162]:

$$DR = \frac{K \times W}{A \times T \times D} \quad (\text{Eq. 4})$$

K - constant to adapt the degradation rate in mm/a ($K = 8.76 \times 10^4$),

W - mass loss in g,

A – sample area in cm^2 ,

T - immersion time in h,

D - density of Mg or Mg-6Ag in g/cm^3 (determined by initial mass and volume of the samples).

Analysis of pH und osmolality in the supernatant

Supernatants were taken to measure the pH and osmolality one, three and seven days after the cell seeding. The remaining old medium was aspirated, and fresh medium was added. An ion-sensitive field-effect transistor (ISFET) pH sensor (Sentron SI600, Sentron Europe BV, Roden, The Netherlands) was used to measure supernatant pH. To measure the osmolality of the supernatants, 50 μL were transferred to an osmometer measuring vial (Gonotec GmbH, Berlin, Germany) and analyzed with a freezing point osmometer 'Osmomat Auto' (Gonotec GmbH, Berlin, Germany). Delta pH (ΔpH) and osmolality values ($\Delta\text{osmolality}$) were calculated according to Eq. 5 and Eq. 6 for fast degrading Mg-6Ag (chapter 4.7), to eliminate deviations between different independent experiments:

$$\Delta\text{pH} = \text{pH}_{\text{material}} - \text{pH}_{\text{medium}} \quad \text{Eq. 5}$$

$$\Delta\text{osmolality} = \text{osmolality}_{\text{material}} - \text{osmolality}_{\text{medium}} \quad \text{Eq. 6}$$

$\text{pH}_{\text{material}}$ and $\text{osmolality}_{\text{material}}$ refer to the pH and osmolality with Mg-6Ag. $\text{pH}_{\text{medium}}$ and $\text{osmolality}_{\text{medium}}$ represent the pH and osmolality of medium without material.

Quantification of Mg and Ag in the supernatant

Quantification of Mg and Ag were performed by atomic absorption spectroscopy (AAS) and inductively coupled plasma mass spectrometry (ICP-MS). The AAS set-up and principle is shown in Figure 6. The sample is transformed into an atomic form in the flame. An element specific wavelength passes through the flame and is absorbed by the atoms of interest. The differences in light absorbance can then be detected eventually [163,164].

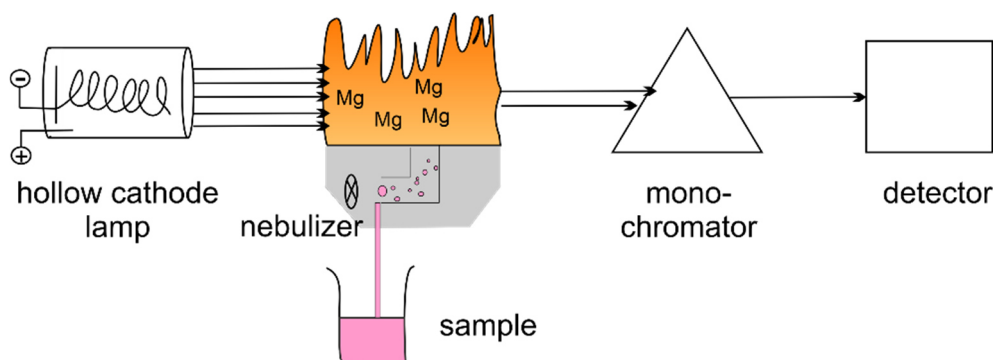


Figure 6. Basic set-up of AAS to measure Mg content in the supernatant.

Along with the supernatants for pH and osmolality measurements, supernatants for Mg and Ag content quantification were additionally saved. To preserve the supernatants and minimize precipitations, the samples were acidified with 1 % (w/v) nitric acid (HNO_3 suprapur, Merck KGaA, Darmstadt, Germany) diluted in ultrapure H_2O and subsequently stored at 4 °C. Mg

Materials and methods

supernatant concentrations during the degradation of pure Mg were measured by AAS, since the concomitant detection of Mg and Ag was biased due to emission spectrum interferences. The acidified samples were further diluted (1:250) in 1 % HNO₃. A flame AAS (Agilent 240 AA, Agilent Technologies, Waldbronn, Germany) was used to detect the absorption at 285.2 nm, which refers to the emission spectrum of Mg. To quantify the resulting Mg supernatant concentrations, a calibration curve (0.05-1.00 mg/L Mg) was measured in advance. The standards were prepared with a reference solution (Carl Roth GmbH+Co. KG, Karlsruhe, Germany). The limit of detection (LOD) and limit of quantification (LOQ) were calculated from the standard curves and were at around 20 µg/mL (LOD) and 56 µg/mL (LOQ). Further AAS measurement parameters are listed in

Table 4.

Table 4. Flame AAS parameters

Parameter	Dimension
Wavelength	285.2 nm
Slit Width	0.5 nm
Gain	31 %
Lamp Current	10.0 mA
Background Correction	BC On
Measurement Time	3.0 s
Pre-Read Delay	3.0 s
Flame Type	Air/Acetylene
Air Flow	13.50 L/min
Acetylene Flow	2.54 L/min
Replicates Standard	3
Replicates Samples	3

The ICP-MS set-up and principle is depicted in Figure 7. The sample is dispersed into an aerosol and transported to the argon plasma torch, where the sample is ionized. Afterwards, the ions are separated in the mass spectrometer according to their mass/charge ratio [165].

The simultaneous release of Mg and Ag during Mg-6Ag degradation was detected via ICP-MS. Therefore, acidified supernatants were further diluted (1:1000-1:2000) with 1% (w/v) HNO₃ to 30 mL in digiTUBEs (S-prep GmbH, Überlingen, Germany). At first, these tubes were flushed with 1% (w/v) HNO₃ in ultrapure water to minimize the contaminations that would dramatically influence the sensitive measurement. Finally, an ICP-mass spectrometer (Agilent 7900 ICP-MS, Agilent Technologies, Waldbronn, Germany) equipped with an ESI PFA microflow nebulizer (Elemental Scientific, Omaha, NE, USA) was used to detect and quantify the Mg and Ag supernatant concentrations. The limits for Mg quantification were at 0.92 µg/L (LOD) and 2.79 µg/L (LOQ) and for Ag measurements at 0.95 µg/L (LOD) and 2.89 µg/L (LOQ). This measurement was performed in the coastal research of the Helmholtz-Zentrum hereon (Helmholtz-Zentrum hereon GmbH, Geesthacht, Germany).

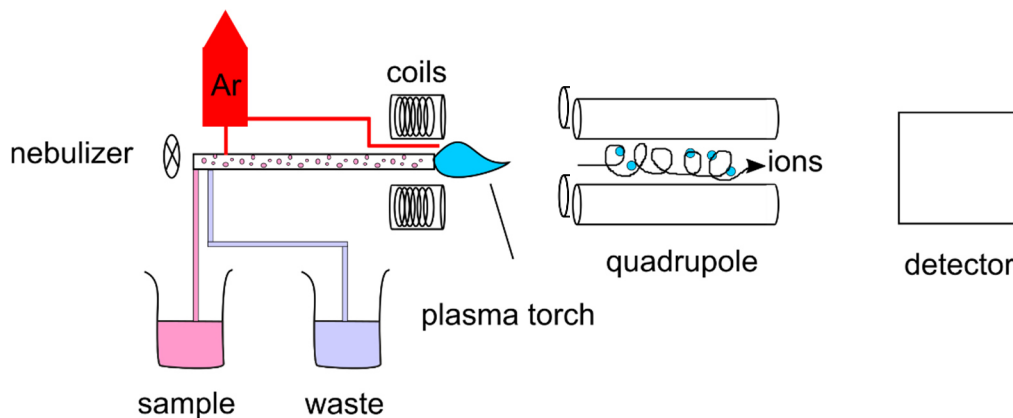


Figure 7. Basic set-up of ICP-MS to measure Mg and Ag content simultaneously in the supernatant.

3.3.2 Biological tests

For biological tests, the Mg-based disks were ground and cleaned as described in chapter 3.3.1. After the sterilization step, the disks were preincubated in 2 mL cell culture medium for 24 h prior to cell seeding.

The Saos-eGFP and RF Fibroblasts were dissociated from the flask with 0.05 % trypsin-EDTA (Life Technologies GmbH, Darmstadt, Germany) and counted using a CASY Counter (Roche Diagnostics GmbH, Mannheim, Germany). Both cell types were mixed to set a coculture of osteosarcoma cells and healthy fibroblasts in a ratio of 1:1. Subsequently, the indicated total cell numbers for each method were applied to each disc or glass slide surface in a volume of 40 μ L and allowed to adhere in the incubator for 20 min. Finally, 2 mL of DMEM supplemented with 10 % FBS were added to each well and the discs were incubated under normoxia (20 %) or hypoxia (3 %) in the incubator. To analyze the cell numbers on opaque material (Mg, Mg-6Ag, Ti-6Al-4V), images of the constitutively fluorescent Saos-eGFP and RF Fibroblasts were taken with an epi-fluorescence microscope (Nikon Eclipse Ni, Nikon GmbH, Düsseldorf, Germany), while pictures of the cells on glass slides were taken with an inverse fluorescence microscope (Eclipse Ti-S; Nikon GmbH, Düsseldorf, Germany). A suitable filter set for fluorescein isothiocyanate (FITC) and TexasRed were used to visualize green fluorescent Saos-eGFP and red fluorescent RF Fibroblasts, respectively. Cell numbers were analyzed with ImageJ (Rasband, W.S., ImageJ, U.S. National Institutes of Health, Bethesda, MD, USA, <https://imagej.nih.gov/ij/>, 1997–2018) through optimized thresholding and analysis of particles (size: 100 μ m²-infinity; circularity: 0-0.8). The monocultures of Saos-eGFP (MCS) and RF Fibroblasts (MCF) served as cell controls for the coculture. Cells on glass slides (glass control) and Ti-6Al-4V (Ti control) served as controls for Mg and Mg-6Ag on non-degradable materials.

After each use, Ti-6Al-4V samples were cleaned in 2% Hellmanex II solution (Hellma Materials GmbH, Jena, Germany), chloroform, and ethanol (both from Merck KGaA, Darmstadt, Germany), for 20 min each in an ultrasonic bath (Branson 1210, Branson Ultrasonics, Danbury, USA). Sterilization was then conducted by autoclaving at 121 °C for 1 h and subsequently in the ultrasonic bath with 70 % ethanol for 20 min before use.

3.4 Cytotoxicity tests of Mg-based materials

Cytotoxicity of the Mg-based materials was assessed via LDH release into the supernatant, live and dead cell discrimination by flow cytometry, as well as detection of oxidative stress and apoptosis.

Lactate dehydrogenase content in the supernatant of exposed cells

Measuring the LDH release into the supernatant by damaged cells is a fast and precise method to quantify cytotoxicity of a treatment or culture condition. This method is based on the color change reaction from tetrazolium salt to formazan conducted by a redox reaction involving the enzymes LDH and diaphorase (Figure 8).

The concentration of released LDH from the coculture into the supernatant was measured with the Cytotoxicity Detection KitPLUS LDH kit (Roche, Basel, Switzerland). Supernatants from osteosarcoma-fibroblast coculture on Mg-based materials, Ti-6Al-4V and glass were taken one, three and seven days after cell seeding. Those supernatants were transferred to a 96-well plate in triplicates, 50 μ L each, and incubated with 50 μ L reaction mix that consists of a dye solution and diaphorase for 30 min at room temperature (RT) in the dark. Subsequently, the absorbance was measured at a wavelength of 490 nm with an absorbance microplate reader (Sunrise™ Tecan microplate reader; Tecan, Männedorf, Switzerland). The coculture seeded on glass served as the glass control, on Ti-6Al-4V as the Ti control and lysed cells (lysis solution provided in the kit) as the lysis control.

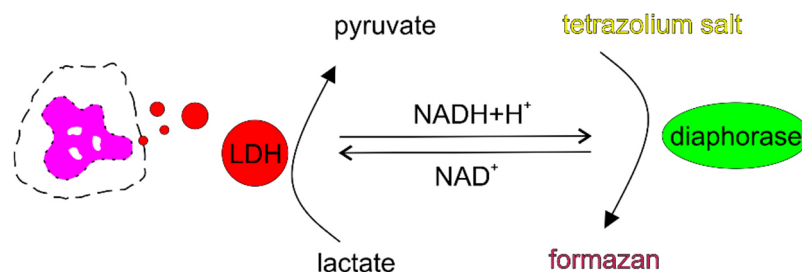


Figure 8. Principle of the color reaction to measure LDH content. Leaking LDH from dead cells converts lactate to pyruvate. This reduces NAD^+ to $\text{NADH}+\text{H}^+$, which is then involved in the reduction of tetrazolium salt into colored formazan.

Determination of live and dead cells

The Vivafix dyes from Biorad (Hercules, CA, USA) represent a reliable method to determine live and dead cells out of a cell mix with an option to further characterize these two subgroups with the flow cytometer. This method relies on the principle that the Vivafix dyes can covalently bind to primary amines. On living cells, they can only bind the amines present on the cell membrane, while they can permeate dead/damaged cells and additionally bind to intracellular free primary amines, giving a stronger signal (Figure 9).

Cells of the coculture were detached from the different materials with 0.05 % trypsin-EDTA seven days after cell seeding. After stopping the dissociation reaction with cell culture medium, the resulting cell suspension was transferred into flow cytometry tubes (Becton Dickinson, Franklin Lakes, NJ, USA). Three washing steps, including centrifugation at 200g for 5 min, supernatant aspiration, and resuspension in PBS, were applied. After the last washing step, the cell pellet was resuspended in 500 μ L PBS and 1 μ L VivaFix 547/573 (Biorad, Hercules, CA, USA) and was subsequently incubated in the dark at room temperature for 30 min. Another two washing steps were applied, and the resulting cell pellet was resuspended once more in 500 μ L PBS. The cell suspension was then analyzed for Saos-eGFP (FL1), VivaFix 547/573 (FL2) and RF Fibroblasts (FL3) using a cell sorter employing an excitation wavelength of 488 and 561 nm (S3e, Biorad, Hercules, CA, USA), respectively.

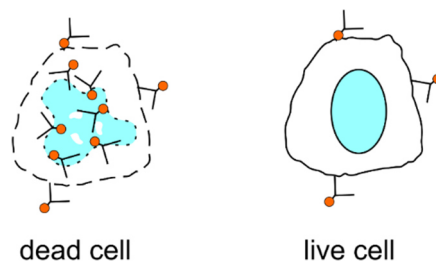


Figure 9. Illustration of live and dead cell discrimination by flow cytometry. Vivafix dyes can only permeate leaky cell membranes, which results in a higher fluorescence signal for dead cells compared to live cells.

Oxidative stress and apoptosis induction

Oxidative stress and apoptosis upon cell incubation with Mg-based materials were visualized simultaneously. Reactive oxygen species (ROS) were detected with a cell-permeant but non-fluorescent dye (CellROX Deep Red). With intracellular oxidation by ROS, this non-fluorescent dye gets highly fluorescent and stays in the cells. To detect apoptotic cells, a non-fluorescent DNA binding dye (NucView 405 Caspase-3 substrate), that is linked to the caspase-3/7 recognition sequence, is introduced to the cells. Activated caspase-3 will cleave the caspase-3/7 recognition sequence and release the dye into the nucleus where it binds to the DNA and emits fluorescent signals. Apoptosis was induced in the effect control by incubating the cells under atmospheric conditions for 24 h.

Oxidative stress and apoptosis induction of Mg-based materials were analyzed seven days after cell seeding. Therefore, a staining solution consisting of 5 μM CellROX Deep Red reagent (Thermo Fisher Scientific, Waltham, MA, USA) and 2 μM NucView 405 Caspase-3 substrate (Biotium Inc., Hayward, CA, USA) in cell culture medium was prepared. Old medium was aspirated, 50 μL of the staining solution was added directly on each material surface and incubated at 37 $^{\circ}\text{C}$ for 30 min in the incubator. Subsequently, images of three randomly chosen positions of each sample were taken with a confocal laser scanning microscope (cLSM, DM 6000 CS, Leica, Wetzlar, Germany) using the following wavelengths (Table 5). ROS was additionally triggered with 100 μM menadione treatment in the effect control at 37 $^{\circ}\text{C}$ for 1 h.

Table 5. Excitation and emission wavelengths for ROS and caspase-3 visualization in the coculture

Target	Excitation laser wavelength	Emission wavelength
Caspase-3	405 nm	450/50 nm
Saos-eGFP	488 nm	507 nm
RF Fibroblasts	552 nm	602 nm
ROS	633 nm	665 nm

Fluorescence intensity of ROS, and thus oxidative stress production in the cells, was quantified by calculating the corrected total cell fluorescence (CTCF) using ImageJ (Rasband, W.S., ImageJ, U.S. National Institutes of Health, Bethesda, MD, USA, <https://imagej.nih.gov/ij/>, 1997–2018). Calculating the CTCF of the images will eliminate false results through different background noises in the images. For each picture, 2-3 cancer cells and healthy fibroblasts were outlined in the single channel images and these outlines were opened in the ROS channel image. Furthermore, three cell-free positions were outlined for background measurements.

Subsequently, the area, integrated density (IntDen), and mean gray value (mean GV) were analyzed for the cell outlines and the background. CTCF was then calculated as follows (Eq. 7) [166]:

$$CTCF = IntDen - cell\ area \times average\ of\ mean\ GV\ background \quad (Eq. 7)$$

Since dead cells could not be outlined, apoptosis was analyzed with the corrected total field fluorescence (CTFF). This also eliminates errors that can occur due to different fluorescent signals with different material reflectance. Here, the area, IntDen, and GV of the whole field of view and three obvious background positions were evaluated. The CTFF equation derived from that of the CTCF (Eq. 8):

$$CTFF = IntDen\ of\ field - field\ area \times average\ of\ mean\ GV\ background \quad (Eq. 8)$$

3.5 Coculture proliferation with Mg-based materials

3.5.1 Proliferation status of the coculture

Cell proliferation was visualized using the proliferation marker Ki-67. To elucidate how the proliferation status of the cells can differ on degrading or non-degrading material, IL-8 and the phosphorylated SMAD2/SMAD 3 complex were quantified. Both are associated with increased proliferation via MAPK (IL-8) or TGF- β (SMAD2/SMAD3) signaling.

Proliferation marker Ki-67

Due to the comparatively small amount of cells seeded on the Mg-based materials, the intracellular proliferation marker Ki-67 was detected by immunofluorescence and quantified with ImageJ. Ki-67 is differently expressed throughout the entire cell cycle (Figure 10). It is a suitable marker for proliferating cells, an absence or low Ki-67 expression can point to a G0/G1 arrest.

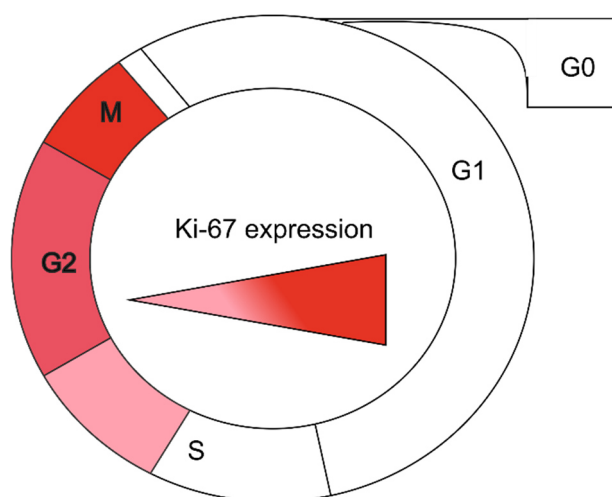


Figure 10. Schematic illustration of the different Ki-67 expression during the cell cycle.

The cells were incubated as coculture or monocultures under normoxia or hypoxia as described before. To investigate the influence of protein kinase RNA-like endoplasmic reticulum kinase (PERK) inhibition on cell proliferation, the cells were incubated with 5 μ M of the selective PERK inhibitor GSK2606414 (Hölzel Diagnostika, Cologne, Germany) in cell culture medium for 72 h prior to staining. After immersion, the cells were fixed and permeabilized in 2 % paraformaldehyde (Alfa Aesar, Haverhill, MA, USA) and 0.5 % Triton X-

100 (Thermo Fisher Scientific, Waltham, MA, USA), respectively, both in PBS supplemented with 10 % FBS at room temperature for 20 min. Three washing steps in PBS with 10 % FBS followed, each for 5 min. Fast proliferating cells were visualized by detecting the proliferation marker Ki-67 with anti-Ki-67-PerCP-Vio700, Clone REA183 (Miltenyi Biotec, Bergisch Gladbach, Germany), 1:50 diluted in PBS with 10 % FBS. Additionally, 5 $\mu\text{g}/\text{mL}$ 4',6-Diamidin-2-phenylindol (DAPI, Sigma-Aldrich Chemie GmbH, Munich, Germany) was mixed to the antibody solution to counterstain the cell nuclei. A volume measuring 50 μL of this mixture was added on each material surface for 20 min in the dark. The cells were then washed as described above and the samples were put on an object carrier for microscopy. Images of three randomly chosen positions on each material were taken with a confocal laser scanning microscope with the software LAS X (Leica, Wetzlar, Germany) and appropriate filter settings required for the fluorophores (Table 6).

Table 6. Excitation and emission wavelengths for Ki-67 visualization in the coculture.

Target	Excitation laser wavelength	Emission wavelength
DAPI	405 nm	461 nm
Saos-eGFP	488 nm	507 nm
anti-Ki-67-PerCP-Vio700	488 nm	704 nm
RF Fibroblasts	552 nm	602 nm

Quantification of IL-8 and P-SMAD2/SMAD3

An enzyme-linked immunosorbent assay (ELISA) is based on the binding of an antigen to enzyme-linked antibodies, which results in a proportional, measurable color reaction to quantify the analyte in a cell culture supernatant or cell lysate. One subtype of the ELISA is the “Sandwich ELISA” that relies on the enclosed binding of two antibodies to the antigen, as shown in Figure 11. The used ELISAs were either the PathScan (Cell Signaling Technology, Danvers, MA, USA) or DuoSet system (R&D System, Minneapolis, MN, USA).

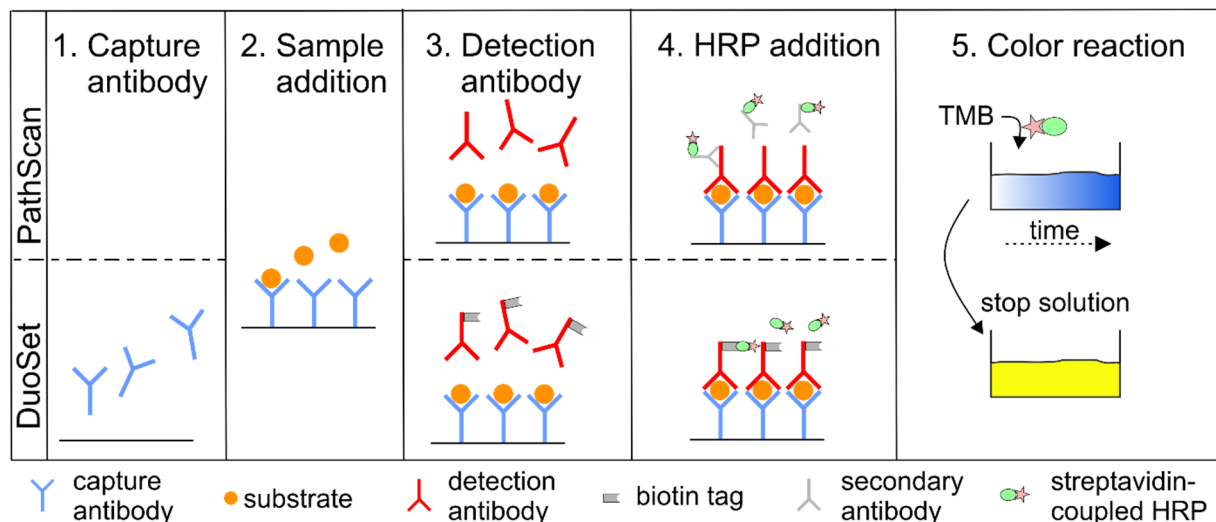


Figure 11. Procedures of two sandwich ELISA. The PathScan® ELISA plates were already coated with the capture antibody (1), while this step has to be performed in the DuoSet system prior to sample addition (2). This is followed by detection of the sample with another antibody (3) and addition of the reporter enzyme horseradish peroxidase (HRP) to catalyze the final color reaction using 3,3',5,5'-tetramethylbenzidine (TMB) (5).

Materials and methods

All ELISAs were conducted as suggested by the different manufacturers, however the basic principle is similar for all. First, a capture antibody is immobilized on a surface-treated microtiter plate. After the incubation with the test sample that contains the target protein, a second antibody (detection antibody) is added that is directed to another binding site of the protein. In this step the target protein is sandwiched between both antibodies. In a next step, a reporter enzyme is added to each sample to catalyze a color reaction that was measured with a microplate reader (Sunrise™ Tecan microplate reader; Tecan, Männedorf, Switzerland). A dilution series with known concentrations of the target protein can be used to quantify the unknown protein concentration in the test samples (Table 7).

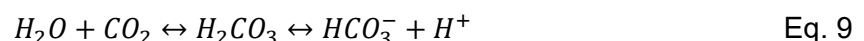
Table 7. ELISA types to quantify IL-8 and P-SMAD2/SMAD3.

Protein	Kit name	Supplier
IL-8	Human IL-8 DuoSet ELISA	R&D System, Minneapolis, MN, USA
P-SMAD2/SMAD3	PathScan® Phospho-Smad2 (Ser465/467)/Smad3 (Ser423/425) Sandwich ELISA	Cell Signaling Technology, Danvers, MA, USA

3.5.2 Impact of Mg degradation on cell proliferation with special focus on varying selected surface-near effects

To investigate which Mg degradation-dependent surface-near effects (i.e., increase in pH, osmolality, and Mg concentration) influence the cell proliferation, single parameter solutions were prepared with increased pH, osmolality, or Mg concentration. Mg extracts were prepared according to the international standard EN ISO 10993 and used to increase the Mg concentration. Briefly, Mg cubes were immersed in normal cell culture medium (0.2 g Mg/mL medium) for 72 h and sterile filtered (0.02 µm CA syringe filter, Thermo Fisher Scientific, Waltham, MA, USA). Afterwards, the Mg concentration was measured using AAS as described in chapter 3.3 and diluted adequately to 30 mM and 5 mM. These concentrations were chosen according to the varying intracellular Mg²⁺ concentrations and Mg concentrations during Mg degradation.

The pH increase was simulated with a decreased CO₂ concentration (0.7 %) in the incubator (BBD 6220, Thermo Electron LED GmbH, Langenselbold, Germany). DMEM comprises a bicarbonate buffer system that is adjusted to buffer the pH at a CO₂ level between 5-10 %. Decreasing the CO₂ level in the incubator leads to a decreased CO₂ fraction that dissolves in the medium and forms carbonic acid, shifting the equilibrium towards the bicarbonate, which results in elevated pH values [167,168]. Eq. 9 describes this phenomenon:



The resulting pH was monitored after 2 h of CO₂ reduction with an ISFET pH sensor (Sentron SI600, Sentron Europe BV, Roden, The Netherlands).

The degradation-induced osmolality increase was mimicked with polyethylene glycol (PEG) 400 that was diluted in cell culture medium to a concentration of 60 mM. The resulting osmolality was monitored directly with a freezing point osmometer 'Osmomat Auto' (Gonotec GmbH, Berlin, Germany).

Cells were seeded in a coculture on glass slides in 24-well plates as described in chapter 3.3. After the cell adherence, medium was changed to the selected conditions and incubated further. Samples treated with solutions with increased osmolality and Mg content were incubated under normal cell culture, while samples treated with increased pH were kept under low CO₂ conditions. Images of the cells were taken after one, three and seven days and the cell numbers were analyzed as described in chapter 3.3. Additionally, Ki-67 expression was visualized as described in chapter 3.5.1 at day 7.

3.6 Analysis of the metastatic potential of the coculture

3.6.1 Cell movements and invasion-related cytokines

Cell migration was analyzed using the scratch assay and cell invasion was examined in a Boyden chamber system in order to analyze the impact of Mg-based materials and their degradation-dependent surface-near effects on cell motility. The scratch assay is a 2D method, which is based on the production of a cell-free area that is closed by the cells over time. It can be performed on any cell culture plate and allows a real-time observation [169]. The Boyden chamber assay is a 3D transmembrane method that was originally designed to study chemotaxis. Cells are seeded on one side of the membrane and are allowed to cross the membrane [169]. Subsequently, the chemotactic potential is assessed by counting the cell numbers that crossed the membrane. Additionally, cancer cell metastasis is initiated by cell-cell adherence loss and degradation of the surrounding ECM. MMPs, especially MMP-2 and MMP-9 are the major enzymes that lead to this ECM breakdown to undergo metastasis, whereas TIMP-1 inhibits MMP activity.

2D cell migration

Cell migration was investigated via the scratch assay (Figure 12). Prior to seeding, both cell types were starved with serum-free DMEM overnight and then treated with mitomycin c (MMC) (Saos-eGFP: 10 µg/mL; RF Fibroblasts: 50 µg/mL) for 2 h to inhibit cell proliferation. Additionally, viability of mitomycin c treated cells was monitored to exclude cytotoxic effects of this treatment. Subsequently, the cells were washed three times with PBS and a total of 50,000 cells (monocultures, 1:1 coculture) was seeded into 12-well plates (25,000 cells in 24-well plates for single parameter assay) and allowed to adhere for 24 h. Then, a cell-free area was created by vertically scratching the cell layer of each well with a pipette tip (20-200 µL). Ground, cleaned, and sterilized Mg and Mg-6Ag samples were transferred into 12-well inserts (3 µm pores, high density, translucent, Corning Inc., Corning, NY, USA) and placed above the cells. Therefore, this experimental set-up represents an indirect contact, in contrast to the cytotoxicity and cell proliferation analyses (chapter 3.4 and 3.5.1). Microscopic images of the interface between the migratory cell front and the cell-free area were taken with an inverse fluorescence microscope (Eclipse Ti-S; Nikon GmbH, Dusseldorf, Germany) after 0, 24 and 48 h. The size of the cell-free areas in the image sections was quantified using ImageJ (Rasband, W.S., ImageJ, U.S. National Institutes of Health, Bethesda, MD, USA, <https://imagej.nih.gov/ij/>, 1997–2018). Relative cell-free areas after 24 and 48 h were then calculated in relation to the size of the initial cell-free area.

Materials and methods

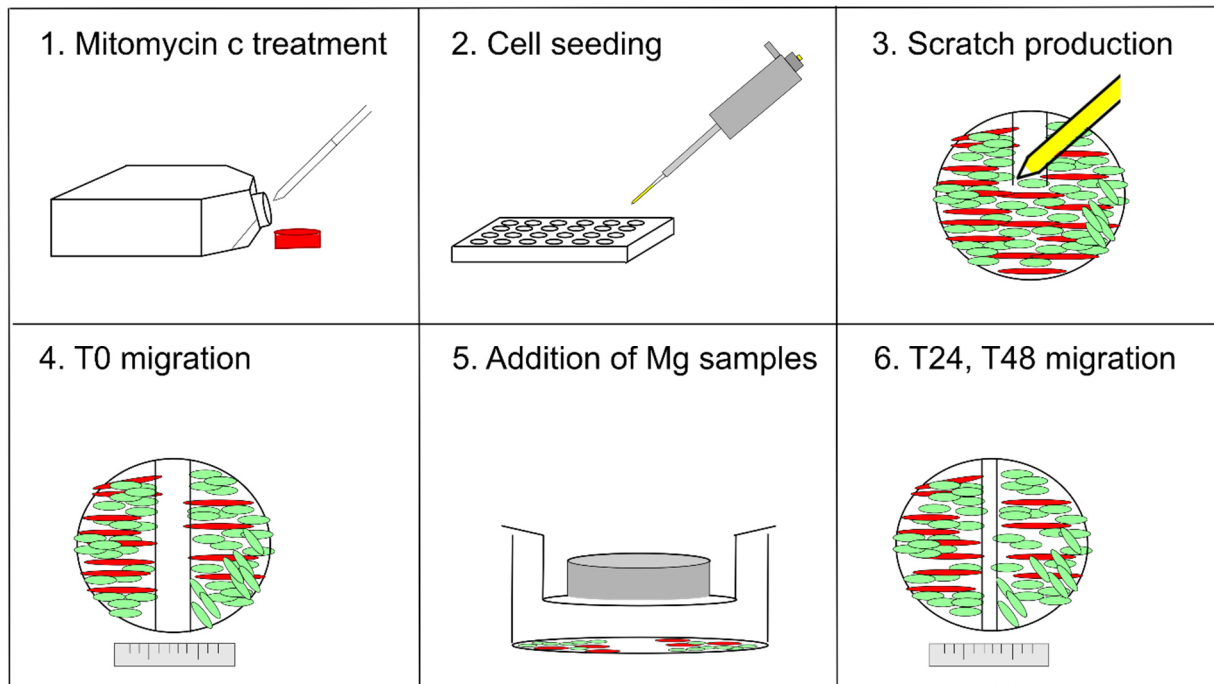


Figure 12. Procedure of the scratch assay. Cells were proliferation inhibited (1) and seeded into a 12-well plate (2). A cell-free area was produced in the dense monolayer of Saos-eGFP (green) and RF Fibroblasts (red) (3) and measured after indicated time points (4-6).

3D cell invasion

Figure 13 shows the procedure of the invasion assay using Saos-eGFP and RF Fibroblasts based on the Boyden chamber method.

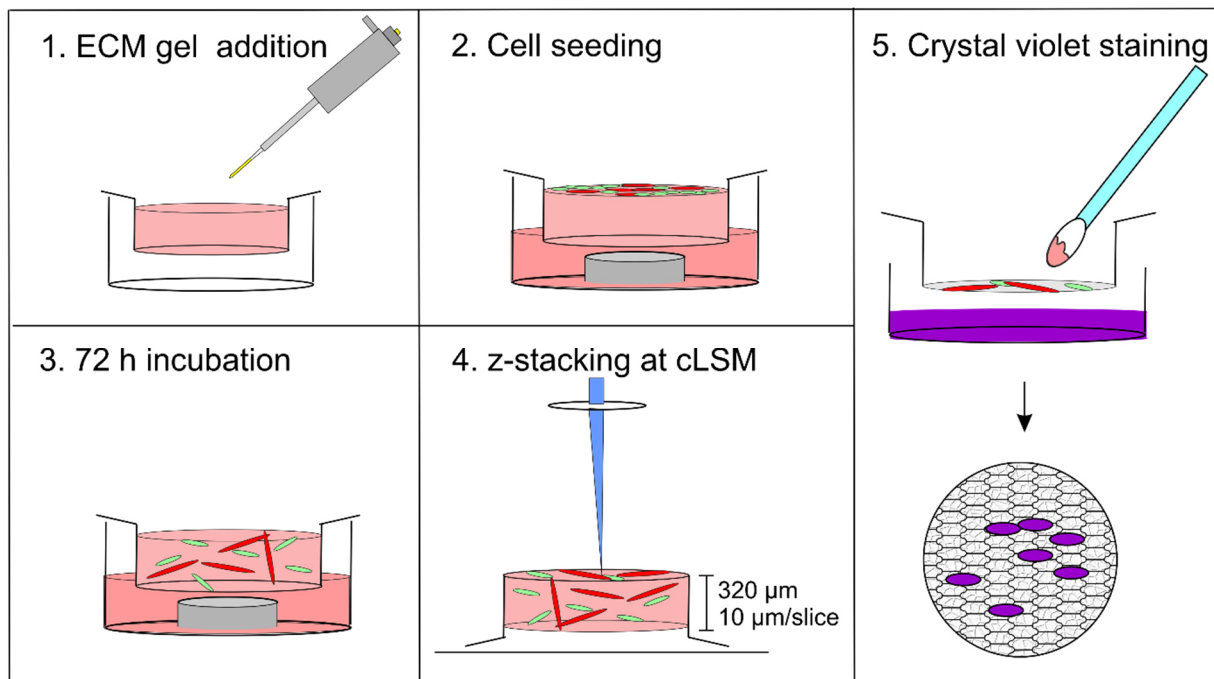


Figure 13. 3D cell invasion assay. Saos-eGFP (green) and RF Fibroblasts (red) were added to the prepared ECM-like matrix (1-2). After 72 h, a z-stack of each sample was recorded (3-4) with a step size of 10 μm . Subsequently, the gel was removed and cells on the membrane were stained with crystal violet (5).

PureCol™ EZ Gel solution (Sigma-Aldrich Chemie GmbH, Munich, Germany) consisting of 5 mg/mL purified Type I bovine collagen was used to simulate the ECM in the TME. The gel solution was diluted 1:4 with serum-free DMEM and 50 µL were loaded into each 24-well cell culture insert (Sarstedt AG & Co. KG, Nümbrecht, Germany) with 8 µm pores to ensure cell passage. The inserts were placed in 24-well plates with carrier plates (Thermo Fisher Scientific, Waltham, MA, USA) and incubated at 37 °C for 1.5 h to allow the gel to solidify. Then, 50,000 cells (Saos-eGFP and RF Fibroblasts) were seeded in coculture or monocultures in a volume of 250 µL in DMEM supplemented with 0.5 % FBS into the upper chamber. Ground, cleaned, and sterilized Mg and Mg-6Ag was placed into the lower chamber in 1 mL cell culture medium. The higher FBS concentration in the lower compartment built a gradient of FBS to attract the cells to pass through the ECM and the membrane. After 72 h, the inserts were placed upside down on an object slide and z-stacks of three positions of the gel (320 µm length, 10 µm/step) were taken by a cLSM. Afterwards, the gel was carefully removed from the insert with a cotton swap and the membrane was stained with 0.05 % crystal violet solution (Merck KGaA, Darmstadt, Germany) in ethanol for 10 min. The membranes were washed three times with PBS and remaining staining solution was removed with a cotton swap. Cells that passed the gel and adhered to the bottom side of the membrane were visualized with an inverse fluorescence microscope (Eclipse Ti-S; Nikon GmbH, Dusseldorf, Germany) using brightfield light. To compare the invasive potential of the cells in the different conditions, the stack slices with the maximal fluorescence intensity were provided by the software of the cLSM (LAS X, Leica, Wetzlar, Germany). Fluorescence intensities of all slices were measured with ImageJ (Rasband, W.S., ImageJ, U.S. National Institutes of Health, Bethesda, MD, USA, <https://imagej.nih.gov/ij/>, 1997–2018). Furthermore, cells that migrated through the membrane were stained with crystal violet and counted from five randomly chosen positions by eye.

MMP-2, MMP-9, and TIMP-1 content

The content of MMP-2, MMP-9 and TIMP-1 in the cell culture supernatant of the coculture on Mg and Mg-6Ag were determined with an ELISA (Table 8) similar to IL-8 quantification described in chapter 3.5.1

Table 8. ELISA types to quantify MMP-2, MMP-9, and TIMP-1.

Protein	Kit name	Supplier
MMP-2	Human MMP-2 DuoSet ELISA	R&D System, Minneapolis, MN, USA
MMP-9	Human MMP-9 DuoSet ELISA	
TIMP-1	Human TIMP-1 DuoSet ELISA	

3.6.2 Analysis of cell migration under specific surface-near effects

The proliferation of the Saos-eGFP and RF Fibroblasts coculture was inhibited using MMC treatment as described in chapter 3.6.1. Afterwards, a total number of 25,000 cells (1:1 Saos-eGFP:RF Fibroblast cell ratio) was seeded into a 24-well plate and was allowed to adhere. Then, a cell-free area was created by scratching with a pipette tip (20-200 µL). The medium was changed to the single parameter solutions (with increased osmolality and Mg²⁺ concentration (5 and 30 mM)), or normal medium under low CO₂ level, as described in chapter 3.5.2. Images were taken with an inverse fluorescence microscope (Eclipse Ti-S; Nikon GmbH, Düsseldorf, Germany) and relative cell-free areas were measured with ImageJ (Rasband,

W.S., ImageJ, U.S. National Institutes of Health, Bethesda, MD, USA, <https://imagej.nih.gov/ij/>, 1997–2018) as previously described in chapter 3.6.1

3.7 NK cell-coculture interaction with Mg-based materials

3.7.1 NK cell activation during Mg degradation

Quantification of cell numbers upon NK incubation

To assess the NK cell activation during Mg degradation, the influence of Mg-based materials on NK cells reducing cancer cell number was measured. The coculture (Saos-eGFP and RF Fibroblasts) was seeded on Mg and Mg-6Ag and incubated for three and seven days as described in chapter 3.3. Then, the suspension cells NK-92 were stained with Hoechst 33342 for 30 min in serum-free α -MEM. Afterwards, the cells were centrifuged and resuspended in fresh NK cell medium. A total number of 50,000 NK cells suspended in 2 mL medium were added per well containing the materials with the coculture and incubated for 4 h in the incubator. Hereafter, images of the Mg-based materials were taken with an epi-fluorescence microscope (Nikon Eclipse Ni, Nikon GmbH, Dusseldorf, Germany). Controls on glass were visualized with an inverse fluorescence microscope (Eclipse Ti-S; Nikon GmbH, Dusseldorf, Germany) using the DAPI (NK cells), FITC (Saos-eGFP) and TexasRed filter (RF Fibroblasts). The coculture incubated without NK cells served as control. Resulting cell numbers of cancer and healthy cells, as well as the consequent cell ratios, were determined with ImageJ (Rasband, W.S., ImageJ, U.S. National Institutes of Health, Bethesda, MD, USA, <https://imagej.nih.gov/ij/>, 1997–2018) (compare 3.3).

Granzyme B and perforin content

Granzyme B and perforin are granular proteins that are secreted by NK cells upon activation, which may be stimulated by Mg degradation. Therefore, the concentration of both proteins in the supernatant was measured to assess NK cell activity and cytotoxic potential against tumor cells. The supernatant granzyme B and perforin contents were determined with an ELISA (Table 9) similar to IL-8 quantification described in chapter 3.5.1

Table 9. ELISA types to quantify granzyme B and perforin.

Protein	Kit name	Supplier
Granzyme B	Human Granzyme B DuoSet ELISA	R&D System, Minneapolis, MN, USA
Perforin	Human Perforin ELISA BASIC kit (HRP)	Mabtech, Nacka Strand, Sweden

3.8 Analysis of cancer cell induced angiogenesis

3.8.1 Preparation of conditioned media

The experimental set-up for investigating the influence of Mg-based materials on angiogenesis was chosen as follows: Saos-eGFP and RF Fibroblasts were seeded in coculture (CC) and monocultures (MCS, MCF) on Mg-based materials and glass in direct contact as described in chapter 3.3. From this, supernatants (conditioned media) were harvested and incubated with HUVEC (indirect contact). Subsequently, analysis of HUVEC can be conducted to assess cancer cell induced angiogenesis. Conditioned media were harvested after one, three and seven days, and fresh medium was added to the coculture system. For all methods that relate

to cancer cell induced angiogenesis, the conditioned media were prepared and applied as shown in Figure 14.

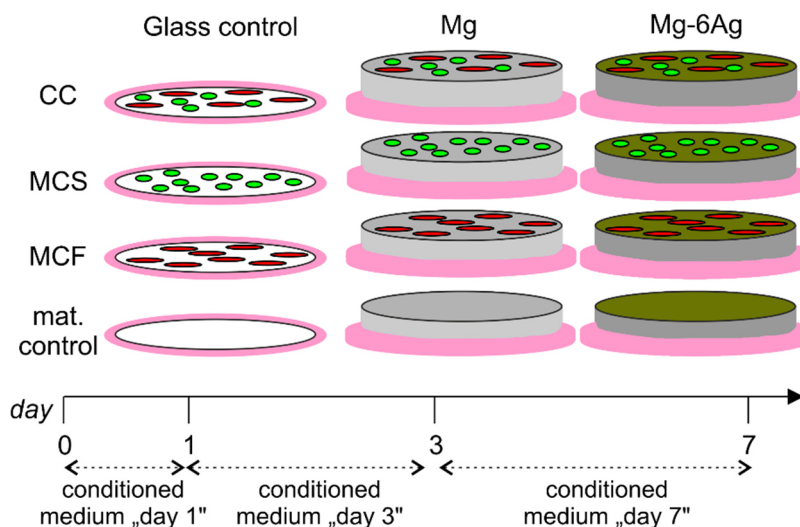


Figure 14. Conditioned media preparation and application. Mg, Mg-6Ag or glass slides (glass control) were seeded with the coculture (CC), the monocultures of Saos-eGFP (MCS) or RF Fibroblasts (MCF), or without cells (mat. control). Supernatants were harvested after one, three and seven days.

Between cell seeding (day 0) and day 1, the conditioned media harvested at day 1 were used. Conditioned media harvested at day 3 were applied between day 1 and day 3. Eventually, conditioned media from day 7 were added with the medium change at day 3 until the end of the experiment.

3.8.2 Endothelial cell permeability and proliferation - VEGF content

Permeability

During the first step of angiogenesis, interendothelial cell connections become leaky and allow the extravasation of basement membrane degrading proteins. Therefore, the influence of Mg-based materials on the HUVEC permeability was qualitatively assessed by the passage of a fluorescently labeled dextran (FITC-Dextran). Initially, 50,000 HUVEC were seeded in 24-well transwell inserts (0.4 μm pores, Thermo Fisher Scientific, Waltham, MA, USA) hold in the 24-well plate with a carrier plate on top (Thermo Fisher Scientific, Waltham, MA, USA). The cells were allowed to form a dense monolayer for 72 h, followed by a medium change to the different conditioned media (see chapter 3.8.1). After an incubation for three and seven days in the incubator under normoxia and hypoxia, 25 $\mu\text{g}/\text{mL}$ FITC-dextran were applied to the upper compartment. Then, the 24-well plate was shaken at 60 rpm for 1 h in a MaxQ™ 4000 Benchtop Orbital Shakers (Thermo Fisher Scientific, Waltham, MA, USA) while being protected from light. Afterwards, the content of the lower compartment was distributed to a 96-well plate in triplicates (100 μL) and fluorescence was measured with the Victor³ multilabel plate reader (PerkinElmer, Inc., Waltham, MA, USA) with an excitation wavelength of 485 nm and emission wavelength of 535 nm. To quantify the concentration of FITC-dextran that passed the HUVEC monolayer and the insert membrane, a serial dilution of known FITC-dextran concentrations was also measured for every plate. Figure 15 summarizes the basic principle of this procedure.

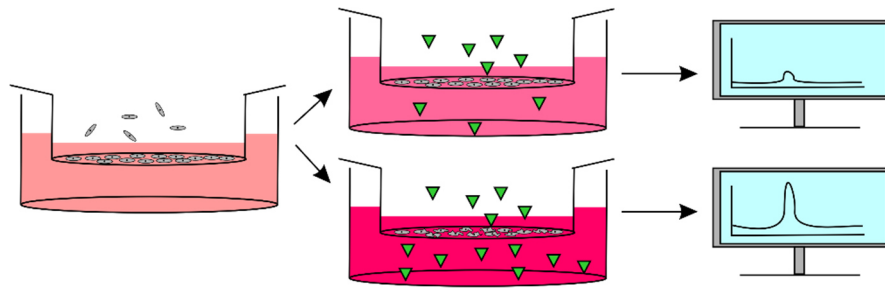


Figure 15. Procedure to measure endothelial cell permeability. More permeable cell layers allow the passage of a dye and result in higher fluorescence intensity values.

Proliferation

The HUVEC proliferation was measured in response to the conditioned media (see chapter 3.8.1). Therefore, 2,000 HUVEC were seeded into every well of a 96-well plate and allowed to adhere overnight. Then, HUVEC were initially stained with 100 μL per well of 2 $\mu\text{g}/\text{mL}$ Hoechst 33342 in serum-free medium for 15 min in the incubator. Fluorescence was excited at a wavelength of 355 nm and fluorescence intensity was measured at 460 nm with a Victor³ multilabel plate reader (PerkinElmer, Inc., Waltham, MA, USA). Afterwards, the medium was changed to the “day 3” conditioned medium and incubated under normoxia and hypoxia. After three and seven days, this procedure was repeated. The resulting fluorescence intensities were calculated as relative fluorescence intensities from the initial time point.

VEGF content

VEGF regulates almost all steps of angiogenesis. To investigate the influence of Mg-based materials on VEGF expression, VEGF content in the supernatant harvested from the HUVEC migration experiment was determined with a Human VEGF DuoSet ELISA (R&D System, Minneapolis, MN, USA) similar to IL-8 quantification described in chapter 3.5.1.

3.8.3 Endothelial cell migration and tube formation

2D Migration

Aside from proliferation, endothelial cell migration is essential to form new blood vessels from preexisting ones. To analyze the influence of Mg-based materials on the HUVEC migration, the 2D migration procedure, described in chapter 3.6.1 was slightly changed. HUVEC were seeded into 24-well plates (50,000 cells) in ECGM and grown to a confluent monolayer. Afterwards, the cells were starved in ECGM without supplement overnight and treated with 10 $\mu\text{g}/\text{mL}$ mitomycin c as described before. After scratching the monolayer, medium was changed to the conditioned media (see chapter 3.8.1) and images of the HUVEC were taken after 0, 24 and 48h with an inverse fluorescence microscope using the brightfield mode. Analysis and calculations were conducted as described in chapter 3.6.1.

Tube formation

The tube formation assay is another method to measure angiogenic stimuli of different conditioned media. The principle is based on the differentiation of endothelial cells into capillary structures on a basement membrane matrix (Figure 16). Then, angiogenesis can be assessed due to tube numbers and lengths, branching points, junctions or isolated segments.

Geltrex® LDEV-free reduced growth factor basement membrane matrix (Thermo Fisher Scientific, Waltham, MA, USA) was thawed overnight at 4 °C. Then, 15 μL of the basement membrane matrix were applied into each well of a 96-well plate and allowed to solidify in the incubator for 30 min. Subsequently, 10,000 HUVEC were seeded in ECGM into each well and

allowed to adhere for a further 30 min. This was followed by a medium change to the conditioned medium (see chapter 3.8.1) and an incubation for 6 h. Then, medium was aspirated. A staining solution containing 1 μM calcein-AM was added to the cells for 30 min. Images of the HUVEC were taken with an inverse fluorescence microscope (Eclipse Ti-S; Nikon GmbH, Dusseldorf, Germany). The images were analyzed with ImageJ and the free plugin: “Angiogenesis analyzer” for the number of branches and isolated segments [170].

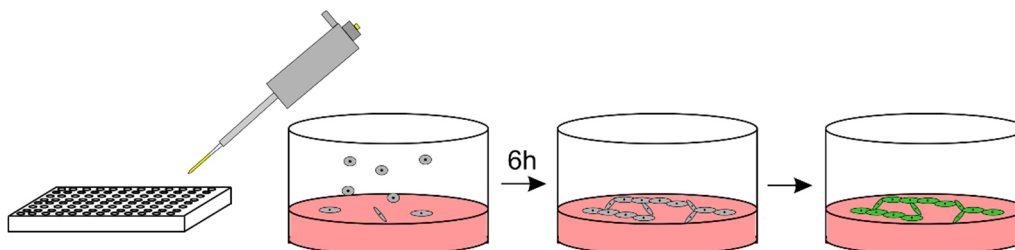


Figure 16. Principle to measure the tube formation ability of endothelial cells. HUVEC form tube-like structures on a basement membrane.

3.9 Statistical analyses

If not stated otherwise, the obtained results refer to three independent experiments with indicated numbers of replicates. For degradation test by weight loss and the related measurements (pH, osmolality) six replicates were used. Scans of the cell-seeded materials for cell counting were conducted with three replicates. Microscopic images that were conducted with a higher magnification with the cLSM (Ki-67, ROS, Caspase-3) were performed with two replicates but at least 3 randomly chosen positions per replicate, if not other stated. Some antibodies and reagents for e.g. cell staining or ELISAs were limited. Therefore, some results were obtained with only two independent experiments.

The data are presented and analyzed using Prism (version 6, GraphPad Software, La Jolla, USA) with different statistical test, each stated under the respective figure. To compare three or more groups a Kruskal-Wallis H test with Dunn’s multiple comparison test was performed. A two-way ANOVA with Tukey’s multiple comparison test was conducted to compare the influence of two independent variables were.

4 Results

4.1 Characterization of an osteosarcoma-fibroblast coculture on slow degrading Mg-based materials

In a first step, Saos-eGFP and RF Fibroblast growths were studied and appeared to be comparable in monocultures on tissue culture plastic (Figure 17A) before seeding them as cocultures on Mg, Mg-6Ag and Ti-6Al-4V disks (Figure 17B).

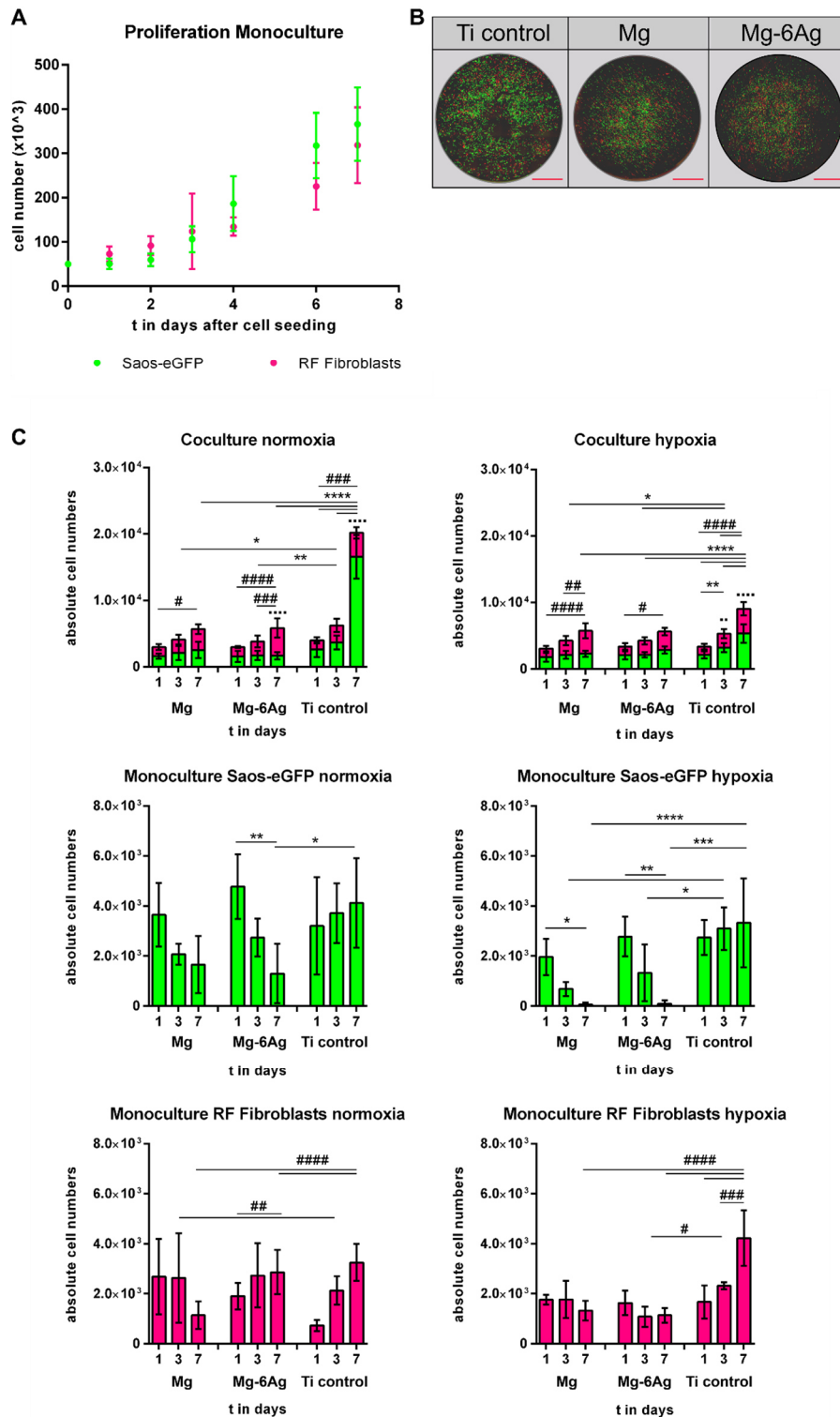
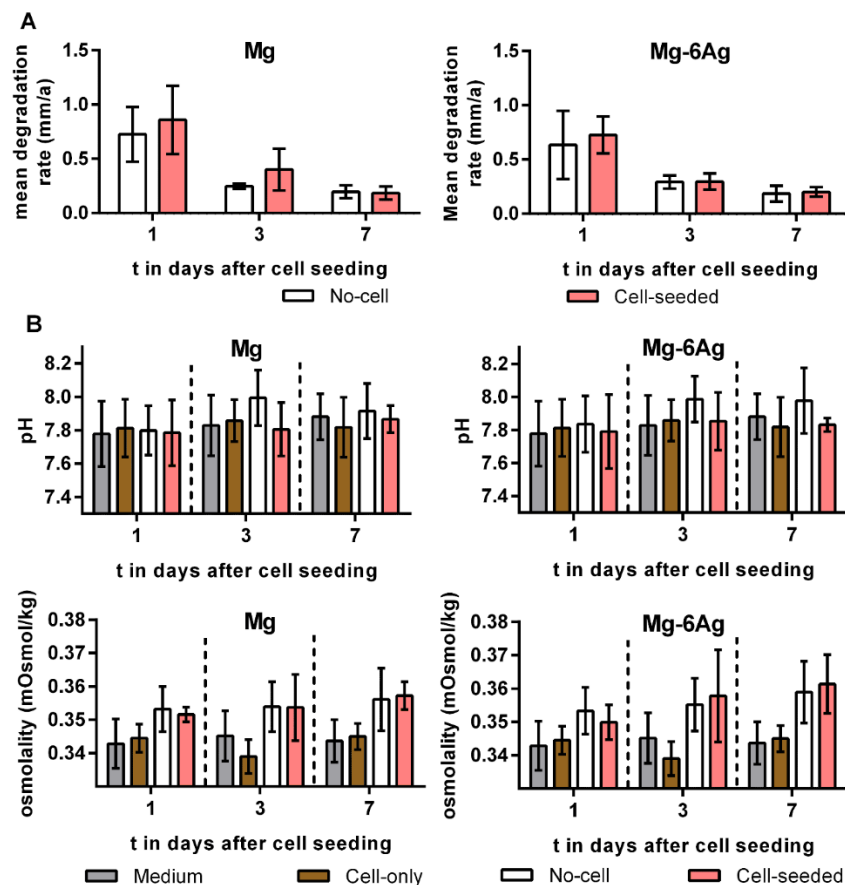


Figure 17. Cell viability of Saos-eGFP and RF Fibroblasts on Mg-based materials. (A) Proliferation of Saos-eGFP (green) and RF Fibroblasts (magenta) in monocultures on tissue culture plastic. (B) Coculture of Saos-eGFP and RF Fibroblasts (1:1 ratio) on Mg, Mg-6Ag and Ti-6Al-4V (Ti control) as exemplary images. Scale bar is 2.5 mm. (C) Cell numbers of the coculture and monocultures on Mg, Mg-6Ag and the Ti control one, three and seven days after cell seeding. Cell numbers are presented as mean \pm SD calculated from microscopic images from three independent experiments with three samples per time point. Statistically significant differences between cell numbers of Saos-eGFP (*), RF Fibroblasts (#) or between both cell types (\cdot) on different materials (Mg, Mg-6Ag, Ti control) or time points (day 1, 3, 7) were obtained via a two-way ANOVA with Tukey's multiple comparison test ($n=9$); one symbol = $p < 0.05$; two symbols = $p < 0.01$; three symbols = $p < 0.001$; four symbols = $p < 0.0001$. Figure is adapted from Globig *et al.* [171].

Figure 17C shows the quantification of cancer cell and healthy cell numbers seeded on Mg, Mg-6Ag and Ti-6Al-4V (Ti control) in co- and monocultures under normoxia and hypoxia. Under both conditions, normoxia and hypoxia, cancer cell numbers remained reasonably constant in coculture within seven days on degrading materials (Mg, Mg-6Ag). In contrast to this, cancer cell numbers significantly increased on the non-degrading Ti control, additionally showing significantly higher cell numbers compared to the respective healthy cell numbers in the coculture after seven days. On the other hand, cell numbers of healthy fibroblasts significantly rose within seven days, regardless of the seeding substrate. This was contrary to the results from the monocultures. While the numbers of both cell types appeared to increase on the Ti control, Saos-eGFP numbers decreased and RF Fibroblast numbers remained constant on degrading Mg and Mg-6Ag.

Figure 18A shows that the MDR of the used Mg and Mg-6Ag materials were comparable and in a degradation rate range that allowed further cell tests.



Results

Figure 18. Mean degradation rate, pH and osmolality on material with and without cells. (A) Comparison of mean degradation rates of the used Mg and Mg-6Ag dependent on coculture seeding. (B) Corresponding pH and osmolality values compared to cells without material and a medium control. Resulting mean degradation rates, pH and osmolality values are presented as the mean \pm SD. Statistically significant differences between samples with and without cells at respective time points were obtained via a Kruskal-Wallis H test with Dunn's multiple comparison test ($n=9$).

The MDR was calculated by the mass loss (Eq. 4) one, three and seven days after cell seeding. Both, the MDR of cell-seeded Mg-based material and material without cells did not significantly differ. These results were also confirmed by pH and osmolality measurements (Figure 18B), as well as Mg and Ag quantification in the supernatant up to seven days after cell seeding (Figure 19).

For both materials, supernatant Mg concentration rose within seven days from 2.5-5.0 mM for cell-seeded and no-cell material. In contrast to this, Mg concentration of samples without material (medium, cell-only) remained on a constant level around 0.8 mM, which is the expected concentration in DMEM. For Mg-6Ag with cells, Ag concentration accounted to 0.4-0.5 nM. The medium control and cells on tissue culture plastic (cell-only) were virtually free of Ag.

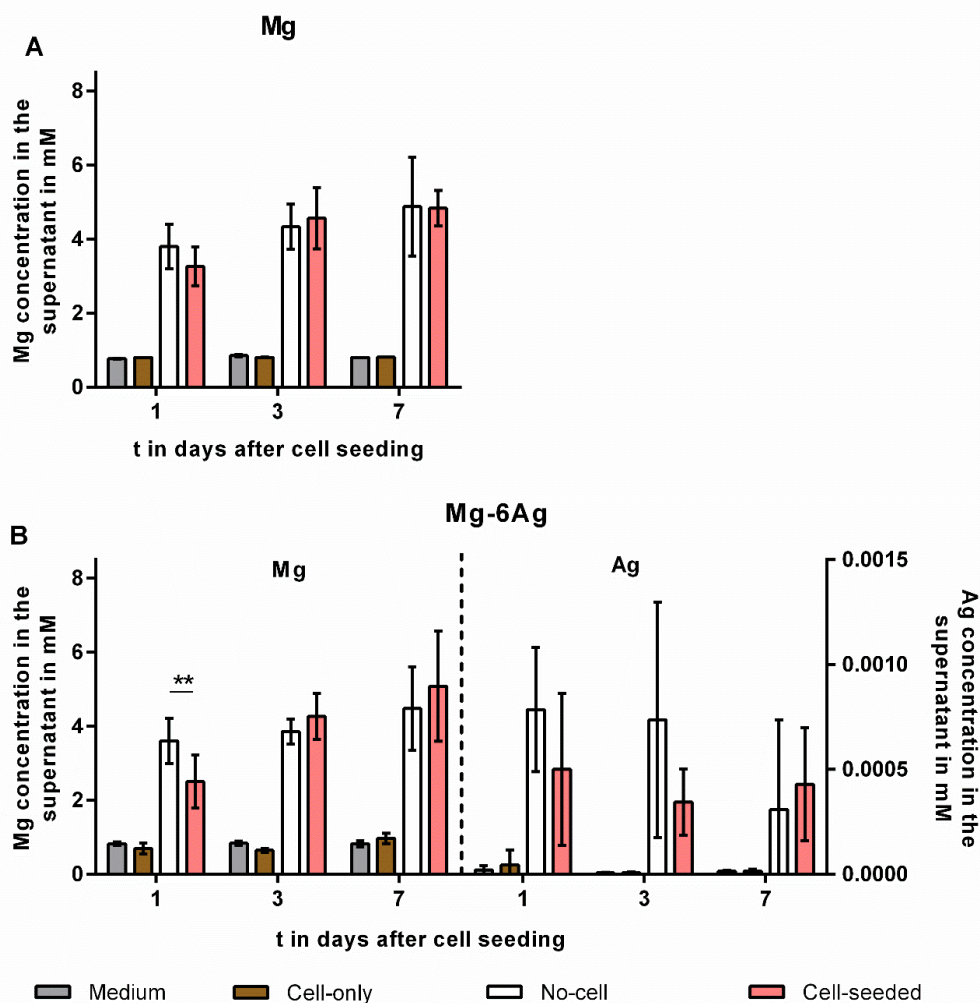


Figure 19. Magnesium and silver concentrations in the supernatant of degrading Mg and Mg-6Ag. Supernatant Mg concentration resulting from Mg degradation was quantified by AAS. (B) Simultaneous quantification of Mg and Ag in the supernatant of Mg-6Ag was performed using ICP-MS. Resulting

supernatant concentrations of Mg and Ag are presented as the mean \pm SD. Statistically significant differences between concentrations at the indicated time points were obtained via a Kruskal-Wallis H test with Dunn's multiple comparison test ($n = 6$ or 9); ** = $p < 0.01$.

4.2 Cytotoxicity of Mg-based materials

Figure 17C revealed constant cancer cell numbers in the coculture. This might be due to an equilibrium of cell death and ongoing cell proliferation. In order to clarify the underlying processes of cellular responses, the cytotoxic potential of slow-degrading Mg and Mg-6Ag was determined using different methods. Figure 20A shows the cytotoxicity of the coculture based on the release of lactate dehydrogenase (LDH). The glass control (cells on glass), as well as cells on Mg and Mg-6Ag did not show any significant differences in the absorbance values of detected LDH. Absolute absorbance values for the coculture on the non-degrading Ti control appeared to be higher compared to Mg and Mg-6Ag. Nevertheless, the LDH release of permeabilized cells (lysis control) was found to be significantly higher compared to Mg, Mg-6Ag and the glass control. These findings suggested integrity of cancer and healthy cells when seeded in coculture on slow-degrading Mg and Mg-6Ag.

The determination of live and dead cells of the coculture on Mg-based materials by flow cytometry indicated similar findings (Figure 20B). The proportion of living cancer cells on Mg (92 ± 11 %), Mg-6Ag (95 ± 5 %) and the Ti control (89 ± 9 %) was slightly, but not significantly, reduced compared to the control on glass (97 ± 2 %). On the contrary, permeabilizing the coculture (lysis control) significantly increased the percentage of dead cancer cells (56 ± 16 %) compared to Mg (8 ± 11 %), Mg-6Ag (5 ± 5 %) and the glass control (3 ± 2 %).

Furthermore, cytotoxicity of Mg and Mg-6Ag was tested by visualizing oxidative stress and a subsequent initiation of apoptosis. Figure 21 shows the ROS production (white) and caspase-3 activity (blue) in cancer cells (green) and healthy cells (red) in response to Mg and Mg-6Ag. The quantification of these images revealed an enhanced ROS production in the fibroblasts within the coculture on Mg and Mg-6Ag compared to the glass control under normoxia. Additionally, in coculture and monoculture under normoxia the oxidative stress in the healthy cells appeared to be higher than in the cancer cells. In contrast to this, the ROS production seemed to be comparable in cancer and healthy cells under hypoxic conditions, though oxidative stress tended to be lower in cancer cells on Mg and Mg-6Ag compared to the glass control. The quantification of caspase-3 activity and thus apoptosis initiation showed no significant differences between degrading material and the negative control in any condition.

Results

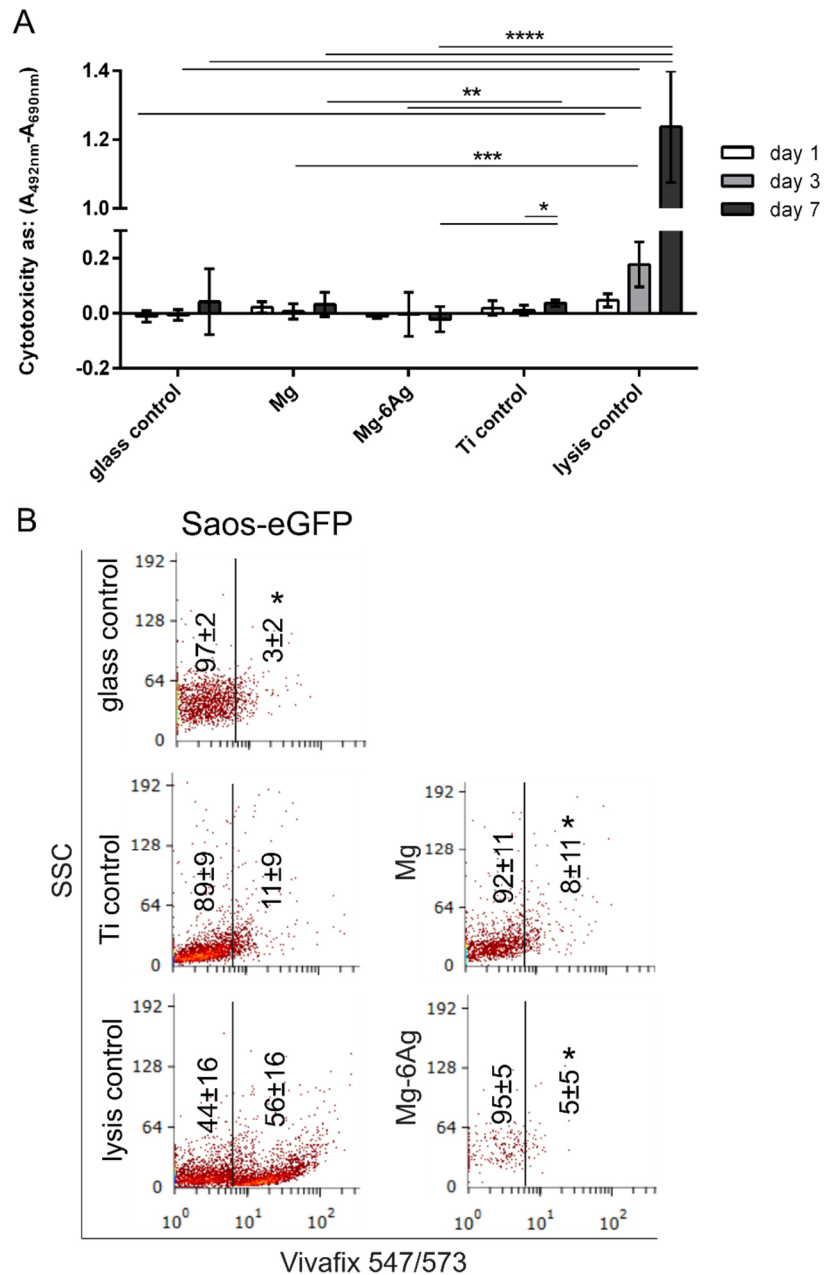


Figure 20. Cytotoxicity of Mg-based materials towards the osteosarcoma-fibroblast coculture under normoxia. Cytotoxicity of Mg and Mg-6Ag was measured and compared to a Ti control, a glass control and a lysis control (Triton-X 100). (A) Background corrected absorbance values of the LDH release in the supernatant and (B) relative live and dead cell numbers determined by flow cytometry are presented as the mean \pm SD. Statistically significant differences between samples on different materials at respective time points were obtained via a Kruskal-Wallis H test with Dunn's multiple comparison test (n=9); * = $p < 0.05$; ** = $p < 0.01$; *** = $p < 0.001$; **** = $p < 0.0001$.

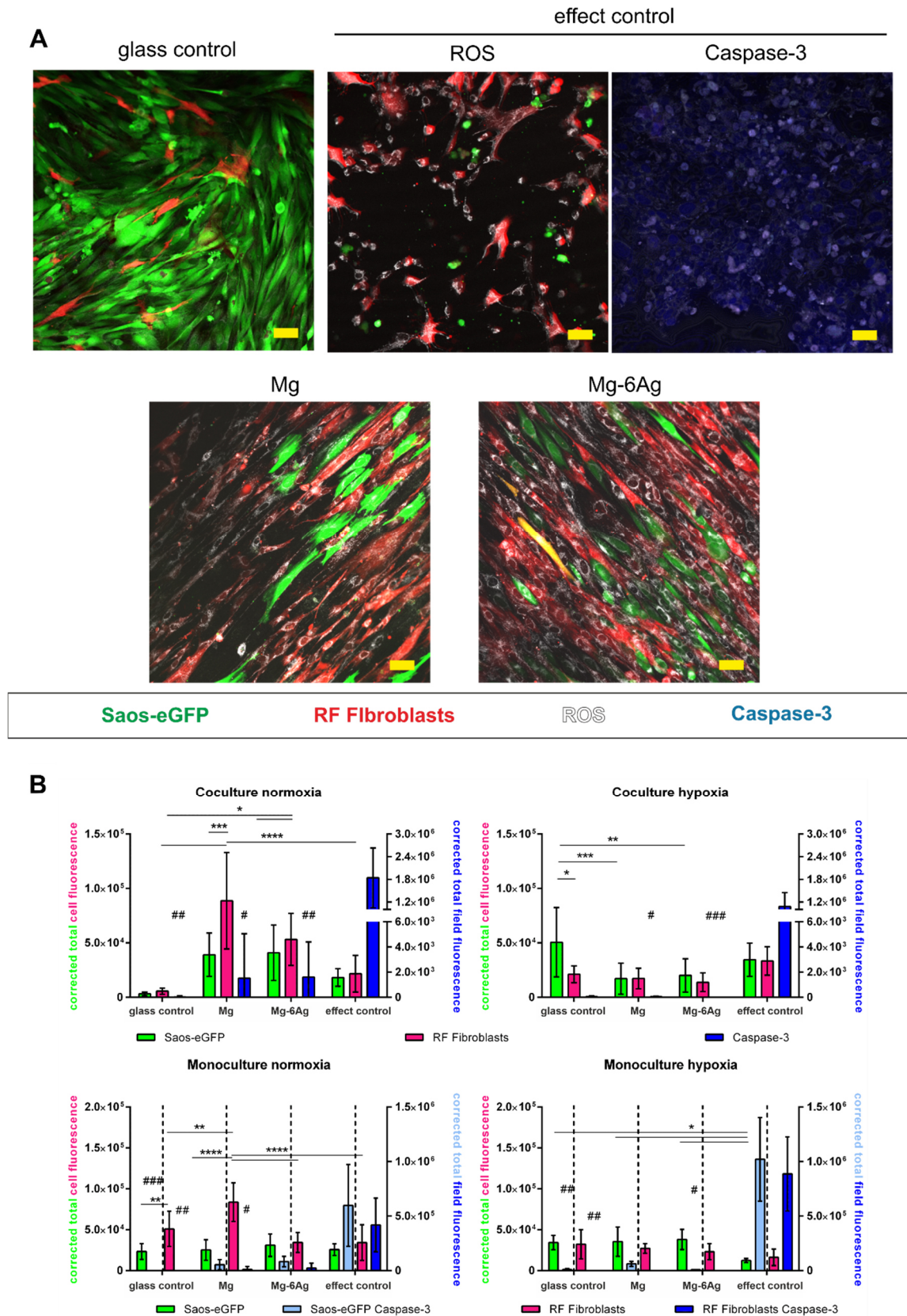


Figure 21. Oxidative stress and apoptosis in response to Mg-based material degradation. (A) Representative images of ROS (white) and caspase-3 activity (blue) in cancer cells (Saos-eGFP, green) and healthy cells (RF Fibroblasts, magenta) on Mg, Mg-6Ag, glass control (without cell treatment), and effect control (glass with a treatment) to provoke apoptosis (atmospheric conditions) and oxidative stress (menadione) seven days after cell seeding. Scale bar is 50 μ m. (B) Quantification of ROS staining

Results

(CTCF) and caspase-3 activity (CTFF) as described in 3.4. Resulting values for CTCF (left y-axis) and CTFF (right y-axis) are presented as the mean \pm SD. Statistically significant differences of CTCF between cell types and materials were obtained via a two-way ANOVA with Tukey's multiple comparison test (n=9); * = $p < 0.05$; ** = $p < 0.01$; *** = $p < 0.001$. Statistically significant differences between CTFF of neg. control, Mg and Mg-6Ag to the pos. control were obtained via a Kruskal-Wallis H test with Dunn's multiple comparison test (n=6); # = $p < 0.05$.

4.3 Influence of Mg-based materials on cancer cell proliferation

4.3.1 Visualization of proliferation marker Ki-67

According to the previous results, slow-degrading Mg and Mg-6Ag did not lead to a detectable cytotoxicity towards the osteosarcoma cells. Therefore, the observation of constant cancer cell numbers (Figure 17C) may hint to an alternative explanation. An inhibited cancer cell proliferation is suggested. To analyze such an inhibited proliferation, Saos-eGFP and RF Fibroblasts were seeded in coculture and monocultures on Mg and Mg-6Ag under normoxia and hypoxia. Subsequently, proliferating cells were visualized by staining of the proliferation marker Ki-67 seven days after cell seeding (Figure 22A). The quantification of the Ki-67 staining showed an overall higher relative number of Ki-67 positive cells under normoxia than under hypoxic conditions (Figure 22B). Furthermore, the relative number of proliferating cancer cells was significantly lowered when seeding cells on degrading material (Mg, Mg-6Ag), which was comparable to proliferation inhibited cells (proliferation inhibition control). In contrast to this, the slower proliferating fibroblasts were not affected by Mg and Mg-6Ag in the coculture. Proliferation inhibition is one feature of cancer cells that acquire a dormancy-like phenotype.

This dormancy-like phenotype entered by the osteosarcoma cells could be reversed when the coculture was detached from Mg and Mg-6Ag and reseeded on glass slides (Figure 23). In doing so, the proportion of Ki-67 positive cancer cells significantly increased from 5-10 % to over 50 %, while the healthy cells seemed to be unaffected.

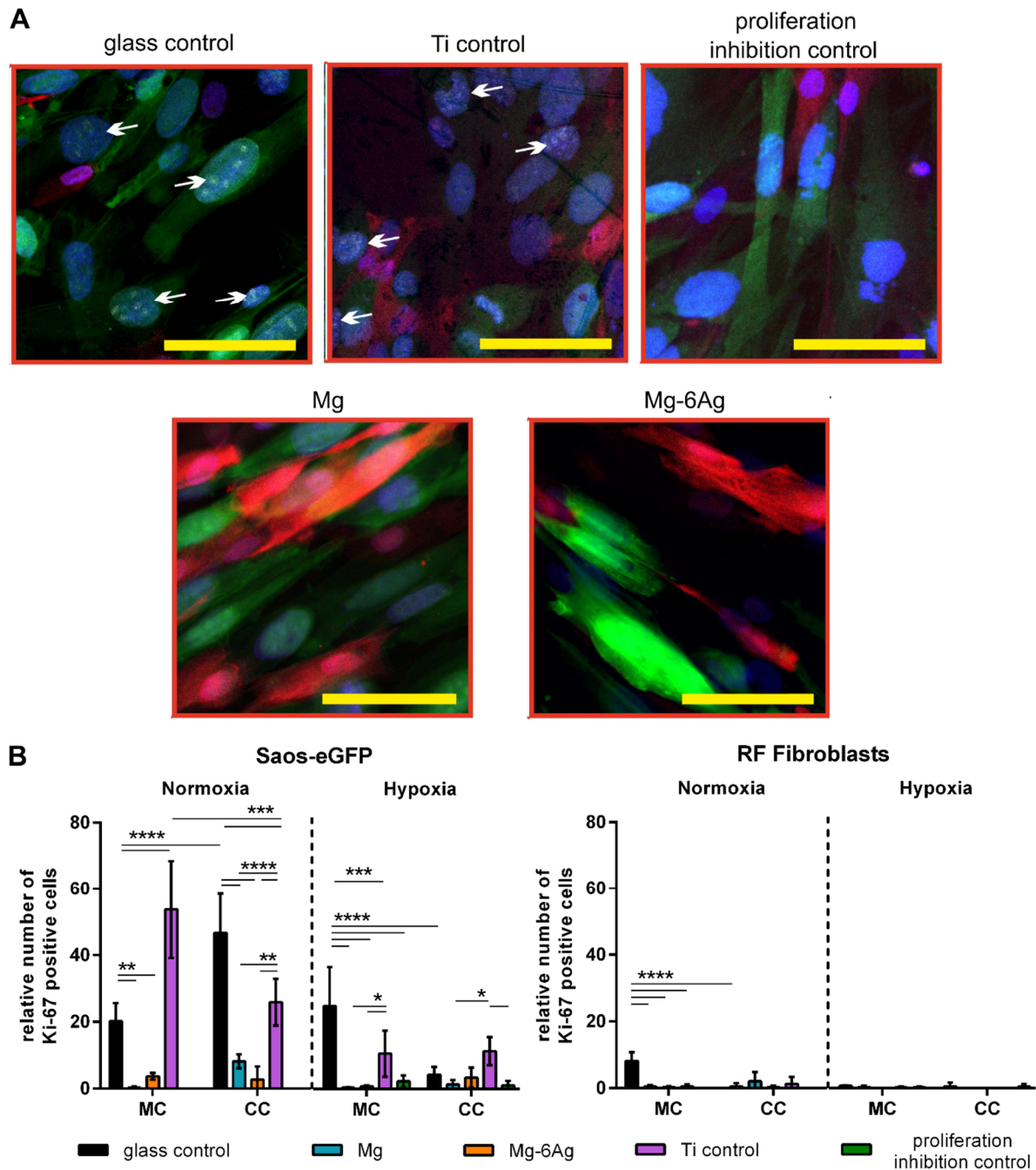


Figure 22. The influence of Mg and Mg-6Ag on Ki-67 expression in the coculture. (A) Representative images of Ki-67 (white) expression in cancer cells (green) and healthy cells (magenta) with nuclei counterstain (blue). White arrows display Ki-67 positive nuclei. Scale bar is 50 μ m. (B) Corresponding quantification of Ki-67 positive cells in monocultures (MC) and coculture (CC). The average number of cells per image was between 20-100 cells. Relative numbers of Ki-67 positive cells are presented as the mean \pm SD from two samples, each with three randomly chosen positions. Statistically significant differences between relative Ki-67 positive cells (oxygen level, material) were obtained via a two-way ANOVA with Tukey's multiple comparison test ($n=6$); * = $p < 0.05$; ** = $p > 0.01$; *** = $p < 0.001$; **** = $p < 0.0001$.

Results

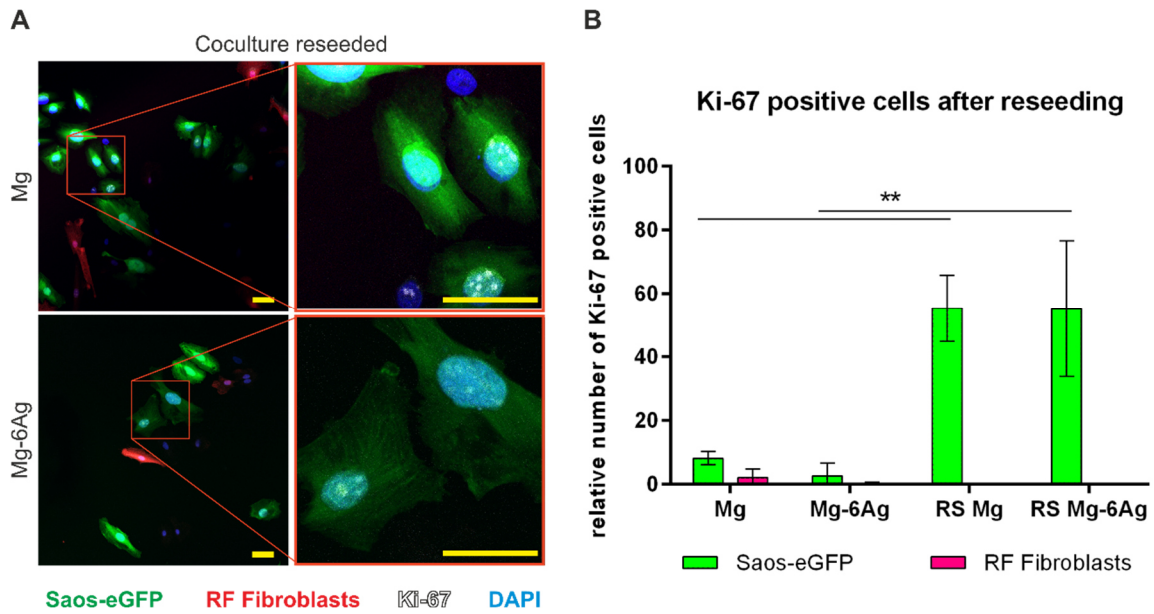


Figure 23. Reversibility of the cancer cell associated dormancy-like phenotype. (A) Cancer cells (green) and healthy cells (magenta) were detached from Mg and Mg-6Ag and stained for Ki-67 (white) and DAPI (blue) 24 h after reseeding on glass slides. Scale bar is 50 μ m. (B) Quantification of relative Ki-67 positive cancer cell (green) and healthy cell (magenta) numbers. The average number of cells per image was between 20-100 cells. Relative Ki-67 positive cells are presented as the mean \pm SD from two samples, each with three randomly chosen positions. Statistically significant differences between relative numbers of Ki-67 positive cells on Mg or Mg-6Ag and their corresponding reseeded samples were obtained via a Mann-Whitney test (n=6); ** = $p < 0001$.

4.3.2 Investigation of the cancer cell proliferation inhibition signaling pathway

In order to clarify specific signaling pathways that are responsible for the observed tumor cell proliferation inhibition when the coculture was seeded on Mg and Mg-6Ag, PERK, IL-8 and TGF- β signaling were investigated. Figure 24 visualizes and quantifies the expression of proliferation marker Ki-67 in response to PERK inhibitor GSK2606414. In the negative control, both, untreated and PERK inhibitor treated samples exhibited equal relative Ki-67 positive cell numbers. These numbers were significantly higher compared to Mg and Mg-6Ag, irrespective of the treatment. Interestingly, cell proliferation did not increase again as a response to the PERK inhibition on both degrading materials.

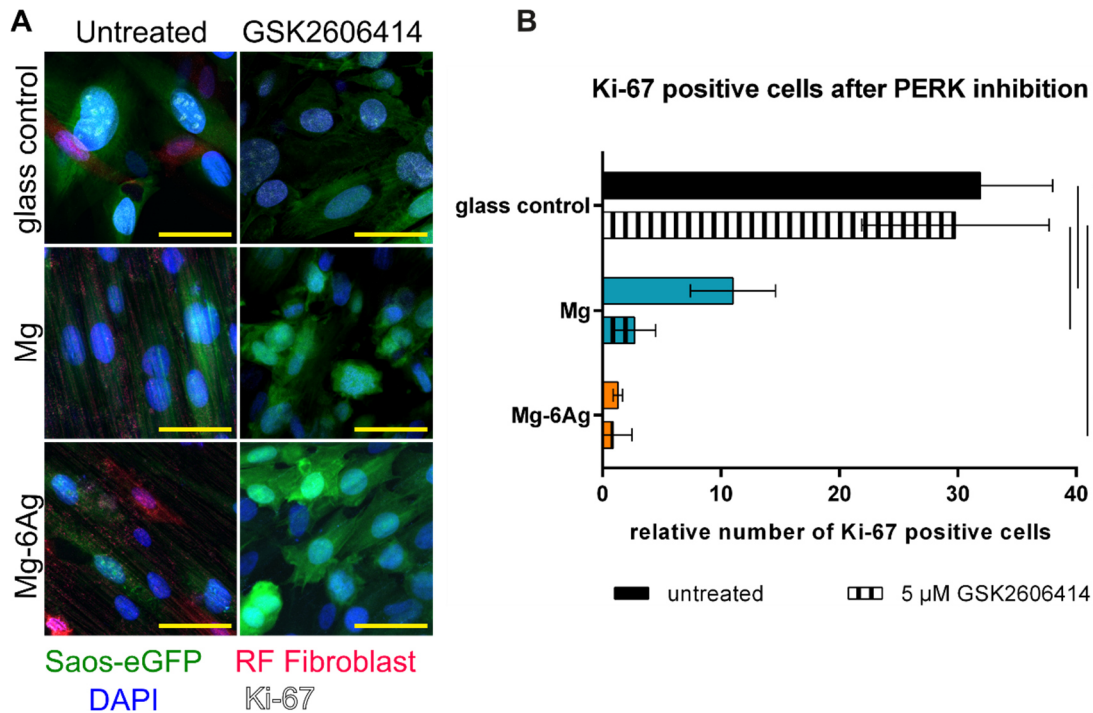


Figure 24. The effect of protein kinase RNA-like endoplasmic reticulum kinase (PERK) inhibition on cancer cell proliferation. (A) Cancer cells (green) and healthy cells (magenta) were stained for DAPI (blue) and Ki-67 expression (white) after incubation with 5 μ M GSK2606414 for 72 h. Scale bar is 50 μ m. (B) Corresponding quantification of relative numbers of Ki-67 positive cells (coculture) presented as the mean \pm SD from two samples, each with three randomly chosen positions. Statistically significant differences between relative Ki-67 positive cells (materials, treatment) were obtained via a two-way ANOVA with Tukey's multiple comparison test ($n=6$); **** = $p < 0.0001$. The average number of cells per image was between 20-100 cells.

Another signaling pathway that can induce cancer cell dormancy includes the transforming growth factor beta (TGF- β). The chemokine TGF- β can reduce cell proliferation by phosphorylation of SMAD2/SMAD3 complex and subsequent transcription of CDK inhibitor p21. Figure 25A indicates the magnitude of absorbance values that are proportional to the concentrations of phosphorylated SMAD2/SMAD3, normalized to the cell numbers. These normalized values did not differ between degrading and non-degrading material under normoxia and hypoxia. IL-8 is a mediator of several cellular signaling pathways and can induce cell proliferation through MAPK, Src kinase and FAK signaling. Figure 25B shows the normalized IL-8 concentration in the supernatant of Mg, Mg-6Ag, Ti control and glass control that were seeded with the coculture for up to seven days. The IL-8 concentration/per cell was initially higher in the glass control compared to degrading Mg and Mg-6Ag under normoxia and hypoxia. This decreased at day 3 and 7, while the normalized IL-8 concentration for the cells seeded on Mg-based materials tended to be higher compared to cells seeded on non-degrading materials (Ti control, glass control). Therefore, neither PERK, TGF- β nor IL-8 are involved in the tumor cell proliferation inhibition observed on Mg and Mg-6Ag.

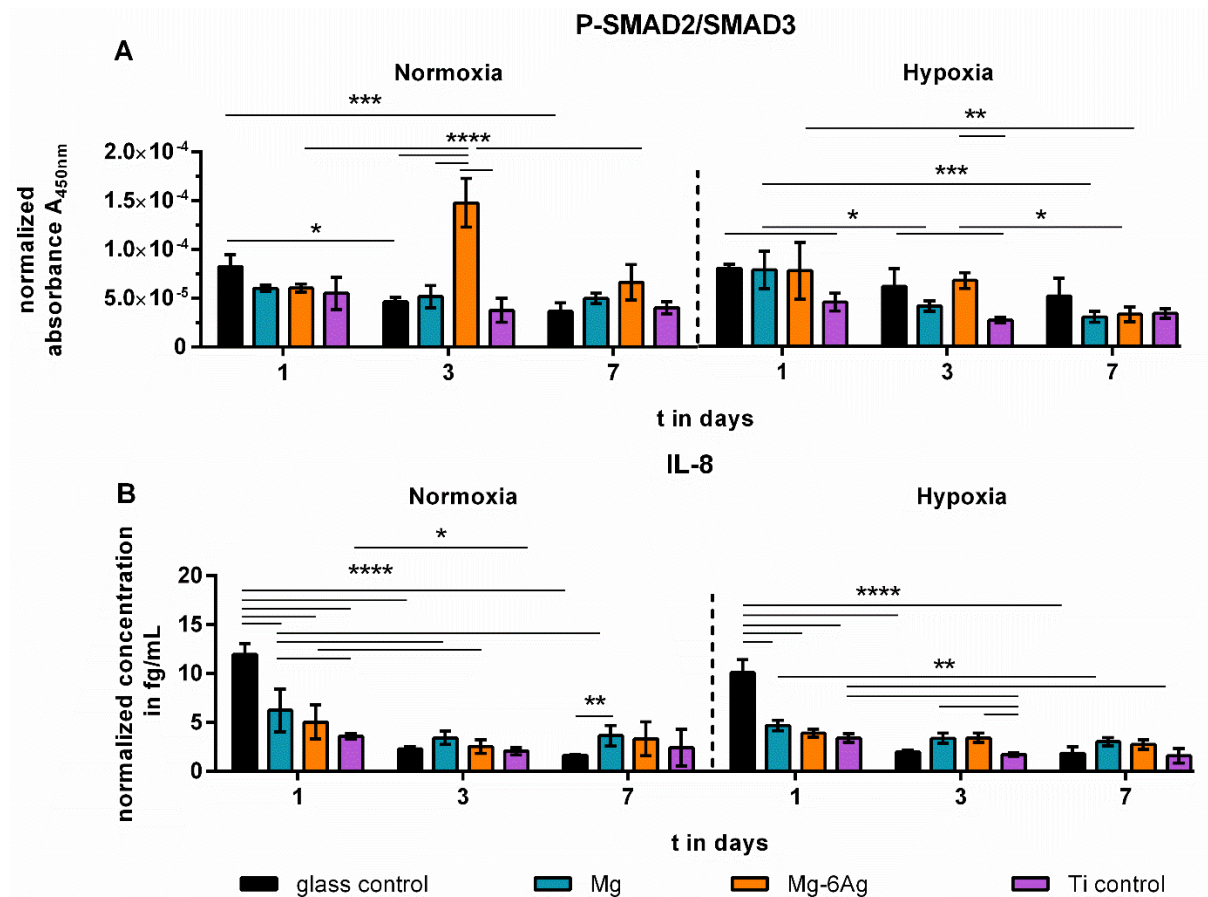


Figure 25. Measurement of IL-8 and phosphorylated SMAD2/SMAD3 complex concentrations. (A) Quantification of phosphorylated SMAD2/SMAD3 complex in the coculture lysate normalized to the cell number. (B) Determination of IL-8 concentrations in the coculture supernatant normalized to the cell number. Resulting protein concentrations are presented as the mean \pm SD from duplicates of two independent experiments with three samples. Statistically significant differences between protein concentrations (material, time points) were obtained via a two-way ANOVA with a Tukey's multiple comparison test ((A) $n=4$; (B) $n=12$); * = $p < 0.05$; ** = $p < 0.01$; *** = $p < 0.001$; **** = $p < 0.0001$.

4.3.3 Studying the influence of surface-near effects of Mg degradation on cell proliferation

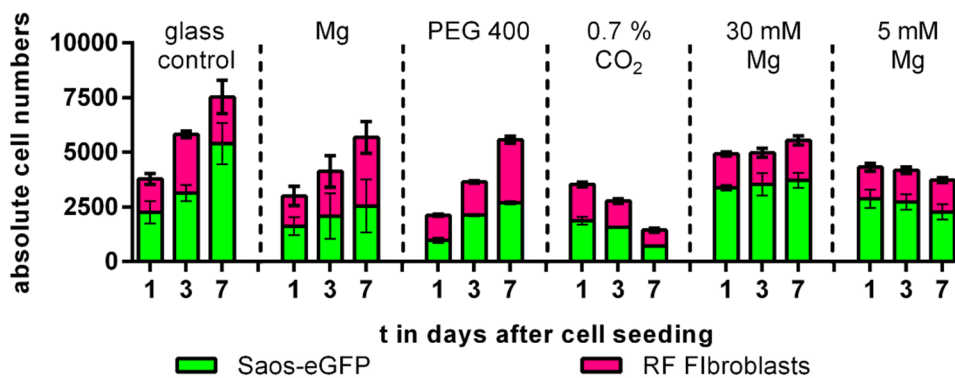
Table 10 shows the pH, osmolality and Mg concentrations of the single parameter solutions in comparison to the values for the glass control and the supernatant of during direct Mg disc seeding.

PEG 400 and the decrease in surrounding CO_2 conditions were used to increase the osmolality and pH, respectively, as it happens during Mg degradation. In this way, both surface-near effects were individually simulated without changing other Mg degradation-dependent parameters. The adjusted osmolality and pH values were higher than the measured values during Mg degradation. This was done because it is known that degradation-dependent effects directly at the interface between material and cells can be even stronger. Likewise, an increased Mg concentration was simulated with two different extracts. The 5 mM Mg extract was used to simulate increased Mg concentration as it was observed during the direct cell assay on Mg discs. The 30 mM Mg extract was used to approximate a higher Mg concentration directly at the material-cell interface.

These single parameter solutions were incubated only with the coculture under normoxia. Subsequently, cell number progression was monitored (Figure 26) and Ki-67 was visualized at day 7 (Figure 27).

Table 10. Concentration of Mg, osmolality and pH of single parameter solutions in comparison to the glass control (cell culture medium), and degrading Mg discs.

Condition	pH	Osmolality (mOsmol/Kg)	Mg concentration (mM)
glass control	7.8	335	0.8
Mg	7.9	357	4.8
PEG 400	7.8	412	0.8
0.7 % CO ₂	8.5	335	0.8
30 mM Mg extract	7.7	359	30.0
5 mM Mg extract	7.7	356	5.0



	glass control			Mg			PEG 400			0.7 % CO ₂			30 mM Mg			5 mM Mg		
	1	3	7	1	3	7	1	3	7	1	3	7	1	3	7	1	3	7
glass control	1	x	*															
	3		x	*						*								
	7			x		*		*		*		*		*				*
Mg	1			x	#							*		*		*		
	3				x	#						*		*				
	7					x					*	#		*	#			#
PEG 400	1						x		*#									
	3							x					*					
	7								x			*	#					#
0.7 % CO ₂	1									x			*					
	3										x		*		*			
	7											x		*				*
30 mM Mg	1												x					
	3													x				
	7														x			*
5 mM Mg	1															x		
	3																x	
	7																	x

Figure 26. Single parameters of Mg degradation influencing cell viability. Progression of cancer cell (green) and healthy cell (magenta) numbers in the coculture at day 1, 3 and 7. Absolute cell numbers

Results

are presented as the mean \pm SD from three samples from two independent experiments. Statistically significant differences between cell numbers of Saos-eGFP (*) or RF Fibroblasts (#) were obtained via a two-way ANOVA with Tukey's multiple comparison test (n=6): one symbol = $p < 0.05$.

The single parameter solutions simulated an increased pH (0.7 % CO₂), osmolality (PEG 400) and Mg²⁺ concentration (30 and 5 mM Mg extract) and were compared with the Mg samples directly seeded with cells (Mg), as well as with the non-degrading glass control (cells on glass slides). Generally, the increase in pH, osmolality and Mg²⁺ concentration resulted in a significantly lower cancer cell number compared to the control after seven days, whereas the healthy cell number did not change significantly. Furthermore, increasing the osmolality was the only parameter that did not induce significantly different cell numbers compared to the coculture directly seeded on Mg samples. Elevating the pH to 8.5 by decreased CO₂ culture conditions resulted in both, significantly lowered cancer and healthy cells after seven days. In opposite to this, increasing the Mg²⁺ concentration alone led to significantly increased cancer cell numbers, while healthy cell numbers were significantly lowered within seven days, compared to cell numbers on degrading Mg.

The influence of the individual Mg degradation-dependent surface-near effects on the Ki-67 expression is shown in Figure 27.

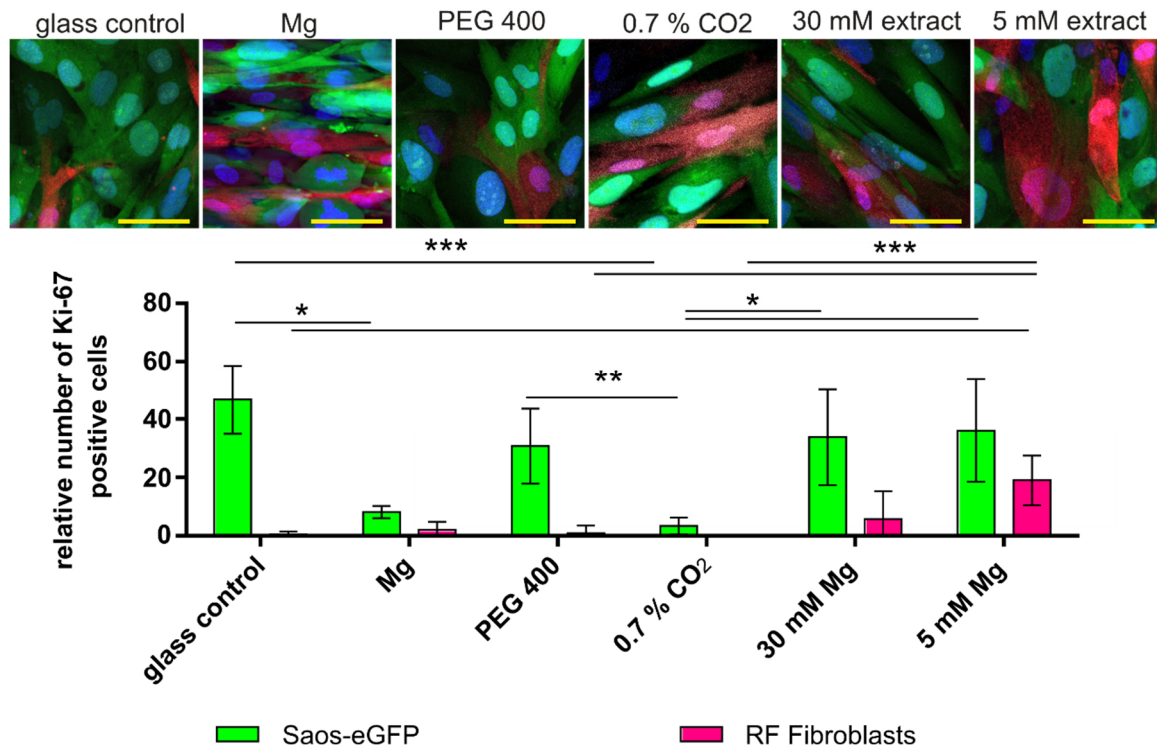


Figure 27. Influence of single parameters of Mg degradation on cell proliferation. Visualization of cell nuclei (blue) and Ki-67 expression (white) in Saos-eGFP (green) and RF Fibroblasts (magenta) after seven days of seeding. Scale bar is 50 μ m. Relative Ki-67 positive cell numbers are presented as the mean \pm SD from two samples, each with three randomly chosen positions. Statistically significant differences between Ki-67 positive cells were obtained via a Kruskal-Wallis H test with Dunn's multiple comparison test (n=6); * = $p < 0.05$; ** = $p < 0.01$; *** $p < 0.001$.

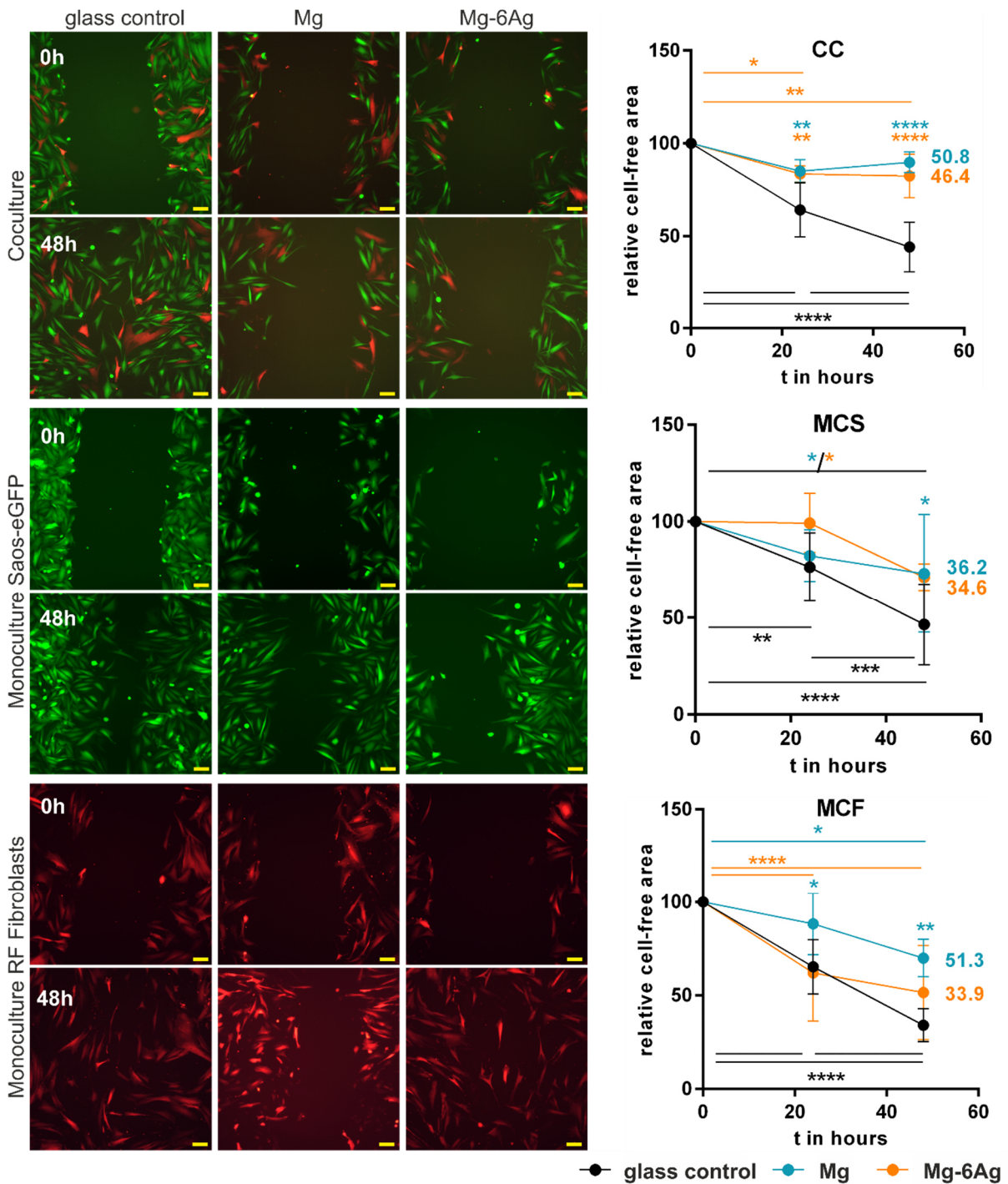
Increasing the pH of the coculture surrounding medium resulted in a similar cancer cell inhibition as observed for the coculture directly seeded on Mg samples. Consequently, the glass control, and rising of the osmolality or Mg concentration alone caused a significantly higher relative number of Ki-67 positive cancer cells compared to the sample with the increased pH. Additionally, the elevation of Mg concentrations appeared to increase the

relative number of Ki-67 positive healthy cells as well. However, a higher Mg concentration (30 mM) seemed to reduce the proliferation promoting effects for healthy cells compared to the 5 mM extract.

4.4 Influence of Mg-based materials on cancer cell migration and metastases

4.4.1 Determination of cell migration and invasion

Figure 28 shows the migration of cancer and healthy cells in response to Mg-based materials.



Results

Figure 28. Cell migration in response to Mg-based materials. The closure of the cell-free area of the coculture (CC) and the monocultures of Saos-eGFP (MCS) and RF Fibroblasts (MCF) was monitored up to 48 h. Blue and orange numbers indicate the migration inhibition in % referring to the glass control with uninhibited migration (100 %). Scale bar is 100 μm . Relative cell-free areas are presented as the mean \pm SD calculated from microscopic images from two independent experiments, two samples each with three different positions. Statistically significant differences between time points and different materials were obtained via a two-way ANOVA with Tukey's multiple comparison test ($n=12$); * = $p < 0.05$; ** = $p < 0.01$; *** $p < 0.001$; **** = $p < 0.0001$.

For the coculture, the glass control and samples with Mg-6Ag showed a significant reduction of the cell-free area within 48 h. After 24 and 48 h, the relative cell-free area of the glass control was significantly smaller compared to that of samples with Mg and Mg-6Ag. The migration inhibition of both degradable materials is about 50.8 % (Mg) and 46.4 % (Mg-6Ag) compared to the glass control at the end of the observation time.

Similarly, the wound area of all samples was significantly reduced after 48 h compared to the initial state for the monocultures. Furthermore, samples with Mg showed a significant migration inhibition compared to the glass control for both monocultures (MCS: 36.2 %, MCF: 51.3 %), while the presence of Mg-6Ag appeared to reduce migration by around 34 % for both monocultures.

In addition to the cell migration, the cell invasion in response to Mg-based materials was investigated. As shown in Figure 29, the maximal fluorescence intensity (representing the point of maximal cell accumulation) of the coculture cells incubated with Mg was significantly further away from the membrane compared to the glass control (Mg: 30 μm distance from the membrane; glass control: 0 μm distance from the membrane). This was confirmed by the results shown in Figure 30, where the numbers of invaded coculture cells in the glass control was significantly higher compared to that with Mg or Mg-6Ag. In contrast to this, the presence of Mg seemed to stimulate the invasion of the monocultures, which was found to be only significant for the cancer cells (Figure 29B). However, the number of monoculture cells that crossed the insert membrane did not differ significantly (Figure 30B).

In summary, Mg-based materials significantly inhibited the migration and invasion of the cancer cells in the coculture. Though, these observations were diminished (migration) or reversed (invasion) in the monoculture.

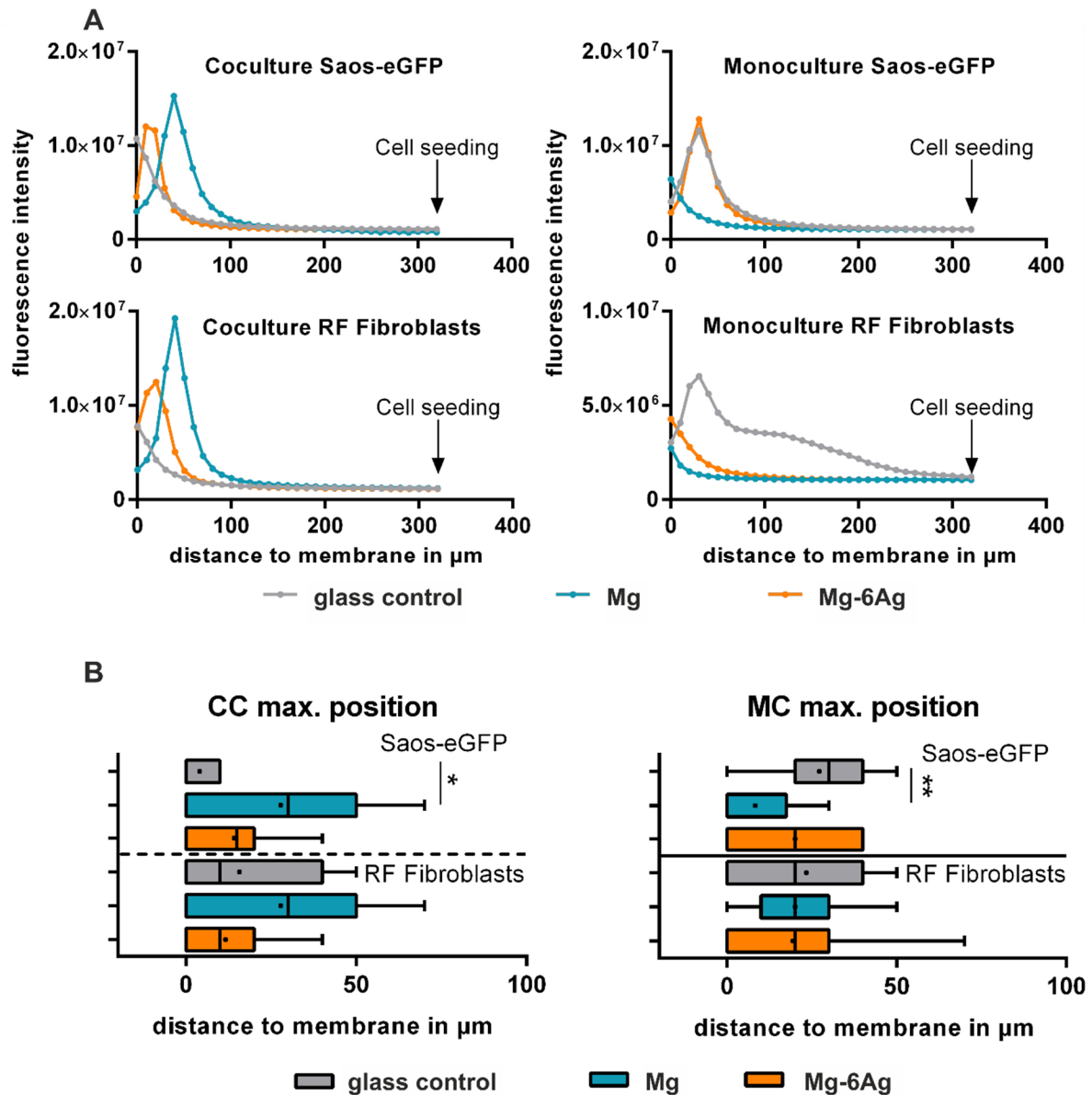


Figure 29. Cell invasion through an ECM gel matrix in response to Mg-based materials. Saos-eGFP and RF Fibroblasts were seeded as a coculture (CC) or monocultures (MC) in low-serum medium onto an ECM mimetic gel matrix in the upper compartment of a transwell insert. Mg, Mg-6Ag or a glass slides (glass control) were placed in the lower compartment in normal cell culture medium. After 72 h, z-stacks of the upside-down placed insert were taken with a cLSM. (A) Fluorescence intensities of representative pictures were plotted dependent on the position in the gel starting from the membrane (0 μm) to the gel surface (320 μm). (B) The positions with the maximal fluorescence intensity are presented as the mean \pm SD from three individual experiments with two samples and two randomly chosen positions. Statistically significant differences between Mg, Mg-6Ag and the glass control were obtained via an ordinary one-way ANOVA with Dunnett's multiple comparison test ($n=12$); * = $p < 0.05$; ** = $p < 0.01$.

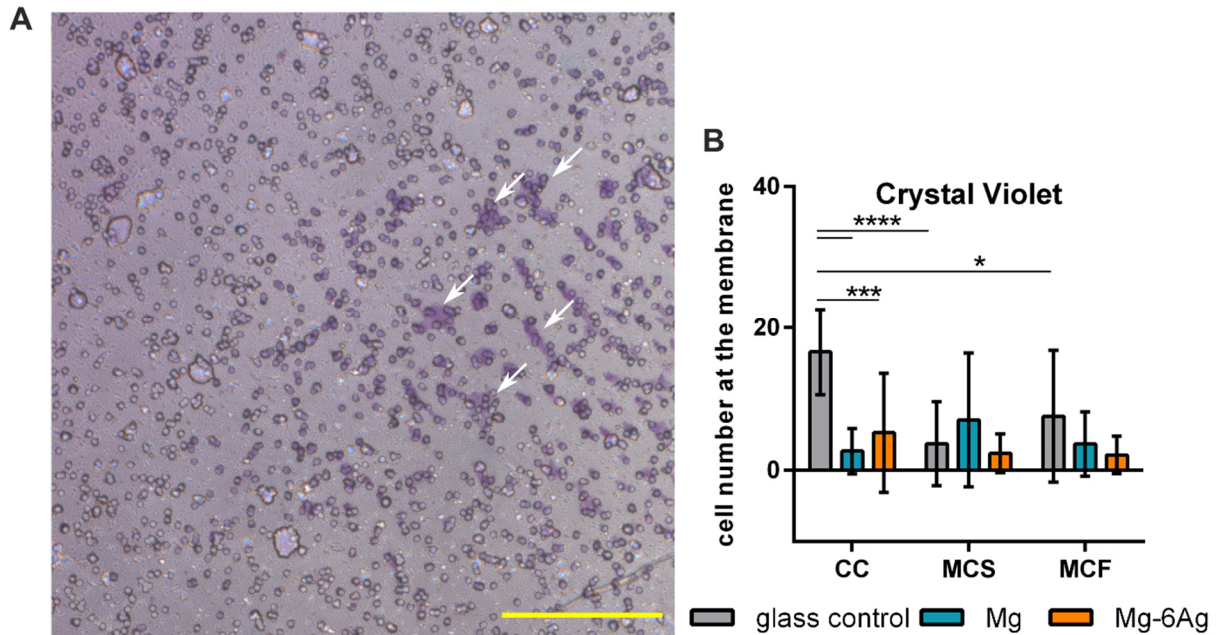


Figure 30. Quantification of invaded cells in response to Mg-based materials after 72 h. Cells were seeded onto an ECM mimetic gel matrix as described in chapter 3.6.1. (A) Representative image of the coculture in the glass control. White arrows indicate invaded cells on the membrane outside exemplarily. Scale bar is 100 μ m. (B) Cell counts of Saos-eGFP and RF Fibroblasts were seeded as a coculture (CC) or monocultures (MC). The cell numbers are presented as the mean \pm SD from three individual experiments with two samples and five randomly chosen positions. Statistically significant differences between Mg, Mg-6Ag and the neg. control with different cell type combinations were obtained via a two-way ANOVA with Tukey's multiple comparison test ($n=30$); * = $p < 0.05$; ** = $p < 0.01$.

4.4.2 Quantification of metastases-associated cytokines

To elucidate possible explanations for the different influence of degrading and non-degrading material on the migration and invasion of the coculture, the metastases-associated proteins MMP-2, MMP-9 and their inhibitor TIMP-1 were quantified in the supernatant and normalized to the cell numbers (Figure 31). The MMP-2 release peaked after seven days with a significant higher normalized MMP-2 release of the coculture cells direct seeded on Mg and Mg-6Ag compared to non-degrading material (glass control, Ti control). This was observed irrespective of the oxygen level. Normalized MMP-9 excretion from the cells steadily declined within the observation time of seven days under normoxia and hypoxia. Like MMP-2, the normalized MMP-9 secretion was significantly higher under the impact of Mg and Mg-6Ag compared to the glass control. Though, the MMP-9 concentration in the supernatant of coculture cells on the Ti control under normoxia was comparable to that on degrading material. Nevertheless, MMP-9 concentration was found to be far lower than MMP-2 concentration. TIMP-1 concentration reached a peak after three days when the coculture was seeded on Mg. This was shown to be significantly higher compared to the non-degrading materials but also to Mg-6Ag under normoxia and hypoxia.

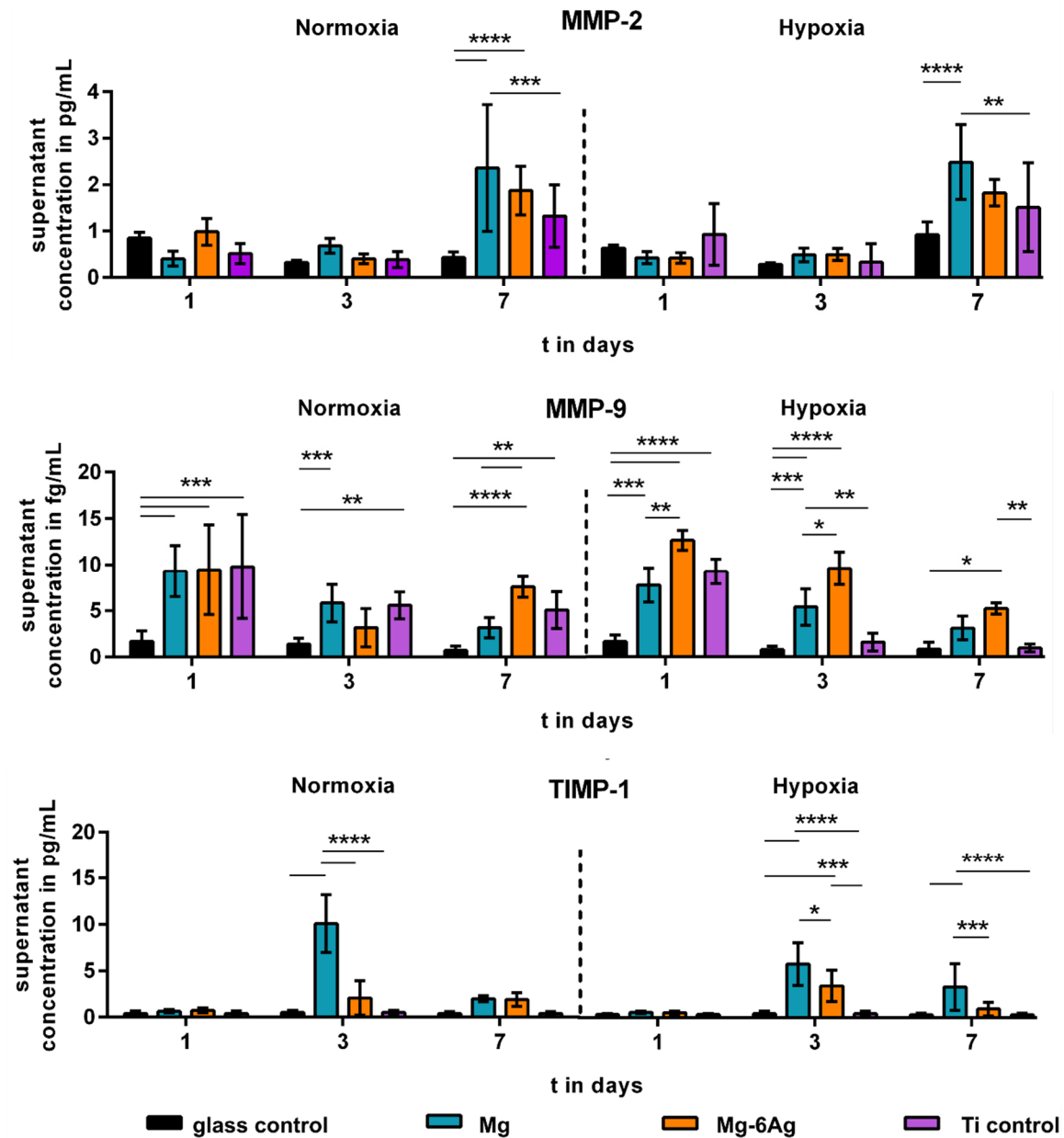
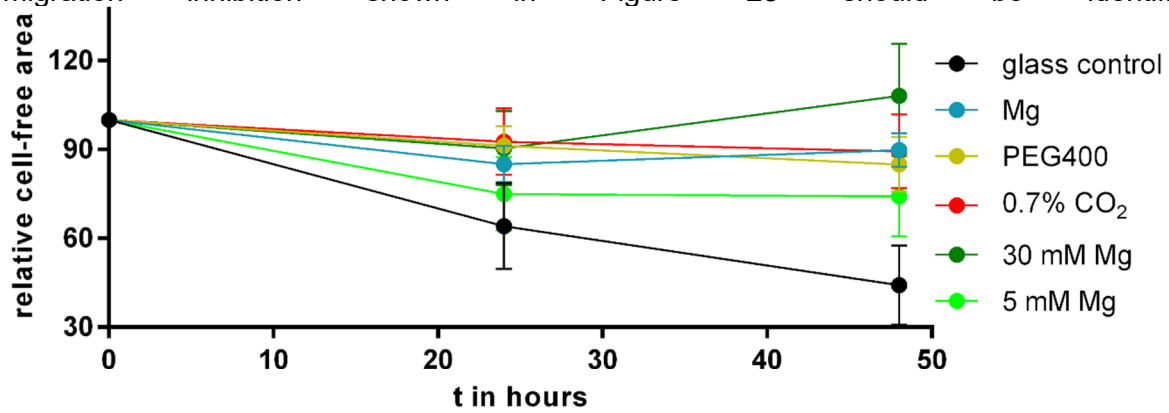


Figure 31. Quantification of metastases-associated cytokines in the supernatant. Saos-eGFP and RF Fibroblasts were seeded in a 1:1 coculture ratio on Mg, Mg-6Ag, a Ti control and a glass control. After one, three and seven days, supernatants were harvested and MMP-2, MMP-9 and TIMP-1 concentration was measured by ELISA and normalized to the cell numbers. Normalized cytokine concentrations are presented as the mean \pm SD from two individual experiments with three samples in duplicates. Statistically significant differences between time points and different materials were obtained via a two-way ANOVA with Tukey's multiple comparison test ($n=12$); * = $p < 0.05$; ** = $p < 0.01$; *** $p < 0.001$; **** = $p < 0.0001$.

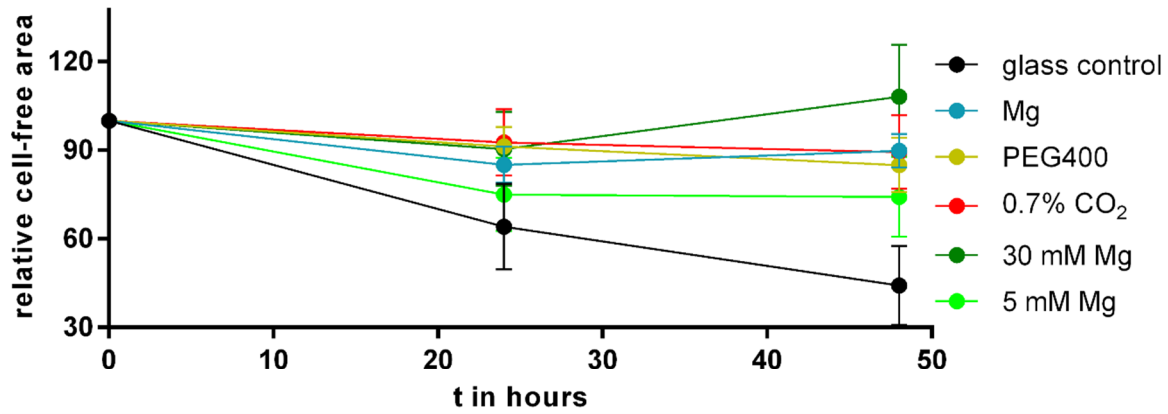
4.4.3 Studying the influence of single parameters of Mg degradation on cell migration

In a next step, the main driving factor of the Mg degradation that is responsible for the cell migration inhibition shown in Figure 28 should be identified.



	glass control			Mg			PEG 400			0.7 % CO ₂			30 mM Mg			5 mM Mg		
	0	24	48	0	24	48	0	24	48	0	24	48	0	24	48	0	24	48
glass control	0	x	*	*														
	24		x	*				*			*			*				
	48			x			*		*		*		*		*			*
Mg	0				x													
	24					x												
	48						x											
PEG 400	0						x		*									
	24							x										*
	48								x						*			
0.7 % CO ₂	0									x								
	24										x							*
	48											x			*			*
30 mM Mg	0												x					
	24													x	*		*	
	48														x		*	*
5 mM Mg	0															x	*	*
	24																x	
	48																	x

Figure 32 presents the wound healing progression under the influence of the defined and selected parameter solutions (see chapter 3.5.2).



		glass control			Mg			PEG 400			0.7 % CO ₂			30 mM Mg			5 mM Mg		
		0	24	48	0	24	48	0	24	48	0	24	48	0	24	48	0	24	48
glass control	0	x	*	*															
	24		x	*					*			*			*				
	48			x			*		*			*			*				*
Mg	0				x														
	24					x													
	48						x												
PEG 400	0							x		*									
	24								x										*
	48									x						*			
0.7 % CO ₂	0										x								
	24											x							*
	48												x			*			*
30 mM Mg	0													x					
	24														x	*		*	
	48															x		*	*
5 mM Mg	0																x	*	*
	24																	x	
	48																		x

Figure 32. Cell migration in response to single parameters of Mg degradation. After producing a cell-free area the medium was changed to the single parameter solutions described in chapter 3.5.2. The closure of the cell-free area of the coculture was monitored up to 48 h. Relative cell-free areas are presented as the mean \pm SD calculated from microscopic images from two independent experiments, three samples each with three different positions. Statistically significant differences between time points and different single parameters were obtained via a two-way ANOVA with Tukey's multiple comparison test ($n=12$ or 18); * = $p < 0.05$.

Compared to the glass control (normal cell culture medium), the wound healing progression under the impact of Mg discs and the individual Mg degradation dependent surface-near effects was significantly slowed inhibited after 48 h. Contrary to this, the influence of Mg discs on the cell-free area did not significantly change compared to its individual Mg degradation-dependent surface-near effects. Increasing the pH and osmolality resulted in a comparable cell migration as for the coculture with Mg discs. Therefore, the pH and osmolality increase can be seen as driving forces for the inhibited cell migration during Mg degradation.

4.5 Influence of Mg-based materials on cancer cell immune evasion

4.5.1 Natural killer cells affecting the coculture cell ratio

Figure 33 shows the influence of the natural killer cell line NK-92 on the relative cell numbers of the coculture in a 5:1 (NK:coculture) ratio of the initially seeded cell numbers on Mg and Mg-6Ag under hypoxia and normoxia. There were no significant differences between cell numbers of the cocultures without NK-92 (control) and these that were incubated with NK-92 for 4 h. Relative fibroblast cell numbers on Mg appeared to increase between three and seven days. On Mg-6Ag, the relative cell numbers of the healthy and cancer cells remain majorly constant over the observation time of seven days, while the glass surface strongly supported the growth of the cancer cells.

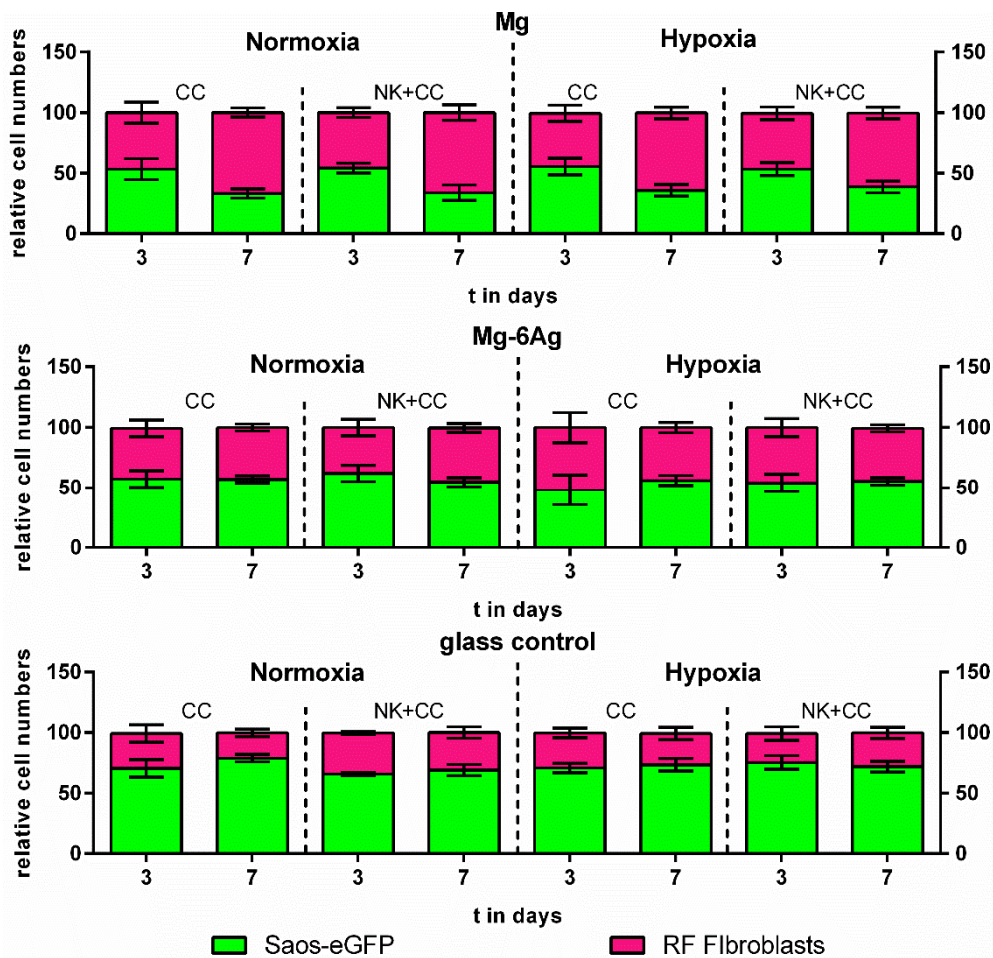


Figure 33. Influence of natural killer cells on coculture cell numbers on Mg-based materials. Saos-eGFP and RF Fibroblasts were incubated with NK (NK+CC) in a ratio 5:1 (NK:coculture) or just as a coculture without NK cells (CC). Relative cell numbers are presented as the mean \pm SD calculated from microscopic images from two independent experiments with three samples per time point. Statistically significant differences between cell numbers were obtained via a two-way ANOVA with Tukey's multiple comparison test (n=9)

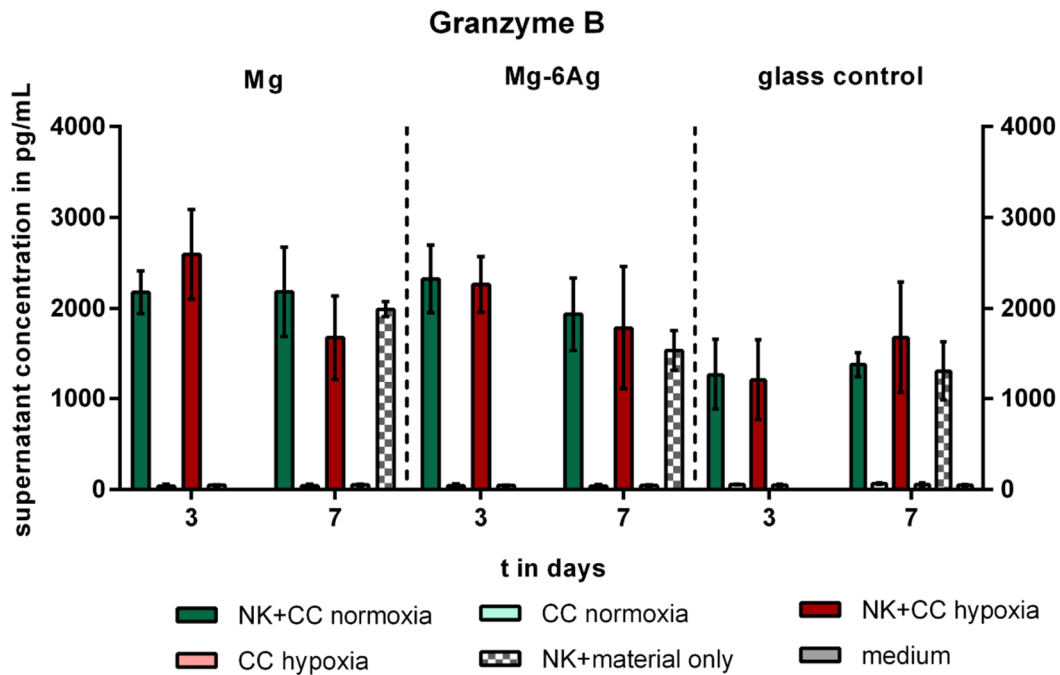
4.5.2 Quantification of natural killer cell activation

The previous results in chapter 4.5.1 did not suggest a stimulating influence of the Mg degradation on the ability of NK cells to eliminate cancer cells. However, the NK cell activity may be influenced by the degrading Mg-based materials. The activity of NK-92 was determined by quantification of supernatant concentrations of the proteins granzyme B (Figure 34) and perforin (Figure 35) that are expressed by NK cells upon activation.

Granzyme B appeared to be expressed by the NK cells independently from the material or coculture presence. However, the addition of NK-92 to the coculture on Mg and Mg-6Ag under normoxia resulted in significantly higher supernatant granzyme B concentrations compared to the glass control.

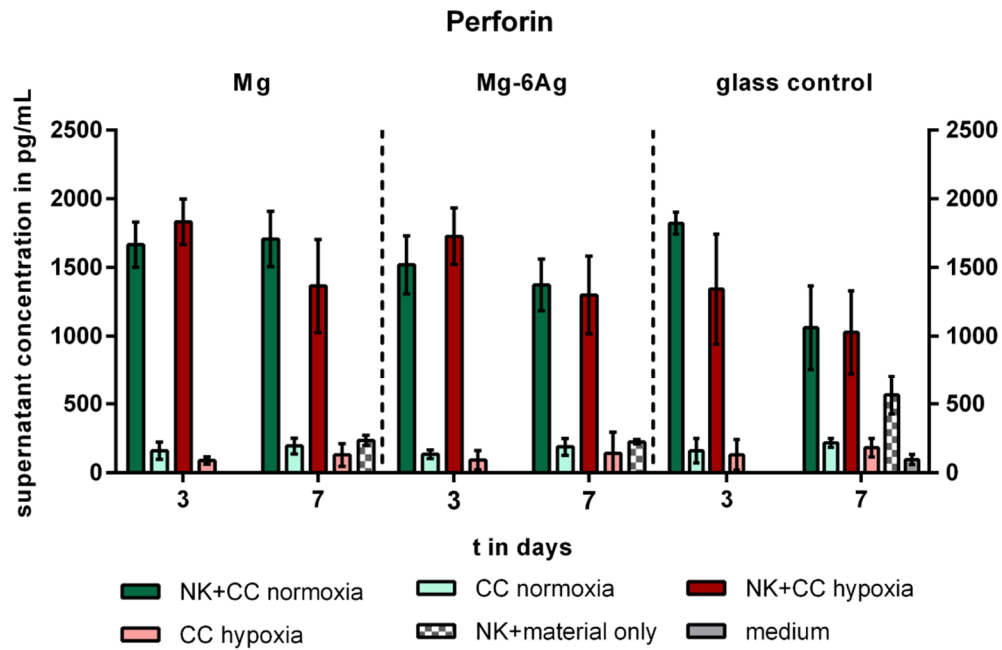
Figure 35 shows the perforin expression by NK cells into the supernatant. Contrary to granzyme B, NK cells expressed significantly more perforin, when they interacted with the osteosarcoma-fibroblast coculture compared to only with material (NK+material only). Additionally, the differences in perforin levels of the coculture on Mg-based materials and the glass control were not significantly at day 3, but perforin supernatant concentrations were significantly higher with Mg and Mg-6Ag compared to the glass control at day 7.

Results



		day 3		day 7		Mg					Mg-6Ag					glass control					medium
		NK+CC normoxia	CC normoxia	NK+CC hypoxia	CC hypoxia	NK+material only	NK+CC normoxia	CC normoxia	NK+CC hypoxia	CC hypoxia	NK+material only	NK+CC normoxia	CC normoxia	NK+CC hypoxia	CC hypoxia	NK+material only					
Mg	NK+CC normoxia		*	*							*					*			*	*	
	CC normoxia	*			*														*	*	
	NK+CC hypoxia			*	*														*	*	
	CC hypoxia			*	*														*	*	
	NK+material only		*	*	*	*													*	*	
Mg-6Ag	NK+CC normoxia						*	*			*					*			*	*	
	CC normoxia						*	*		*									*	*	
	NK+CC hypoxia							*	*	*									*	*	
	CC hypoxia							*	*	*	*								*	*	
	NK+material only						*	*	*	*	*								*	*	
glass control	NK+CC normoxia	*					*				*	*				*	*		*	*	
	CC normoxia										*	*							*	*	
	NK+CC hypoxia			*					*				*	*				*	*	*	
	CC hypoxia												*	*	*			*	*	*	
	NK+material only	*	*	*	*	*	*	*	*	*	*	*	*	*	*	*	*	*	*	*	
medium	*	*	*	*	*	*	*	*	*	*	*	*	*	*	*	*	*	*	*		

Figure 34 Supernatant granzyme B concentration during incubation of the coculture with natural killer cells. NK-92 were added to the coculture in a 5:1 (NK:coculture) ratio for 4 h. Then, the supernatants of cocultures (CC) on different materials with NK (NK+CC) and without NK (CC) under normoxia and hypoxia and NK with material only (NK+material control) were collected. Granzyme B concentrations are presented as the mean \pm SD from three samples of three experiments. Statistically significant differences between treatment and oxygen levels were obtained via a two-way ANOVA with Tukey's multiple comparison test (n=9): one symbol = $p < 0.05$.



		day 3		day 7		Mg					Mg-6Ag					glass control					medium
		NK+CC normoxia	CC normoxia	NK+CC hypoxia	CC hypoxia	NK+material only	NK+CC normoxia	CC normoxia	NK+CC hypoxia	CC hypoxia	NK+material only	NK+CC normoxia	CC normoxia	NK+CC hypoxia	CC hypoxia	NK+material only					
Mg	NK+CC normoxia	*	*	*	*	*					*				*			*	*		
	CC normoxia	*	*															*	*		
	NK+CC hypoxia			*	*	*												*	*		
	CC hypoxia			*	*														*	*	
	NK+material only	*		*		*															
Mg-6Ag	NK+CC normoxia						*	*		*								*	*		
	CC normoxia						*	*										*	*		
	NK+CC hypoxia							*	*	*								*	*		
	CC hypoxia							*	*	*								*	*		
	NK+material only						*	*	*	*								*	*		
glass control	NK+CC normoxia										*	*			*	*		*	*		
	CC normoxia										*	*			*	*		*	*		
	NK+CC hypoxia			*							*	*	*	*	*	*		*	*		
	CC hypoxia								*		*	*	*	*	*	*		*	*		
	NK+material only	*	*	*	*		*	*	*	*	*	*	*	*	*	*	*	*	*		
medium	*		*			*	*			*	*			*	*		*	*			

Figure 35 Supernatant perforin concentration during incubation of the coculture with natural killer cells. NK-92 were added to the coculture in a 5:1 (NK:coculture) ratio for 4 h. Then, the supernatants of cocultures (CC) on different materials with NK (NK+CC) and without NK (CC) under normoxia and hypoxia and NK with material only (NK+material control) were collected. Perforin concentrations are presented as the mean ± SD from three samples of three experiments. Statistically significant differences between treatment and oxygen levels were obtained via a two-way ANOVA with Tukey's multiple comparison test (n=9): one symbol = p < 0.05.

4.6 Influence of Mg-based materials on cancer cell induced angiogenesis

4.6.1 Conditioned media used for HUVEC incubation

Table 11 shows the Mg concentration in the supernatants of the different conditioned media (compare to chapter 3.8.1) to avoid false correlation to the Mg concentration of the further results in this section. The preparation of conditioned media under different oxygen levels did not lead to significant changes in supernatant Mg concentrations. As shown in chapter 4.1, the Mg concentration of the glass control and of the material control (cell culture medium) was similar (0.8 mM). The degradation of Mg and Mg-6Ag with direct seeding of Saos-eGFP and RF Fibroblasts resulted in Mg concentration between 3-6 mM released in the cell culture supernatant (similar to Figure 19)

Table 11. Supernatant Mg concentration (in mM) in conditioned media. Saos-eGFP and RF Fibroblasts were seeded as a 1:1 coculture (CC) or monocultures (Saos-eGFP: MCS, RF Fibroblasts: MCF) on Mg, Mg-6Ag or glass. Furthermore, material without cells served as a control (mat. control) (see chapter 3.8.1). Conditioned media were harvested after one, three and seven days, and Mg concentration was quantified by AAS (n=6)

Mg (mM)	conditioned medium CC		conditioned medium MCS		conditioned medium MCF		conditioned medium mat. control		
	Day	Normoxia	Hypoxia	Normoxia	Hypoxia	Normoxia	Hypoxia	Normoxia	Hypoxia
glass control	1	0.80±0.00	0.81±0.01	0.77±0.01	0.76±0.05	0.70±0.02	0.73±0.01	0.66±0.04	0.67±0.00
	3	0.88±0.10	0.78±0.01	0.88±0.17	0.86±0.06	0.75±0.00	0.75±0.01		
	7	0.79±0.00	0.80±0.02	0.85±0.08	0.74±0.01	0.77±0.01	0.71±0.00		
Mg	1	3.52±0.01	3.62±0.04	3.16±0.00	3.08±0.01	3.00±0.23	2.85±0.02	3.31±0.05	3.26±0.06
	3	3.93±0.18	3.78±0.01	3.74±0.15	3.93±0.07	3.72±0.31	4.02±0.07		
	7	4.84±0.20	4.76±0.24	4.42±0.04	5.85±0.06	4.33±0.04	6.36±0.03		
Mg-6Ag	1	3.64±0.02	3.55±0.11	2.83±0.02	3.93±0.01	2.48±0.01	2.46±0.05	3.12±0.03	3.62±0.08
	3	3.69±0.11	3.66±0.08	3.96±0.02	3.92±0.01	3.33±0.05	3.28±0.05		
	7	5.59±0.07	4.45±0.07	4.61±0.94	3.90±0.01	4.00±0.03	4.46±0.10		

4.6.2 Endothelial cell permeability and proliferation - VEGF expression

Cancer-induced angiogenesis is initiated by loosening of interendothelial connections. This permeabilization of the endothelial layer facilitates the extravasation of plasma proteins to propagate the angiogenesis. Figure 36 shows the permeability of the interendothelial cell junctions under the influence of the conditioned media represented by the concentration of fluorescein-dextran that passed through the HUVEC monolayer.

Under normoxia, HUVEC revealed a significantly higher amount of passed fluorescein-dextran, thus significantly higher permeability at day 7 compared to day 3. The fluorescein-dextran concentration in the lower chamber tended to be higher for HUVEC treated with conditioned medium from cells (coculture and monoculture) on glass (glass control) compared to that of HUVEC treated with conditioned medium from cells seeded on Mg-based materials at day 7. In contrast to this, the HUVEC permeability at day 3 and 7 appeared to be not different under hypoxia.

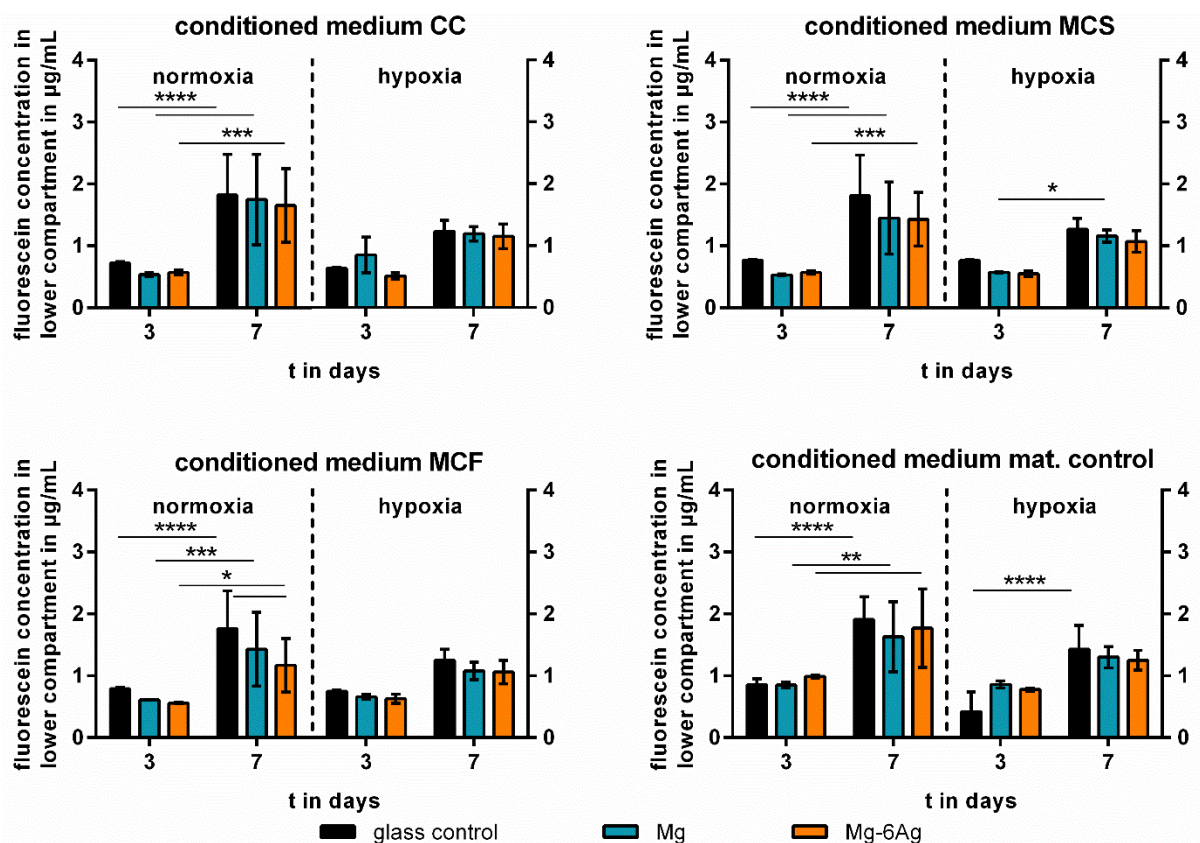


Figure 36. Permeability of endothelial cells incubated with conditioned medium. HUVEC were grown in 24-well insert to a confluent monolayer. Conditioned medium from the coculture (CC) or monocultures of Saos-eGFP (MCS) and RF Fibroblasts (MCF) on Mg-based materials or just the material without cells (mat. control) were incubated with HUVEC (see chapter 3.8.1). After three and seven days, fluorescein-dextran solution was added to the upper compartment. After 1 h shaking in an incubator the lower compartment was transferred to a 96-well plate in triplicates and fluorescence was measured at 535 nm and quantified using a standard curve. Fluorescein-dextran concentrations are presented as the mean \pm SD from two individual experiments with one triplicate each. Statistically significant differences between different time points and materials were obtained via a two-way ANOVA with Tukey's multiple comparison test (n=6); * = $p < 0.05$; ** = $p < 0.01$; *** $p < 0.001$; **** = $p < 0.0001$

Results

The proliferation of endothelial cells, which is part of the second step of angiogenesis, is presented in Figure 37 as relative fluorescence units of stained cell nuclei at day 0, 3 and 7. Generally, HUVEC incubated with the conditioned media of the coculture or monocultures on glass showed a tendency towards an increasing cell amount irrespective of the oxygen levels. Strikingly, HUVEC numbers showed an even more distinct increase within the observation time of seven days when incubated in the conditioned medium of the cancer cells on glass as a monoculture under normoxia. Similar findings were received for HUVEC treated with the coculture conditioned medium on glass under hypoxia. Incubating HUVEC with conditioned medium of cells (coculture and monoculture) on Mg resulted in a significant increase of the cell amount within the first three days and a subsequent decline under normoxia. Contrary to this, the conditioned media produced with Mg-6Ag only showed slight changes in HUVEC amounts.

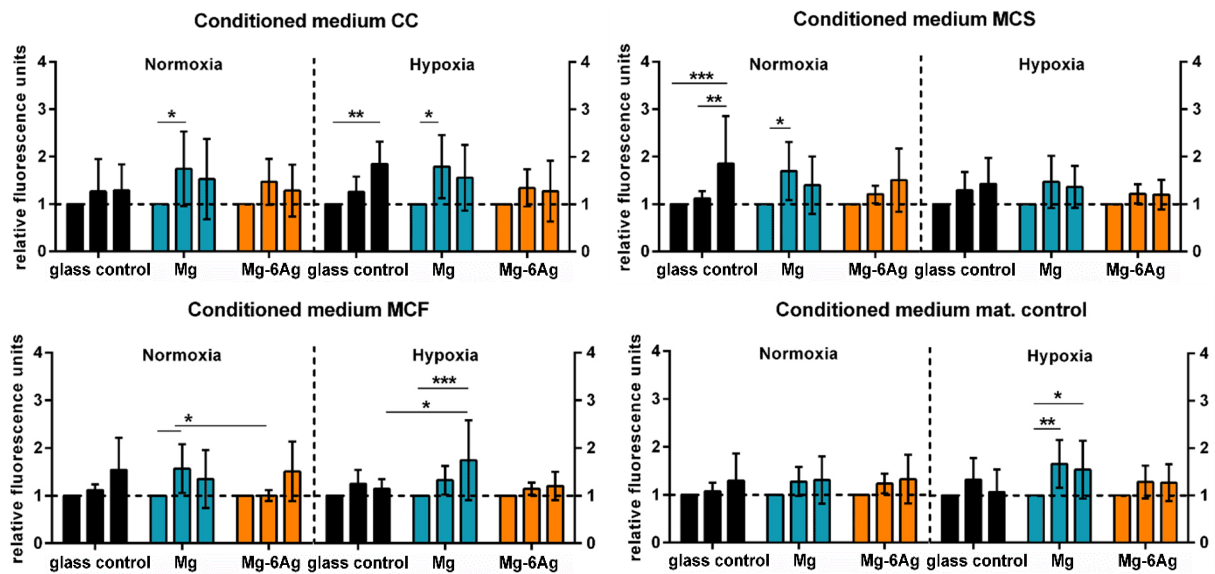


Figure 37. Proliferation of HUVEC incubated with conditioned medium. ECGM was changed to conditioned medium from the coculture (CC) or monocultures of Saos-eGFP (MCS) and RF Fibroblasts (MCF) on Mg-based materials or cell-free material (mat. control) (see chapter 3.8.1). Fluorescence intensities (day 3= second bar, day 7=third bar) relative to that of the initial (first bar) cell nuclei staining are presented as the mean \pm SD from two individual experiments with six samples each. Statistically significant differences between different time points and materials were obtained via a two-way ANOVA with Tukey's multiple comparison test ($n=12$); * = $p < 0.05$; ** = $p < 0.01$; *** $p < 0.001$.

VEGF is the most prominent factor of cancer-induced angiogenesis and contributes to endothelial cell growth and vascular permeability. Figure 38 summarizes the normalized VEGF concentrations in the supernatant of HUVEC incubated with conditioned media after one, three and seven days. No significant differences could be observed for the VEGF concentrations in the supernatant of conditioned media of the coculture, fibroblast monoculture or the material control. Only the incubation of HUVEC with conditioned medium of cancer cells as a monoculture on glass under hypoxia led to a significant increase in VEGF concentration at day 3.

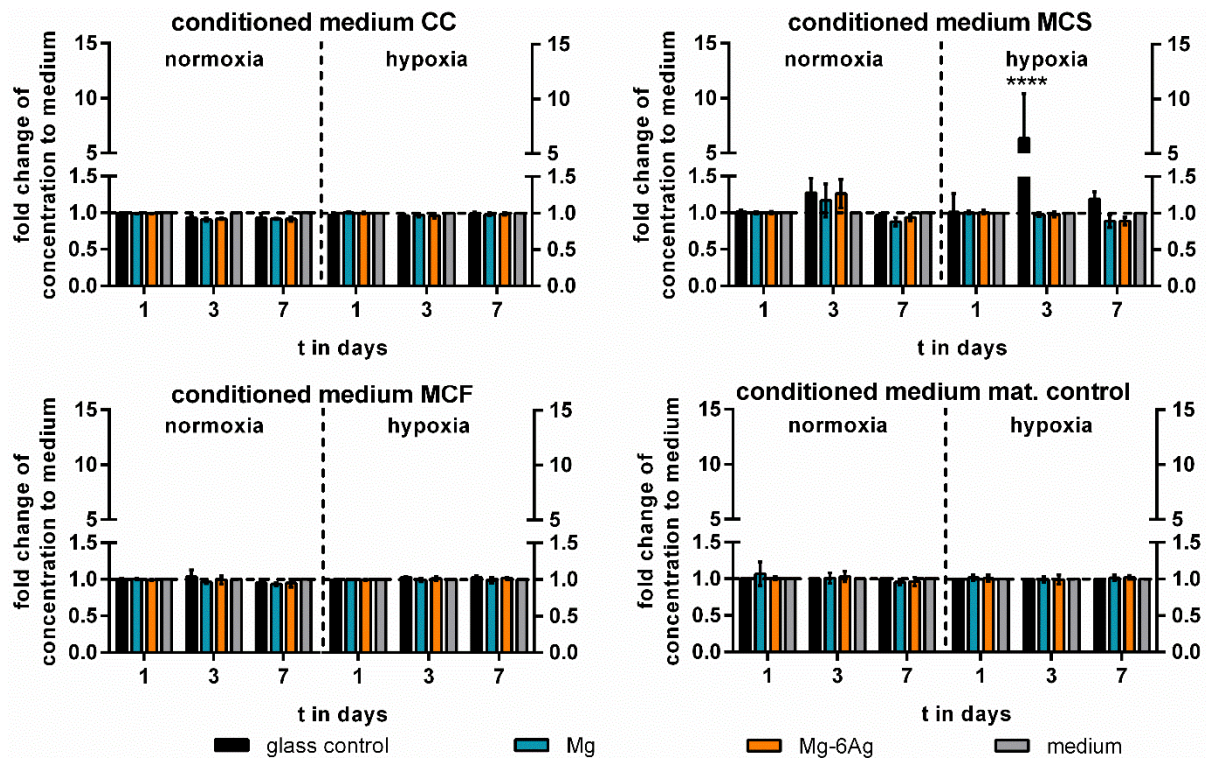


Figure 38. Quantification of VEGF in the supernatant of endothelial cells. HUVEC were treated with conditioned medium from the coculture (CC) or monocultures of Saos-eGFP (MCS) and RF Fibroblasts (MCF) on Mg-based materials or just the material without cells (mat. control) (see chapter 3.8.1). After one, three and seven days, the supernatant was harvested, and VEGF concentration quantified by ELISA. Fold changes of the VEGF concentration relative to the medium control are presented as the mean \pm SD from two individual experiments with three samples. Statistically significant differences between fold changes of samples and medium control were obtained via a one-way ANOVA with Dunnett's multiple comparison test ($n=6$); **** $p < 0.0001$

4.6.3 Endothelial cell migration

The migratory potential of endothelial cells is another characteristic of the second step of angiogenesis to prolong preexisting blood vessels. Figure 39 indicates the migration of HUVEC into a cell-free area dependent on different conditioned media (described in chapter 3.8.1) under normoxia (Figure 39A) and hypoxia (Figure 39B). Under normoxia, the wound closure was similar for HUVEC incubated with conditioned medium of the coculture and monocultures on all different substrates. For these conditions, the incubation with the conditioned media led to a significant wound closure within 48 h. However, there were no significant differences in the migration inhibition between the conditions. Incubating the HUVEC with only medium (on glass, no cells) also led to a significant reduction of the cell-free space.

Hypoxic conditions slowed down the migration of HUVEC irrespective of the substrate (glass control or Mg-based materials) when incubated with the coculture conditioned medium. In contrast to this, the incubation of the HUVEC with conditioned media obtained from the monocultures on Mg-based materials led to a significant reduction of migration compared to the respective samples on glass.

Only the conditioned media of Mg and Mg-6Ag without cells (mat. control) showed a significant HUVEC migration inhibition (40.4-61.9 %) compared to the glass control under both, normoxia and hypoxia.

Results

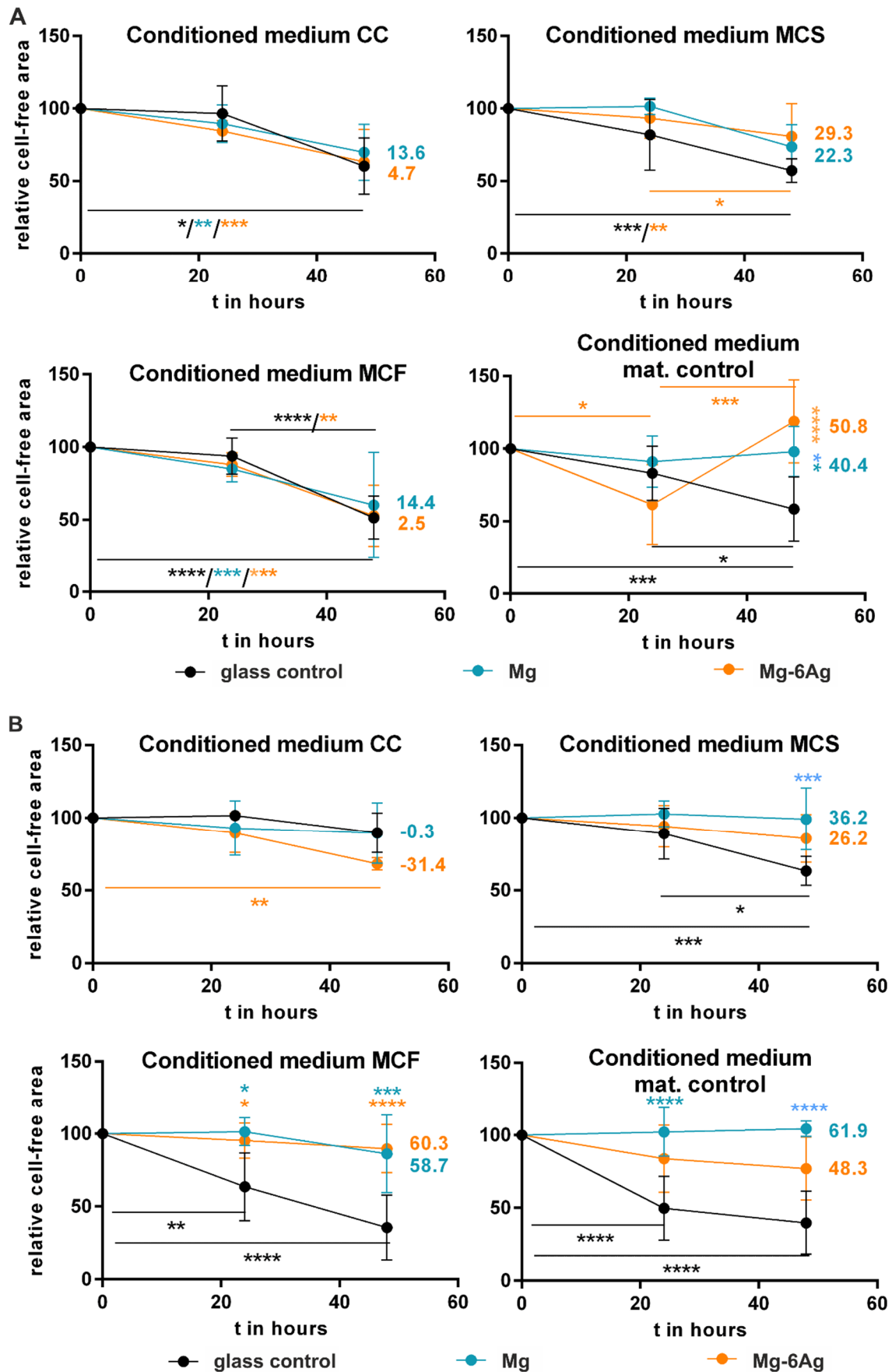


Figure 39. Migration of endothelial cells incubated with conditioned medium. Medium was changed to conditioned medium obtained from the coculture (CC) or monocultures of Saos-eGFP (MCS) and RF Fibroblasts (MCF) on Mg-based materials or just the material without cells (mat. control) (see chapter 61

3.8.1) under (A) normoxia and (B) hypoxia. Blue and orange numbers indicate the migration inhibition in % referring to the glass control with uninhibited migration (100 %). Resulting cell-free areas are presented as the mean \pm SD from two individual experiments, two samples each with three different positions. Statistically significant differences between different time points and to the neg. control were obtained via a two-way ANOVA with Tukey's multiple comparison test (n=12); * = $p < 0.05$; ** = $p < 0.01$; *** $p < 0.001$; **** = $p < 0.0001$

4.6.4 Formation of an endothelial cell network

Endothelial cell proliferation and migration lead to the formation of new blood vessel branches from preexisting ones. As a last step, the endothelial cells differentiate and form capillary structures on a basement membrane (Figure S1). Figure 40 shows the magnitude of tube formation into an endothelial network in response to the conditioned medium after 6 h. Branches represent the connection between an extremity and a junction, while isolated segments are not connected to other structures. The incubation with Mg and Mg-6Ag containing conditioned medium induced HUVEC to form tubes with increased branch numbers under normoxia. However, the conditioned medium obtained from the monoculture of Saos-eGFP on Mg caused the HUVEC tube formation with a lower branch number and a tendency for a high number of isolated segments. Contrary to this, hypoxia led to a tendency towards decreased branch numbers for the monocultures on Mg and Mg-6Ag. A higher number of isolated segments was observed for the endothelial cells cultured under the impact of media obtained from the coculture and cell-free material (mat. control).

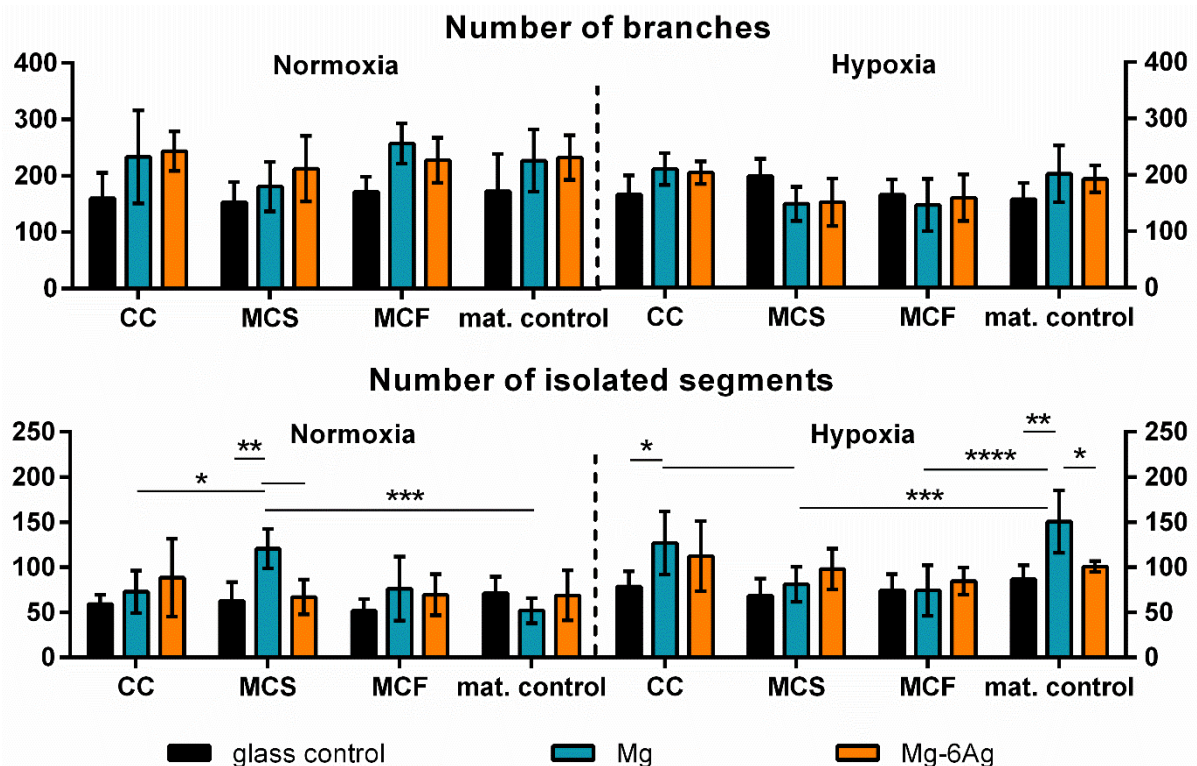


Figure 40. Endothelial cell tube formation in response to conditioned medium. A 96-well plate was coated with basement membrane matrix and seeded with HUVEC. Then, HUVEC cells were treated with conditioned medium from the coculture (CC) or monocultures of Saos-eGFP (MCS) and RF Fibroblasts (MCF) on Mg-based materials or just the material without cells (mat. control). After 6 h, the cells were stained with calcein-AM and images were taken with an inverse fluorescence microscope. The number of branches and isolated segments was quantified with the ImageJ plugin "Angiogenesis

Results

Analyzer” to assess angiogenesis. Both parameters are presented as the mean \pm SD from two individual experiments with samples in triplicates. Statistically significant differences between different materials or cell types were obtained via a two-way ANOVA with Tukey’s multiple comparison test ($n=6$); * = $p < 0.05$; ** = $p < 0.01$; *** $p < 0.001$; **** = $p < 0.0001$

4.7 Degradation tailoring of Mg-6Ag to adjust anticancer activity

Figure S2-S4 and Figure 40 show the degradation rates of all heat-treated, fast-degrading Mg-6Ag samples. Only a T6 aging treatment with 200 °C for 7-15 min succeeded to adjust the MDR of Mg-6Ag samples in the desired degradation range between 1-2.4 mm/a. Surface images and the detailed degradation rates for this material obtained after seven days are depicted in Figure 41. The respective delta pH and osmolality values after one, three and seven days of immersion are shown in Figure 42. With increasing heat-treatment duration from 7 to 15 min, the MDR increased steadily.

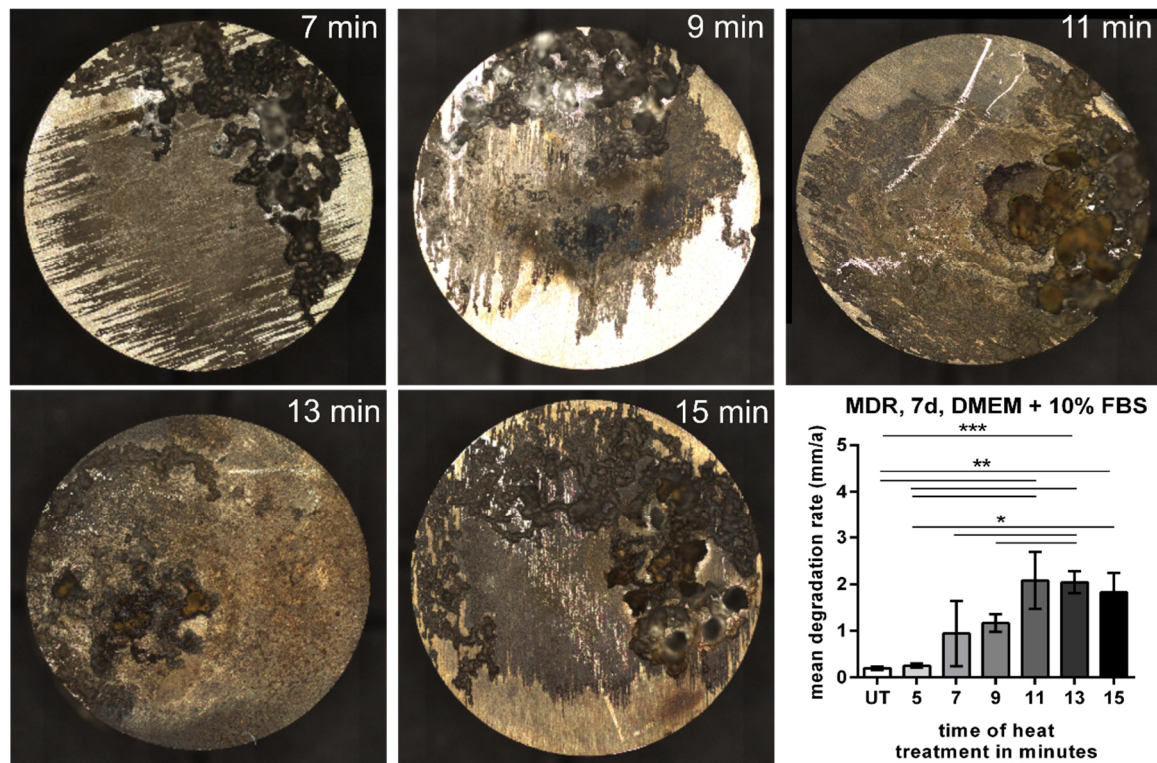


Figure 41. MDR of Mg-6Ag T6 heat treatment for 7-15 min at 200 °C. Surface images of T6 treated Mg-6Ag discs and determination of MDR after seven days in comparison to the untreated (UT) Mg-6Ag. The MDR is presented as the mean \pm SD from two individual experiments with six samples each. Statistically significant differences between the MDRs were obtained via a Kruskal-Wallis H test with Dunn’s multiple comparison test ($n=12$); * = $p < 0.05$; ** = $p < 0.01$; *** $p < 0.001$; **** = $p < 0.0001$.

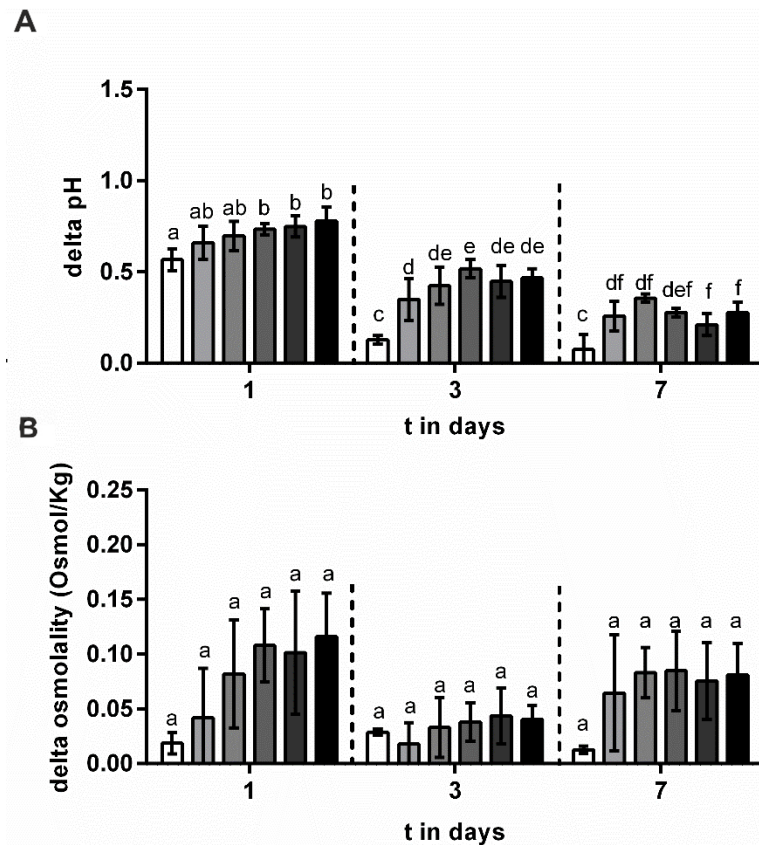


Figure 42. Differences of pH and osmolality values of T6 treated and untreated (UT) Mg-6Ag. Delta (A) pH and (B) osmolality values represent the difference between T6 treated samples and medium and were calculated as described in chapter 3.3. Both parameters are presented as the mean \pm SD from two individual experiments with six samples each. Bars with a different lowercase letters showed statistically significant differences obtained via a two-way ANOVA with Tukey's multiple comparison test ($n=12$). Same letter = $p < 0.05$.

Likewise, the differences of pH and osmolality to the medium control increased with increasing MDR. Figure 43 shows the absolute cell count and cell ratio of Saos-eGFP and RF Fibroblasts on the heat-treated Mg-6Ag samples within seven days of immersion. The overall cell count decreased with increasing MDR and heat treatment duration.

Additionally, the cell ratios on fast-degrading Mg-6Ag progressed in a similar manner as on the slow degrading material within the seven days of immersion. With increasing immersion time, the proportion of healthy fibroblasts within the coculture increased, partly with significant differences between cancer and healthy cell ratios.

Results

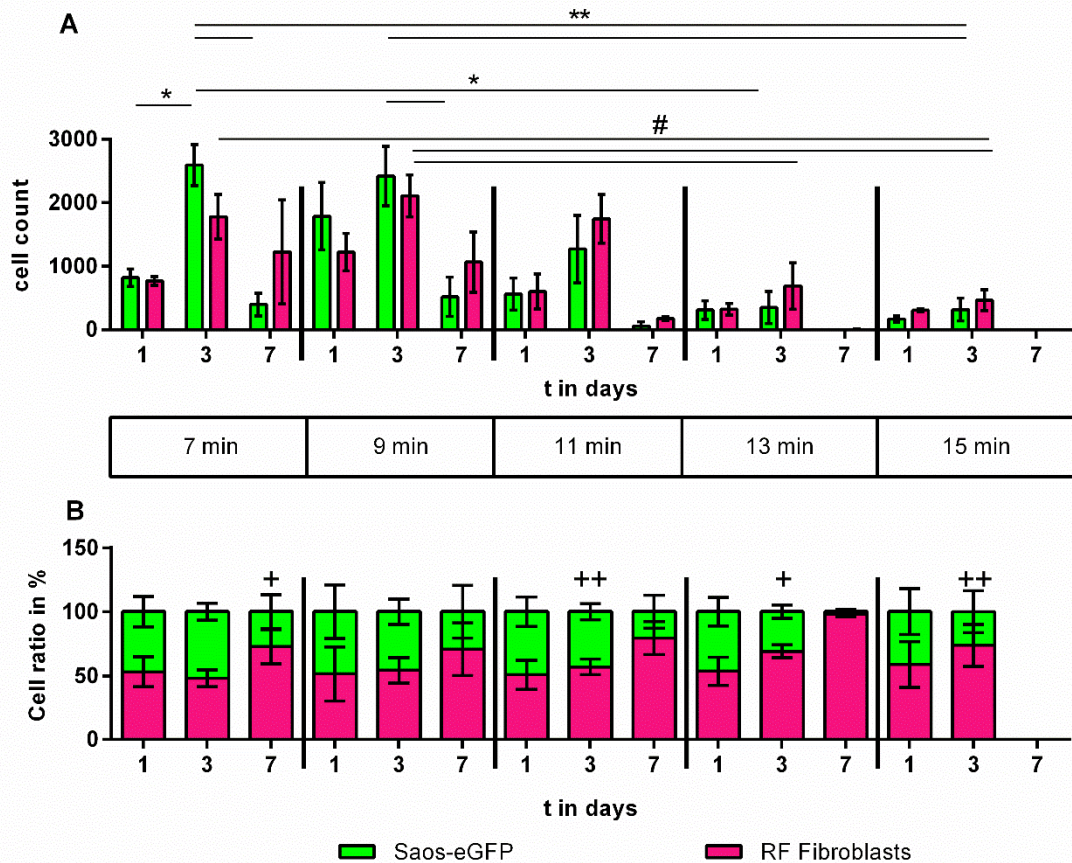


Figure 43. Cell viability of Mg-6Ag T6 heat-treated samples. (A) Determination of cell numbers and (B) corresponding cell ratios of osteosarcoma cells (green) and fibroblasts (magenta) on the differently T6 treated Mg-6Ag. Cell numbers and ratios are presented as the mean \pm SD from two experiments with three samples each. (A) Statistically significant differences between cell numbers of Saos-eGFP (*) or RF Fibroblasts (#) on different materials were obtained via a Kruskal-Wallis H test with Dunn's multiple comparison test (n=6). One symbol = $p < 0.05$; two symbols = $p < 0.01$. (B) Statistically significant differences between the ratios of both cell types on the same material were obtained via a Mann-Whitney test (n=6); + = $p < 0.05$, ++ = $p < 0.01$.

5 Discussion

5.1 Suitable model for testing anticancer activity of Mg-based materials

The first aim of this thesis was the development and characterization of a suitable *in vitro* cancer cell model to study the potential anticancer activity of Mg-based biomaterials. The execution of these studies requires a mechanistic model that simplifies conditions in the TME to ensure high throughput experiments but displays *in vivo* conditions better than cancer cell monocultures at the same time. In order to achieve this, a 1:1 coculture (initial cell ratio) of fluorescent human osteosarcoma cells (Saos-eGFP) and dermal fibroblasts (RF Fibroblasts) was employed, as recently published [171]. Such coculture models consisting of cancer cells and fibroblasts were already shown to increase the relevance of several cancer models before [172-176], while the application as a test system for Mg-based materials is not well established yet. Saos-2, which were used to create Saos-eGFP [160], were previously reported to be preferred over MG63 and U2OS [177,178] when studying the influence of Mg on bone-derived cells due to their similarity to human osteoblasts [179-182]. Adhesion and cell size of Saos-2 on tissue culture plastic were comparable to primary human osteoblasts under the influence of Mg salt extracts [178]. Furthermore, Czekanska [179,180] reported that Saos-2 also exhibited a comparable cytokine and growth factor profile, mineralization, and bone-associated alkaline phosphatase (ALP) activity to human osteoblasts. As described in chapter 1.4.2, fibroblasts play an important role in the TME, owing to their versatile interaction with the cancer cells. Furthermore, fibroblasts can be found in many other tissues that makes them an ideal cell type to investigate other cancer types as well. [183]. The osteosarcoma cells and fibroblasts used here both constitutively emit fluorescent light in green (eGFP) and red (FP602), respectively, that can be detected by conventional fluorescence microscopes. Generally, Mg-based materials limit the feasibility of standard molecular biological methods due to their size, opaqueness, and degradability. However, this fluorescent osteosarcoma-fibroblast coculture model allows the direct visualization as well as cell type distinction on the opaque Mg-based materials.

At first, the coculture were seeded on Mg-based materials to test the feasibility of the tumor model. Subsequently, the cell viability as well as the time-dependent cell number progression on the material were tested. Both cell types showed a viable, cell type-specific morphology on all used materials (Figure 17B), while the proportions of both cell types significantly varied between degrading and non-degrading materials. Mg and Mg-6Ag seemed to favor the growth of healthy fibroblasts, whereas on Ti-6Al-4V the cancer cell ratio significantly increased within the coculture. Since both cell types showed comparable proliferation rates in monoculture (Figure 17A), the observed effects can be assumed to be material specific. Moreover, cell progressions in coculture and monocultures strongly differed, that is why the coculture system is suggested to be preferred over simple monocultures in this context.

To avoid misinterpretations of material-cell effects, the influence of the cells on the MDR, pH, and osmolality were analyzed. It is a well-accepted fact that not only the material can affect cells, but an influence can also be vice versa. However, cells were differently reported as degradation stimulating [184-186], inhibiting [187,188], or without any effect [189], suggesting cell type and material dependency. All these studies were performed with monocultures, which reduces the comparability with the coculture model used in the present study. Neither the MDR, nor pH and osmolality of the applied Mg and Mg-6Ag materials were found to be influenced by the exposure to the coculture (Figure 18). Moreover, the Mg and Ag concentrations in the supernatant during Mg and Mg-6Ag degradation were measured to ascribe possible Mg-based

material specific effects to these ions (Figure 19). The detected Mg concentrations in the supernatants of degraded Mg and Mg-6Ag lay within an expected range of 3-6 mM [190-195]. Although, the MDR between cell-seeded and cell-free Mg materials was similar, a reduced Mg concentration could even be detected in some samples. This may be explained by cell-dependent mechanisms incorporating elements to surface bound degradation products or adsorbed proteins, which cannot be detected by AAS and ICP-MS [196,197]. Additionally, the differences in the methods to obtain the MDR and Mg concentration is pivotal. While for the MDR a mass loss in Mg is detected, AAS and ICP-MS measure a Mg concentration in the supernatant. Moreover, the determining the mass loss is an end point measurement, whereas the supernatant for the AAS and ICP-MS measurement can be taken in parallel to the ongoing experiment.

The Mg-based material degradation and the resulting surface-near effects (increase in pH, osmolality and constant hydrogen and ion release) may provoke the different relative cell numbers on the surface of degrading and non-degrading materials. Hence the following investigations aimed to explain these differences: Do the Mg-based materials evoke increased cancer cell specific cytotoxicity influencing specific carcinogenic processes, or do they inhibit only the cancer cell proliferation?

5.2 Cytotoxic potential of Mg-based materials

The results of the coculture characterization revealed profound differences in the cell number progression of cancer and healthy cells between coculture and monoculture. Cancer cell numbers remained relatively constant on degrading Mg and Mg-6Ag but strongly increased on non-degrading Ti-6Al-4V, especially under normoxia. This phenomenon on Mg and Mg-6Ag can be explained by

- (I) Tumor mass dormancy: establishment of an equilibrium of cancer cell proliferation and cytotoxicity
- (II) Cellular dormancy: constant cancer cell numbers through slowed or inhibited proliferation

To analyze, whether the constant tumor cell numbers on Mg and Mg-6Ag resulted from tumor mass dormancy, the cytotoxic potential of the Mg-based materials was tested with three different approaches.

Cytotoxicity was examined by the release of LDH, staining of primary amines and determination of live and dead cells by flow cytometry, and ROS/apoptosis staining. The LDH release showed no significant differences between the effects of Mg-based materials and the glass control (Figure 20A), indicating no degradation-dependent cytotoxicity. Slightly increased LDH release on Ti-6Al-4V may be explained by a denser cell layer compared to the glass control and thus a few cytotoxic events. Though, this increase is not as crucial as the LDH release of the lysed control where the cells were permeabilized. Though, Fischer *et al.* discouraged from using tetrazolium salt-based assays e.g. LDH (as performed in this thesis), MTT and XTT to measure cytotoxicity of Mg-based material, since the degradation products accelerate the color change reaction by formazan formation and give false results [198]. Therefore, the cytotoxic potential of slow degrading Mg and Mg-6Ag was double checked with other analyses.

To additionally distinguish live and dead cells on Mg-based material, primary amines were stained and analyzed by flow cytometry. These results obtained by flow cytometry confirmed the previous LDH results, once again.

Visualization of apoptosis (Caspase-3) and oxidative stress (ROS) showed a significantly higher formation of oxidative stress in the coculture on Mg-based materials than in the neg. control under normoxia (Figure 21). However, both coculture and monoculture, showed higher ROS production in healthy cells than cancer cells under normoxia. Unlike cancer cells, healthy cells have a sophisticated antioxidant system consisting of various active enzymes (e.g. SOD) to prevent excessive formation of free radicals and ROS [199]. These ROS can have two adverse effects in cancer cells. Low concentrations initiate and promote tumorigenesis in an early stage of tumor development. Increasing concentrations can lead to inhibited cancer cell growth and apoptosis, due to the dysregulated antioxidant system [200,201]. Consequently, the constant cancer cell numbers shown in Figure 17C may result from the increased ROS levels, which are not yet high enough to induce apoptosis. And indeed, Caspase-3 activity representing apoptosis was not significantly higher on Mg-based materials than on the glass control irrespective of oxygen level and number of cell types.

In summary, all three cytotoxicity analyses revealed no detectable cytotoxic effect of slow degrading Mg-based materials. Hence, constant tumor cell numbers on degrading material can be rather attributed to cellular dormancy than tumor mass dormancy.

5.3 Influence of slow degrading material on cancer cell hallmarks

Cytotoxicity of the slow degrading Mg-based materials towards osteosarcoma cells could not be observed. However, Mg and Mg-6Ag apparently had a negative, selective influence on tumorigenesis as displayed in Figure 17C. Therefore, the proliferation of cancer cells on Mg-based materials, as well as other cancer hallmarks that were already shown to be influenced by individual Mg degradation related effects were studied. Moreover, the surface-near effects of Mg degradation (pH, osmolality, Mg concentration) were analyzed separately regarding their influences on cancer cells utilizing the selected assays to evaluate demands on future Mg-based implants to evoke a certain anticancer activity.

Sustaining proliferative signaling

The previous results refuse the hypothesis that constant cancer cell numbers on Mg-based materials result from tumor mass dormancy. In turn, to cover the explanation of cellular dormancy, the proliferation of cancer and healthy cells was visualized by Ki-67 (Figure 22), an approved *in vitro* proliferation marker [202,203] and prognostic tool used in clinics [204,205]. On Mg and Mg-6Ag, the proportion of Ki-67 positive, thus proliferating cancer cells was significantly lower compared to that of non-degrading material and similar to proliferation-inhibited cells, which is supported by Zan *et al.* [206]. This explains the overall higher cell numbers, when seeding the coculture on Ti-6Al-4V compared to degrading Mg and Mg-6Ag. A possible reason is that the environmental conditions get unfavorable for cancer cells due to Mg degradation and consequently, the cancer cells stop proliferating and enter a dormancy phase, a mechanism that allows cancer cells to survive in unfavorable environmental and nutritional conditions. Different authors summarized in their work that cellular dormancy may be regulated by quiescence mechanisms to trigger this reversible growth arrest [207,208]. In fact, this thesis could also indicate such a reversibility of the dormant state, when osteosarcoma cells were detached from the material and were reseeded in “more favorable” conditions, subsequently starting to proliferate again (Figure 23). This is in accordance with

Discussion

other authors who reported of cancer cells that awake from dormancy once they stopped with a treatment [209,210]. Bragado and colleagues hypothesized with a special emphasis for the communication between cancer and microenvironment that surrounding stress conditions can change the gene expression profile of the cancer cells, thereby triggering cellular dormancy [211].

The material-based induction of a dormant state in osteosarcoma cells must be discussed carefully regarding the potential applicability for cancer treatment. On one hand cellular dormancy slows down the proliferation of the cancer cells and prevents severe disease courses, but on the other hand it eases the development of resistances against antiproliferative drugs [212]. Additionally, entering the dormant state protects the cancer cells from inducing apoptosis during Mg degradation-related harsh environmental conditions. To sensitize the cancer cells for a potential therapy with cytostatics or to induce apoptosis through the harsh degradation-related environmental conditions, the cancer cells were attempted to be forced back into the cell cycle using GSK2606414 to inhibit PERK. Among others, PERK activation was previously associated with cell cycle arrest in the G0/G1 phase following endoplasmic reticulum (ER) stress, consequently leading to unfolded protein response (UPR). Stress situations such as hypoxia [213] and oxidative stress [214] were already reported as potent PERK activators to avert cell damages [215-217]. Moreover, the surface-near effects that arise during Mg degradation feature a disapproved microenvironment for the cancer cells, which may lead to PERK activation and cancer cell dormancy. If the observed cancer cell proliferation inhibition was PERK dependent, the inhibition of PERK would result in proliferating cancer cells, even on degrading Mg-based materials. However, the PERK inhibitor GSK2606414 miscarried to raise the ratio of Ki-67 positive cancer cells on Mg-based materials and therefore, did not promote cancer cells reentering the cell cycle (Figure 24). Therefore, the Mg degradation-dependent cancer cell proliferation inhibition is PERK independent and execute through other signaling pathways.

Another pathway for signal transduction resulting in cancer cell proliferation inhibition is triggered by TGF- β [218]. Binding of TGF- β to its receptors "TGFBR" leads to the phosphorylation of the SMAD2/SMAD3 complex that can migrate into the nucleus and initiates the transcription of p21, a CDK-2 inhibitor [219]. It was previously shown that an accelerated inhibition of CDK-2 by a high amount of p21 was responsible for cells entering a transient G0-like state [220]. Such decreased levels of phosphorylated SMAD2/SMAD3 in the cocultured cells seeded on degrading materials (Figure 25) could not be confirmed in the present study.

A third signaling pathway to inhibit cell proliferation in cancer cells includes IL-8. The cytokine IL-8 is an important factor that links many different signaling pathways and is involved in cell proliferation, inflammation, angiogenesis and metastasis in different cancers [221-223]. If the Mg degradation-dependent inhibition of the cancer cell proliferation involved indeed IL-8, a significant lower IL-8 expression would be expected in the presence of Mg and Mg-6Ag. In this thesis, the normalized IL-8 levels were initially higher for the coculture on the glass control than on Mg-based materials, which underlines the higher initial cancer cell proliferation on glass. However, the overall IL-8 concentration in all samples was very low. Such a low expression of IL-8 in Saos-2 was previously also shown by Mussano *et al.* [224]. The already low IL-8 expression in Saos-eGFP thus minimizes the significance of the results. Therefore, a detailed assessment of the responsible signaling pathway is not possible. Thus, the exact signaling pathways that lead to the observed proliferation inhibition in cancer cells on Mg-based materials are still unknown and should be elucidated in future studies. This may include the utilization of a different cancer cell type with a higher endogenous IL-8 level or the focus on other signaling pathways such as integrin signaling or the MAPK pathway, as suggested by [225].

Furthermore, the unique contributions of Mg degradation dependent surface-near effects on this cancer cell proliferation inhibition are potentially interesting for tailoring Mg based materials. Therefore, cell culture medium samples mimicking a distinct surface-near effect were prepared and tested. It is known that the local degradation-dependent surface-near effects, such as pH and osmolality, can strongly differ from the values in global [226]. Hence, the single parameter solutions were purposely adjusted with a higher pH or osmolality than measured in the supernatant of degrading Mg-based materials (Figure 18). Separating the Mg degradation into single parameters showed a similar cell number progression between Mg and an increased osmolality (Figure 26). Increasing the pH resulted in a significant low number of Ki-67 positive cancer cells, as observed for cells in direct contact with Mg discs (Figure 27). Contrary to the common opinion that Mg can dramatically increase cancer cell proliferation due to its cofactor function in enzymes [4], an increase in Mg concentration resulted in lowered relative Ki-67 positive osteosarcoma cell numbers compared to the glass control (Figure 27), which is in accordance to Yun *et al.* [227]. The findings that a manipulation of extracellular pH can result in inhibited cancer growth is in accordance with other publications [228]. Neri and Supuran summarized in their review the influence of inhibiting different pH regulation proteins (carbonic anhydrases, vacuolar ATPase or the $\text{Na}^+/\text{HCO}_3^-$ cotransporter) on the tumorigenesis [229]. This protein inhibition led to the normalization of pH_i and pH_e similar to healthy cells, consequently impairing tumor growth. Other strategies to increase the extracellular pH of cancer tissue include the oral administration of alkaline substances, consisting of trisodium citrate and sodium [230]. However, only a high and frequently administered dose would maintain a sufficiently alkaline environment of the tumor tissue [231,232]. A further problem is the sufficient transport of the alkaline agents directly to the tumor site. Local therapy strategies can overcome these issues by directly functioning at the tumor [233], as also hypothesized for Mg-based implants. Another way in which the pH_e of a cancer cell can influence tumor growth is via proton-sensing G-protein coupled receptors (GPR). The GPR68 for example is upregulated in various cancers e.g., osteosarcoma and reacts to extracellular acidity [234,235]. By sensing an acidic microenvironment, GPR68 promotes cell proliferation by PLC/IP3/ Ca^{2+} signal transduction and eventually activation of MEK/ERK [236]. In that way, alkalization of the microenvironment can suppress tumor growth [237].

Increasing the surrounding medium osmolality only led to increased numbers of Ki-67 positive cancer cells, although the cell number progressions were comparable to that of Mg degradation. This effect can be explained by findings from Wu and colleagues [238]. There, increasing the osmolality by using Mg alloy extracts resulted in a higher proportion of cells resting in G2/M phase and a lower proportion of cells facing a G0/G1 arrest compared to the control. This would lead to an increase in Ki-67 positive cells, as observed in the present thesis. For a better understanding, additional cell cycle analyses via flow cytometry should be performed with the coculture in future. Adverse effects on the cell viability due to the increased osmolality were not expected [239,240].

Avoiding immune destruction

Immunosurveillance is an endogenous process to eradicate foreign or transformed cells and to protect the organism at an early stage of virus infection or malignant cell transformation. This process leads inevitably, but often only after many years, to mutations in individual cancer cells that allow them to withstand recognition by the immune system [241]. Recent studies showed increased lymphocyte activity, in detail T cells and NK cells with Mg supplementation [242,243]. Therefore, this thesis should also reveal if Mg degradation has a beneficial effect on the exposure of disguised cancer cells or a boosting effect on the cytolytic function of NK cells to target and kill transformed cells. No significant cancer cell number reductions could be observed upon NK cell addition to the coculture for 4 h in comparison to the control without NK

Discussion

cells (Figure 33). This may result from a too short incubation time, low cytotoxicity or inactive NK cells. The low cytotoxicity of NK cells can result from heterogeneous NK phenotypes within solid tumors [244]. The expression of CD56 and CD16 on the NK cell surface (CD56^{dim}, CD16⁺) is associated with increased cytotoxicity, while low cytotoxicity and increased metabolic activity is found for NK cells negative for CD16 (CD56^{bright}, CD16⁻) [245], as reported for NK-92 [246]. Although the NK cells did not reduce the cancer cell numbers, even not in the presence of Mg, a significant increase in NK activity could be detected with Mg materials. Granzyme B secretion was increased in the presence of Mg-based materials but coculture independent (Figure 34). Perforin secretion was significantly higher when NK cells faced the coculture compared to the cell-free material (Figure 35). This would confirm that perforin is majorly secreted upon binding to the cancer cells and activation of NK cells through activating receptors, such as NKG2D [247]. Furthermore, the presence of Mg increased granzyme B secretion, indicating an increased cytotoxic potential of NK cells.

The change of environmental conditions around the tumors due to the Mg degradation may also affect NK cell function and binding affinity to the target cells. Increasing the Mg concentration was already shown to positively correlate with the NKG2D expression on the NK-cell surface [243,248]. Moreover, tumor acidity was shown to correlate with the activation of coinhibitory receptors, suppression of costimulatory receptors, such as DNAM-1, and with the production of IFN- γ inhibiting the function of e.g., cytotoxic T cells and NK cells [249,250]. Thus, neutralization of the tumor microenvironmental pH during Mg degradation may restore immune cell function and delay tumor growth [249,251]. Mg degradation may not only directly affect NK cells through altering their surface marker profile but also indirectly by cytokine activity and NK cell receptor ligand changes. Perforin and granzyme B are activated with the release of acidic granules from the NK cells into the immunologic synapse with a neutral pH [252,253]. Though, the activity of both cytokines may be diminished again at the acidic tumor proximity, which can be prevented by Mg degradation dependent pH increase.

Inducing angiogenesis

Angiogenesis induction is a critical part of cancer biology to maintain a sufficient supply of nutrients and oxygen and to promote tumor growth. To investigate the influences of Mg-based materials on the cancer-induced angiogenesis, conditioned media of Mg, Mg-6Ag and glass seeded with the coculture or monocultures under normoxia and hypoxia were prepared. On one hand, this ensured simplification of the methods avoiding opaque material and finding the optimal conditions of a triple culture with three cell lines, but on the other hand it did not diminish the relevance of the results. Figure 36 revealed that endothelial cell permeability tended to increase for the glass control of cell-containing conditioned media compared to the respective samples with Mg-based materials. This is in accordance to Zhu *et al.* [254] who found a lower endothelial cell permeability after Mg treatment compared to Mg deficiency *in vitro* and *in vivo*. The authors explained this with an increased expression of barrier stabilizing mediators such as cyclic adenosine monophosphate (cAMP), fibroblast growth factor (FGF) and endothelial nitric oxide synthase (eNOS) on mRNA and protein level, which may lead to an increased tight junction assembly and endothelial barrier function [254-256]. Conversely, Mg treatment led to an increased expression of VEGF, a main inducer of endothelial permeability, on mRNA level. However, its expression on protein level did not change [254], as likewise seen in this study (Figure 38), suggesting an enhancing effect of Mg on endothelial cell permeability.

VEGF also plays a key role in inducing endothelial cell proliferation and migration during a later stage of angiogenesis. The results presented here showed that cell related conditioned media of the glass control and Mg increased HUVEC proliferation, while the material control (material without cells) conditioned media did not reveal changes (Figure 37). This leads to the

assumption that Mg degradation itself does not promote endothelial cell proliferation, but cancer cells and fibroblasts that secrete proliferation inducing cytokines [257]. The action of extracellular Mg and Mg degradation on endothelial cell proliferation is ambiguously discussed in the literature, but thought to be rather proliferation inducing [254,258-260] than inhibiting [261,262]. A decreased HUVEC migration in connection with Mg and Mg-6Ag could be shown in this study. Interestingly, the endothelial cell migration inhibition faded when seeding the coculture on the materials (normoxia, hypoxia) or just the monocultures of cancer and healthy cells (normoxia). In contrast to this, several authors showed an elevated endothelial migration with a concentration of Mg<20 mM [254,258,261,262]. Increased MMP-2 and MMP-9 levels, likewise presented in this study, may lead to ECM degradation and subsequent initiation of endothelial cell migration [263]. VEGF was also found to increase endothelial cell migration in the presence of Mg supplementation (5 mM) [264]. The ability of endothelial cells to form tube-like structures was increased with Mg under normoxic conditions (Figure 40). These results are comparable to the findings of Gao and colleagues [265] and indicate increased angiogenesis with Mg supplementation under normoxia. However, Mg supplementation seemed to have no major influences on tube formation under hypoxia. Since cancer cells induces angiogenesis primarily under hypoxic conditions, it can be summarized that Mg-based materials potentially do not influence the differentiation of endothelial cells into capillary structures.

Activating invasion and metastases

Not only inhibition of cancer cell proliferation but also metastases forming secondary tumors should be considered for an effective cancer treatment [266]. Invasive cancer cells stop proliferating [267] and are therefore not targeted by cytostatic drugs. Therefore, the influence of Mg degradation on cell migration (Figure 28) and invasion (Figure 29), as key events of metastases, were also studied in this thesis. Determining the cell migration of the coculture revealed a significant migration inhibition caused by Mg-based materials in comparison to the glass control. This migration inhibition was reduced when cancer cells were only investigated as a monoculture, suggesting an additional migration inhibiting action of the fibroblasts [268,269]. Similar results were obtained for cell invasion, shown in Figure 29 and Figure 30. In accordance with our results, Wu and colleagues could show that extracts from different Mg-based materials inhibited migration and invasion of the osteosarcoma cell line U2OS [238]. The authors suggested that these findings resulted from MAPK signaling promoting by an increased expression of ERK, JNK and p38.

The secretion of MMP-2, MMP-9 and their inhibitor TIMP-1 from the coculture was investigated in this thesis because these molecules are major driving metastasis factors (Figure 31). Both, MMP-2 and MMP-9 secretion was found to be higher on Mg-based materials compared to the glass control. The inhibiting effect was more pronounced for MMP-9 secretion as reported by Roomi for other osteosarcoma cell lines [270]. A higher MMP secretion on Mg and Mg-6Ag may be explained by the higher proportion of fibroblasts in the coculture compared to the glass control (Figure 17C), suggesting the fibroblasts as the major source of MMP. In fact, several authors reported an increased MMP-2 level after coculture of cancer cells and fibroblasts for more than 48 h, where the cancer cells promoted MMP-2 production in fibroblasts [271-273]. Saad *et al.* could conclude from their work that inactive MMP-2 in fibroblasts can be activated and very quickly released through fibronectin residing on the surface of adjacent breast cancer cells [274]. This MMP-2 activation and release will lead to ECM degradation and subsequent promotion of cancer cell invasion and metastases. In contrast to this, MMP-9 expression in fibroblasts could only be provoked by coculture with cancer cells [43,275].

Surface-near effects induced by Mg degradation may also affect MMP and TIMP expression and activity. The expression of both, MMP-2 and MMP-9, was previously documented to be

Discussion

increased during Mg deficiency [45,276], while TIMP-1 expression elevated by a factor of 4 with increasing Mg concentrations up to 10 mM [277]. Furthermore, different authors showed that an acidic tumor microenvironment can promote MMP-9 production, reducing it at normal pH_e [68,278]. Therefore, it can be assumed that Mg degradation leading to an alkaline pH_e should decrease MMP-9 secretion even more, explaining the steady decrease observed here (Figure 31). Contrary to this, Razaq *et al.* reported a very low TIMP-1 activity at acidic pH, but increasing with increasing pH_e , as observed during Mg degradation. Therefore, TIMP can inhibit MMP activity although MMP-2 and MMP-9 were expressed [279].

Furthermore, the cell migration under the influence of selected parameter resulting during Mg degradation was investigated (Figure 32). The results obtained from Mg degradation itself were comparable to those of the tested single parameters. Only the extract with 30 mM Mg tended to inhibit migration even more compared to the Mg degradation in the direct assay. This is in accordance with the results from Amberg *et al.*, who examined the influence of increased Mg-ion and osmolality on human gingival fibroblasts [280]. The authors reported a reduced migration with increased $MgCl_2$ concentrations that was not provoked by the increased resulting osmolality but by the elevated Mg-ion concentration. Similar results were shown for MG63 [281] and different prostate cancer cells [282]. Acidity of the tumor surrounding appears to be important again as it was shown to promote invasion and metastases, described by multiple authors [116,283,284]. Furthermore, neutralization of the tumor surrounding pH with alkaline oral administered agents was already reported to inhibit metastases [285,286]. Moreover, the increased osmolality seems to play a role in cancer cell migration as well. Aside from the well-known classical migration process including actin polymerization and myosin II-mediated contraction [287-289], a new model recently got attention, named osmotic engine model. This model relies on a water influx through aquaporins on the leading edges of polarized, migrating cells to form lamellipodia [290,291]. Papadopoulos and Saadoun recently highlighted the important role of aquaporins on cancer biology and overexpression in various cancer types [292]. The osmotically driven water transport through aquaporins can be attenuated by increasing the extracellular osmolality as it is observed for Mg degradation. Since cells are usually maintained in isotonic cell culture medium between 310-360 mOsmol/Kg (according to supplier information) *in vitro*, this leads to water efflux from the cells and a slower and undirected migration.

The influence of Mg-based materials on the selected cancer hallmarks is summarized in Figure 44.

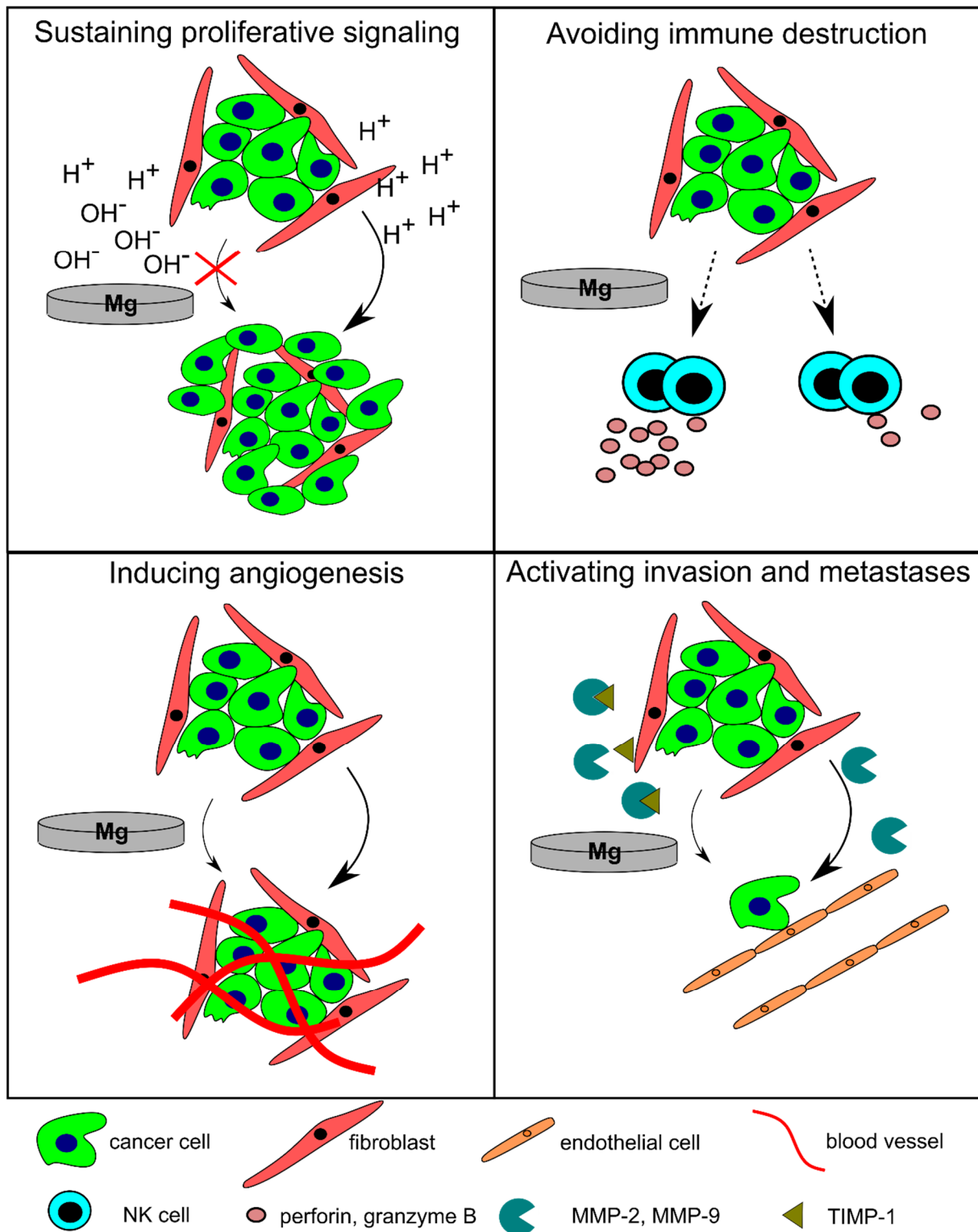


Figure 44. Summary of the impact of Mg-based materials on selected cancer hallmarks. The increasing pH during Mg degradation inhibits cancer cell proliferation. Mg degradation was shown to increase perforin and granzyme B release from NK cells. With Mg, the cancer-induced angiogenesis was decreased. Indeed, Mg degradation led to an increased release of MMP-2 and MMP-9, however, also the concentration of their inhibitor TIMP-1 increased.

5.4 Degradation tailoring for anticancer applications

The comprehensive scope of this thesis was to elucidate the possible application of Mg-based materials as candidates for cancer therapy. The slow-degrading materials (0.2 mm/a) showed no cytotoxicity *in vitro* against the cancer cells. Enhancing the degradation rate *in vitro* will lead to an increase in surface-near effects and increased cytotoxicity due to the harsh cell environment. Therefore, a degradation rate window between 1-2.4 mm/a was hypothesized for this part of the thesis. Materials with a degradation rate below 1 mm/a were thought to only insignificantly affect cancer cell cytotoxicity, as shown for slow degrading materials (Figure 20), while a degradation rate above 2.4 mm/a likely kills everything on the material surface nonspecifically. The degradation rate increase of the Mg-6Ag alloy was realized by T6 aging treatment that do not majorly diminish the mechanical material properties. This treatment artificially produces precipitates whose amount positively correlates with the degradation rate [34]. Nevertheless, the actual treatment was done in a partner project and will be only shortly discussed. The optimal T6 heat-treatment parameters were initially chosen and adjusted due to the resulting degradation rates (Figure S2-S4). The final heat treatment at 200 °C for 7-15 min resulted in MDR of Mg-6Ag that lay in the desired degradation rate window (Figure 41). The chosen T6 aging treatment procedure allowed the observation of increased MDR, pH and osmolality values even for small treatment time differences. Accompanied with the elevation of these parameters, a decreasing overall cell number of the coculture could be observed within seven days (Figure 43). As shown for the slow degrading materials, the cancer cells appeared to be more sensitive to the T6 treated Mg-6Ag alloy compared to the healthy cells. The increase in MDR is also reflected by increasing Mg concentrations (Figure S5) and probably Ag concentrations in the supernatant, which potentially may also affect the observed differences in cell viability between cancer and healthy cells. Mg concentration was shown to increase up to 50-70 mM. While a concentration of up to 5 mM MgCl₂ seemed to be well-tolerated by the cells (Figure S6), Feyerabend *et al.* similarly indicated different Mg sensitivities between cancer and healthy cells. While HUCPV reached a cell viability of 60-70 %, the viability of the osteosarcoma cell line MG63 declined below 30 % with 70 mM MgCl₂ [293]. Regarding the sensitivity towards Ag in the supernatant, healthy and cancer cell viability dramatically decreased with an AgNO₃ concentration of around 60 nM (Figure S6). This concentration differs approximately by the magnitude of 10 compared to the literature that states IC₅₀ values (half maximal inhibitory concentration) between 0.31 and 0.37 mM dependent on the Ag source and cell types [294,295]. This shows that Ag in a sufficient concentration might affect cell viability, whereas this concentration is not reached with slow degrading Mg-6Ag alloys (Figure 19).

To summarize this, slow degrading material could not evoke cytotoxicity towards cancer cells. With the increase of the degradation rate and accompanied surface-near effects in fast degrading materials, cells were killed unspecifically. However, these degradation-dependent effects can be further tuned to kill cancer cells specifically.

5.5 Suitability of Mg-based materials for osteosarcoma therapy

The potential application of Mg in cancer therapy seems to be disadvantageous at first sight since cancer cells are characterized by certain avidity for Mg [4]. This leads to an intracellular Mg accumulation [296] and can theoretically contribute to increased cancer cell proliferation due to the Mg activity as a cofactor for enzymes, or involvement in nucleic acid and protein metabolism [297-299]. Though, the slow-degrading Mg-based materials used in this thesis

showed promising anticancer activity with minimal harm to fibroblasts. Explanations for these unexpected effects against tumorigenesis may be the calcium (Ca)/Mg competition. Therefore, the Mg degradation-dependent increase in extracellular Mg concentrations can lead to a decrease in Ca-dependent cellular processes such as proliferation and cell motility [300,301]. Moreover, Mg degradation is not only characterized by increased extracellular Mg concentration, but the cells also face the change of the surrounding by surface-near effects. In this thesis, the elevating pH during Mg degradation was shown to be the driving force against tumorigenesis. Indeed, neutralization of the tumor surrounding was already associated with inhibition of tumor growth [229] and metastases [285,286], but it could also be beneficial for combined cancer therapy. Entry of weak basic chemotherapeutic agents such as doxorubicin are pH_e dependent [302,303]. In the acidic tumor environment they are protonated, thus get a positive charge that dramatically diminishes the membrane permeation, a phenomenon called pH partition [302]. Raising the pH_e of tumors during Mg degradation has the potential to facilitate the chemotherapeutic drug entry, and consequently may reduce tumor chemo resistance. This opens the door for possible drug coatings on the Mg-based material surface or drug encapsulation in porous material to increase the efficacy of cytotoxic agents. Furthermore, Damen *et al.* [304] suggested three possible strategies to eradicate dormant cancer cells:

- (I) combining systemic and targeted approaches to kill the dormant cells
- (II) continuous force into the dormant state
- (III) reawakening and killing of proliferating cancer cells

Systemic chemotherapies do not target dormant cancer cells. However, Pajic *et al.* [305] could identify the alkylating agent nimustine to target non-proliferating cancer cells in a mouse model. Research about the second strategy is more advanced at the moment. Therapeutic drugs such as tamoxifen were already shown to keep the dormant cells in a dormant state [306]. The disadvantage of this therapy approach is that it requires a lifelong drug administration, which is accompanied with high costs and burden of the patient's life. The third strategy was simulated in this thesis (section 4.3.2), which turned out to be not efficient. Therefore, the exact signaling pathway that induces the cancer cell proliferation inhibition has to be identified. An imprudent reawakening of the dormant cancer cells can also promote the cancer outgrowth, which is why this strategy must be highly personalized and controlled.

Although the slow-degrading Mg-based materials did not lead to osteosarcoma cell death, the materials showed very promising action against several cancer hallmarks, which can be beneficial for the cancer treatment. This may be due to the unfavorable environment that inhibits tumor spreading on one hand but on the other hand is not harsh enough to lead to cancer cell eradication. Severing the environmental conditions can be provoked by T6 aging treatment as shown for Mg-6Ag. This increased the MDR thus also surface-near effects but maintained mechanical properties at the same time. Both, the tensile strength as well as the young's modulus (material stiffness) of Mg-based materials are comparable to that of cortical bone [307,308], which makes Mg materials especially attractive for osteosarcoma therapy. These materials can therefore provide sufficient stability after resection of small bones, avoid spreading of residual cancer cells and cancer recurrence and stimulate the growth of new, healthy bone tissue in the excised area.

6 Conclusion

In the scope of this thesis, a coculture model of the TME in form of an osteosarcoma-fibroblast coculture was described as a beneficial monitoring system on opaque material. Due to the different fluorescence labeling, both cell types could be efficiently distinguished, and material-related effects were assigned cell-specifically.

Slow degrading materials exerted cancer-specific cytostatic activity by inhibiting the cancer cell proliferation rather than inducing cytotoxicity. This effect was not observed on the non-degrading Ti and glass controls, which suggests this effect as degradation-dependent. Furthermore, the monocultures of cancer and healthy cells produced entirely different results, which indicates the necessity of more complex cell culture systems than monocultures for significant findings. The analysis of major cancer hallmark-related effects of slow degrading Mg and Mg-6Ag revealed promising anticancer activity. Although NK cells did not induce cytotoxicity towards the osteosarcoma cells in presence of Mg-based materials, the expression of cytolytic cytokines was increased, underlining the general increased NK cell activity in the presence of Mg-based materials. Cancer cell-induced angiogenesis was decreased with Mg-based materials, which was shown by a reduced VEGF release under hypoxia, and permeability, migration and proliferation of endothelial cells. The cancer cell migration and invasion were reduced in presence of Mg-based materials, which was determined by expression levels of MMP-2, MMP-9 and TIMP-1. The Mg degradation-dependent increase in pH and osmolality were found to be the major influencing surface-near effects exerting anticancer activity.

T6 treatment of Mg-6Ag was shown to be a promising method for degradation rate tailoring, as well as to increase pH and osmolality. This work suggests treatment parameters and durations to yield an exposure-response relationship *in vitro*: With increasing Mg degradation, the pH and osmolality increased. As a result of this, cell numbers of healthy and cancer cells decreased, with the latter to a higher extend, until the environmental conditions got too harsh and cells were killed unspecifically.

To conclude, the results presented in this thesis suggest a promising anticancer activity of Mg-based materials *in vitro*. This is a promising basis to proof these effects in more complex *in vitro* models (3D) and finally *in vivo* to draw final conclusions about the underlying processes.

References

1. Swaminathan, R. Magnesium metabolism and its disorders. *Clin Biochem Rev* **2003**, *24*, 47-66.
2. Saris, N.E.; Mervaala, E.; Karppanen, H.; Khawaja, J.A.; Lewenstam, A. Magnesium. An update on physiological, clinical and analytical aspects. *Clin Chim Acta* **2000**, *294*, 1-26, doi:10.1016/s0009-8981(99)00258-2.
3. Romani, A.M. Magnesium homeostasis in Mammalian cells. *Metal ions in life sciences* **2013**, *12*, 69-118, doi:10.1007/978-94-007-5561-1_4.
4. de Baaij, J.H.; Hoenderop, J.G.; Bindels, R.J. Magnesium in man: implications for health and disease. *Physiol Rev* **2015**, *95*, 1-46, doi:10.1152/physrev.00012.2014.
5. Wallach, S. Magnesium: Its Biologic Significance, by J. K. Aikawa. *Medical Physics* **1982**, *9*, 588-589, doi:<https://doi.org/10.1118/1.595176>.
6. Fox, C.; Ramsoomair, D.; Carter, C. Magnesium: its proven and potential clinical significance. *South Med J* **2001**, *94*, 1195-1201.
7. Rude, R.K. Magnesium Deficiency: A Cause of Heterogenous Disease in Humans. *Journal of Bone and Mineral Research* **1998**, *13*, 749-758, doi:<https://doi.org/10.1359/jbmr.1998.13.4.749>.
8. Maguire, M.E.; Cowan, J.A. Magnesium chemistry and biochemistry. *Biomaterials* **2002**, *15*, 203-210, doi:10.1023/A:1016058229972.
9. Touyz, R.M. Magnesium in clinical medicine. *Frontiers in bioscience : a journal and virtual library* **2004**, *9*, 1278-1293, doi:10.2741/1316.
10. Vormann, J. Magnesium: nutrition and metabolism. *Molecular aspects of medicine* **2003**, *24*, 27-37, doi:10.1016/s0098-2997(02)00089-4.
11. Elin, R.J. Magnesium metabolism in health and disease. *Disease-a-month : DM* **1988**, *34*, 161-218, doi:10.1016/0011-5029(88)90013-2.
12. Lowenstein, F.W.; Stanton, M.F. Serum magnesium levels in the United States, 1971-1974. *Journal of the American College of Nutrition* **1986**, *5*, 399-414, doi:10.1080/07315724.1986.10720143.
13. Alfrey, A.C.; Miller, N.L. Bone magnesium pools in uremia. *The Journal of clinical investigation* **1973**, *52*, 3019-3027, doi:10.1172/JCI107500.
14. Wang, J.; Xu, J.; Liu, W.; Li, Y.; Qin, L. Biodegradable Magnesium (Mg) Implantation Does Not Impose Related Metabolic Disorders in Rats with Chronic Renal Failure. *Scientific Reports* **2016**, *6*, 26341, doi:10.1038/srep26341.
15. Zhao, D.; Huang, S.; Lu, F.; Wang, B.; Yang, L.; Qin, L.; Yang, K.; Li, Y.; Li, W.; Wang, W., et al. Vascularized bone grafting fixed by biodegradable magnesium screw for treating osteonecrosis of the femoral head. *Biomaterials* **2016**, *81*, 84-92, doi:10.1016/j.biomaterials.2015.11.038.
16. Witte, F.; Kaese, V.; Haferkamp, H.; Switzer, E.; Meyer-Lindenberg, A.; Wirth, C.J.; Windhagen, H. In vivo corrosion of four magnesium alloys and the associated bone response. *Biomaterials* **2005**, *26*, 3557-3563, doi:10.1016/j.biomaterials.2004.09.049.
17. Bettman, R.B.; Zimmerman, L.M. The use of metal clips in gastrointestinal anastomosis. *The American Journal of Digestive Diseases* **1935**, *2*, 318-321, doi:10.1007/BF03000817.
18. Payr, E. Ueber Verwendung von Magnesium zur Behandlung von Blutgefässerkrankungen. *Deutsche Zeitschrift für Chirurgie* **1902**, *63*, 503-511, doi:10.1007/BF02816557.
19. Witte, F. The history of biodegradable magnesium implants: A review. *Acta Biomaterialia* **2010**, *6*, 1680-1692, doi:<https://doi.org/10.1016/j.actbio.2010.02.028>.
20. Zhang, Y.; Xu, J.; Ruan, Y.C.; Yu, M.K.; O'Laughlin, M.; Wise, H.; Chen, D.; Tian, L.; Shi, D.; Wang, J., et al. Implant-derived magnesium induces local neuronal production of CGRP to improve bone-fracture healing in rats. *Nat Med* **2016**, *22*, 1160-1169, doi:10.1038/nm.4162.

References

21. Kraus, T.; Fischerauer, S.F.; Hänzi, A.C.; Uggowitzer, P.J.; Löffler, J.F.; Weinberg, A.M. Magnesium alloys for temporary implants in osteosynthesis: in vivo studies of their degradation and interaction with bone. *Acta Biomater* **2012**, *8*, 1230-1238, doi:10.1016/j.actbio.2011.11.008.
22. Henderson, S.E.; Verdelis, K.; Maiti, S.; Pal, S.; Chung, W.L.; Chou, D.-T.; Kumta, P.N.; Almarza, A.J. Magnesium alloys as a biomaterial for degradable craniofacial screws. *Acta biomaterialia* **2014**, *10*, 2323-2332.
23. Tie, D.; Guan, R.; Liu, H.; Cipriano, A.; Liu, Y.; Wang, Q.; Huang, Y.; Hort, N. An in vivo study on the metabolism and osteogenic activity of bioabsorbable Mg-1Sr alloy. *Acta Biomater* **2016**, *29*, 455-467, doi:10.1016/j.actbio.2015.11.014.
24. Wang, J.-L.; Xu, J.-K.; Hopkins, C.; Chow, D.H.-K.; Qin, L. Biodegradable Magnesium-Based Implants in Orthopedics—A General Review and Perspectives. *Advanced Science* **2020**, *7*, 1902443, doi:<https://doi.org/10.1002/advs.201902443>.
25. Walker, E.K.; Nauman, E.A.; Allain, J.P.; Stanciu, L.A. An in vitro model for preclinical testing of thrombogenicity of resorbable metallic stents. *Journal of biomedical materials research. Part A* **2015**, *103*, 2118-2125, doi:10.1002/jbm.a.35348.
26. Windhagen, H.; Radtke, K.; Weizbauer, A.; Diekmann, J.; Noll, Y.; Kreimeyer, U.; Schavan, R.; Stukenborg-Colsman, C.; Waizy, H. Biodegradable magnesium-based screw clinically equivalent to titanium screw in hallux valgus surgery: short term results of the first prospective, randomized, controlled clinical pilot study. *BioMedical Engineering OnLine* **2013**, *12*, 62, doi:10.1186/1475-925X-12-62.
27. Plaass, C.; von Falck, C.; Ettinger, S.; Sonnow, L.; Calderone, F.; Weizbauer, A.; Reifenrath, J.; Claassen, L.; Waizy, H.; Daniilidis, K., et al. Bioabsorbable magnesium versus standard titanium compression screws for fixation of distal metatarsal osteotomies – 3 year results of a randomized clinical trial. *Journal of Orthopaedic Science* **2018**, *23*, 321-327, doi:<https://doi.org/10.1016/j.jos.2017.11.005>.
28. Lee, J.W.; Han, H.S.; Han, K.J.; Park, J.; Jeon, H.; Ok, M.R.; Seok, H.K.; Ahn, J.P.; Lee, K.E.; Lee, D.H., et al. Long-term clinical study and multiscale analysis of in vivo biodegradation mechanism of Mg alloy. *Proc Natl Acad Sci U S A* **2016**, *113*, 716-721, doi:10.1073/pnas.1518238113.
29. Verheye, S.; Wlodarczak, A.; Montorsi, P.; Bennett, J.; Torzewski, J.; Haude, M.; Vrolix, M.; Buck, T.; Aminian, A.; van der Schaaf, R.J., et al. Twelve-month outcomes of 400 patients treated with a resorbable metal scaffold: insights from the BIOSOLVE-IV registry. *EuroIntervention* **2020**, *15*, e1383-e1386, doi:10.4244/eij-d-18-01058.
30. Zhang, Y.; Ren, L.; Li, M.; Lin, X.; Zhao, H.; Yang, K. Preliminary Study on Cytotoxic Effect of Biodegradation of Magnesium on Cancer Cells. *Journal of Materials Science & Technology* **2012**, *28*, 769-772, doi:[https://doi.org/10.1016/S1005-0302\(12\)60128-5](https://doi.org/10.1016/S1005-0302(12)60128-5).
31. Wang, Q.; Jin, S.; Lin, X.; Zhang, Y.; Ren, L.; Yang, K. Cytotoxic Effects of Biodegradation of Pure Mg and MAO-Mg on Tumor Cells of MG63 and KB. *Journal of Materials Science & Technology* **2014**, *30*, 487-492, doi:<https://doi.org/10.1016/j.jmst.2014.03.004>.
32. Li, M.; Ren, L.; Li, L.; He, P.; Lan, G.; Zhang, Y.; Yang, K. Cytotoxic Effect on Osteosarcoma MG-63 Cells by Degradation of Magnesium. *Journal of Materials Science & Technology* **2014**, *30*, 888-893, doi:<https://doi.org/10.1016/j.jmst.2014.04.010>.
33. Walker, J.; Shadanbaz, S.; Woodfield, T.B.; Staiger, M.P.; Dias, G.J. Magnesium biomaterials for orthopedic application: a review from a biological perspective. *J Biomed Mater Res B Appl Biomater* **2014**, *102*, 1316-1331, doi:10.1002/jbm.b.33113.
34. Ghali, E.; Dietzel, W.; Kainer, K.-U. General and localized corrosion of magnesium alloys: A critical review. *Journal of Materials Engineering and Performance* **2004**, *13*, 7-23, doi:10.1361/10599490417533.
35. Anastassopoulou, J.; Theophanides, T. Magnesium-DNA interactions and the possible relation of magnesium to carcinogenesis. Irradiation and free radicals. *Crit Rev Oncol Hematol* **2002**, *42*, 79-91, doi:10.1016/s1040-8428(02)00006-9.

36. Ralec, C.; Henry, E.; Lemor, M.; Killelea, T.; Henneke, G. Calcium-driven DNA synthesis by a high-fidelity DNA polymerase. *Nucleic Acids Research* **2017**, *45*, 12425-12440, doi:10.1093/nar/gkx927.
37. Williams, N.H. Magnesium Ion Catalyzed ATP Hydrolysis. *Journal of the American Chemical Society* **2000**, *122*, 12023-12024, doi:10.1021/ja0013374.
38. Blum, M.; Chang, H.Y.; Chuguransky, S.; Grego, T.; Kandasamy, S.; Mitchell, A.; Nuka, G.; Paysan-Lafosse, T.; Qureshi, M.; Raj, S., et al. The InterPro protein families and domains database: 20 years on. *Nucleic Acids Res* **2021**, *49*, D344-d354, doi:10.1093/nar/gkaa977.
39. Zu, H.; Yi, X.; Zhao, D. Transcriptome sequencing analysis reveals the effect of combinative treatment with low-intensity pulsed ultrasound and magnesium ions on hFOB1.19 human osteoblast cells. *Mol Med Rep* **2018**, *18*, 749-762, doi:10.3892/mmr.2018.9006.
40. Rojas, A.; Padidam, M.; Cress, D.; Grady, W.M. TGF-beta receptor levels regulate the specificity of signaling pathway activation and biological effects of TGF-beta. *Biochim Biophys Acta* **2009**, *1793*, 1165-1173, doi:10.1016/j.bbamcr.2009.02.001.
41. Kwak, H.J.; Park, M.J.; Cho, H.; Park, C.M.; Moon, S.I.; Lee, H.C.; Park, I.C.; Kim, M.S.; Rhee, C.H.; Hong, S.I. Transforming growth factor-beta1 induces tissue inhibitor of metalloproteinase-1 expression via activation of extracellular signal-regulated kinase and Sp1 in human fibrosarcoma cells. *Mol Cancer Res* **2006**, *4*, 209-220, doi:10.1158/1541-7786.Mcr-05-0140.
42. Cawston, T.; Billington, C.; Cleaver, C.; Elliott, S.; Hui, W.; Koshy, P.; Shingleton, B.; Rowan, A. The regulation of MMPs and TIMPs in cartilage turnover. *Ann N Y Acad Sci* **1999**, *878*, 120-129, doi:10.1111/j.1749-6632.1999.tb07678.x.
43. Singer, C.F.; Kronsteiner, N.; Marton, E.; Kubista, M.; Cullen, K.J.; Hirtenlehner, K.; Seifert, M.; Kubista, E. MMP-2 and MMP-9 Expression in Breast Cancer-Derived Human Fibroblasts is Differentially Regulated by Stromal-Epithelial Interactions. *Breast Cancer Research and Treatment* **2002**, *72*, 69-77, doi:10.1023/A:1014918512569.
44. Ko, K.; Yazumi, S.; Yoshikawa, K.; Konda, Y.; Nakajima, M.; Chiba, T.; Takahashi, R. Activation of fibroblast-derived matrix metalloproteinase-2 by colon-cancer cells in non-contact Co-cultures. *Int J Cancer* **2000**, *87*, 165-171.
45. Yue, H.; Uzui, H.; Lee, J.D.; Shimizu, H.; Ueda, T. Effects of magnesium on matrix metalloproteinase-2 production in cultured rat cardiac fibroblasts. *Basic Res Cardiol* **2004**, *99*, 257-263, doi:10.1007/s00395-004-0472-9.
46. Zhang, Y.; Alexander, P.B.; Wang, X.-F. TGF- β Family Signaling in the Control of Cell Proliferation and Survival. *Cold Spring Harb Perspect Biol* **2017**, *9*, a022145, doi:10.1101/cshperspect.a022145.
47. Ferrè, S.; Baldoli, E.; Leidi, M.; Maier, J.A.M. Magnesium deficiency promotes a pro-atherogenic phenotype in cultured human endothelial cells via activation of NFkB. *Biochimica et Biophysica Acta (BBA) - Molecular Basis of Disease* **2010**, *1802*, 952-958, doi:<https://doi.org/10.1016/j.bbadis.2010.06.016>.
48. Howard, A.B.; Alexander, R.W.; Taylor, W.R. Effects of magnesium on nitric oxide synthase activity in endothelial cells. *Am J Physiol* **1995**, *269*, C612-618, doi:10.1152/ajpcell.1995.269.3.C612.
49. Bernardini, D.; Nasulewic, A.; Mazur, A.; Maier, J.A. Magnesium and microvascular endothelial cells: a role in inflammation and angiogenesis. *Frontiers in bioscience : a journal and virtual library* **2005**, *10*, 1177-1182, doi:10.2741/1610.
50. Dulak, J.; Józkowicz, A. Nitric oxide and angiogenic activity of endothelial cells: direct or VEGF-dependent effect? *Cardiovascular Research* **2002**, *56*, 487-488, doi:10.1016/s0008-6363(02)00670-3.
51. Wolf, F.I.; Maier, J.A.; Nasulewicz, A.; Feillet-Coudray, C.; Simonacci, M.; Mazur, A.; Cittadini, A. Magnesium and neoplasia: from carcinogenesis to tumor growth and progression or treatment. *Archives of biochemistry and biophysics* **2007**, *458*, 24-32, doi:10.1016/j.abb.2006.02.016.
52. Kimura, H.; Weisz, A.; Kurashima, Y.; Hashimoto, K.; Ogura, T.; D'Acquisto, F.; Addeo, R.; Makuuchi, M.; Esumi, H. Hypoxia response element of the human vascular

References

- endothelial growth factor gene mediates transcriptional regulation by nitric oxide: control of hypoxia-inducible factor-1 activity by nitric oxide. *Blood* **2000**, *95*, 189-197.
53. Sugimoto, J.; Romani, A.M.; Valentin-Torres, A.M.; Luciano, A.A.; Ramirez Kitchen, C.M.; Funderburg, N.; Mesiano, S.; Bernstein, H.B. Magnesium decreases inflammatory cytokine production: a novel innate immunomodulatory mechanism. *J Immunol* **2012**, *188*, 6338-6346, doi:10.4049/jimmunol.1101765.
 54. Chaigne-Delalande, B.; Li, F.Y.; O'Connor, G.M.; Lukacs, M.J.; Jiang, P.; Zheng, L.; Shatzer, A.; Biancalana, M.; Pittaluga, S.; Matthews, H.F., et al. Mg²⁺ regulates cytotoxic functions of NK and CD8 T cells in chronic EBV infection through NKG2D. *Science* **2013**, *341*, 186-191, doi:10.1126/science.1240094.
 55. Zhang, X.F.; Park, J.H.; Choi, Y.J.; Kang, M.H.; Gurunathan, S.; Kim, J.H. Silver nanoparticles cause complications in pregnant mice. *International journal of nanomedicine* **2015**, *10*, 7057-7071, doi:10.2147/ijn.S95694.
 56. Lu, Z.; Rong, K.; Li, J.; Yang, H.; Chen, R. Size-dependent antibacterial activities of silver nanoparticles against oral anaerobic pathogenic bacteria. *J Mater Sci Mater Med* **2013**, *24*, 1465-1471, doi:10.1007/s10856-013-4894-5.
 57. Zhang, T.; Wang, L.; Chen, Q.; Chen, C. Cytotoxic potential of silver nanoparticles. *Yonsei Med J* **2014**, *55*, 283-291, doi:10.3349/ymj.2014.55.2.283.
 58. Zhan, D.; Fan, F.R.; Bard, A.J. The Kv channel blocker 4-aminopyridine enhances Ag⁺ uptake: a scanning electrochemical microscopy study of single living cells. *Proc Natl Acad Sci U S A* **2008**, *105*, 12118-12122, doi:10.1073/pnas.0805286105.
 59. Behra, R.; Sigg, L.; Clift, M.J.; Herzog, F.; Minghetti, M.; Johnston, B.; Petri-Fink, A.; Rothen-Rutishauser, B. Bioavailability of silver nanoparticles and ions: from a chemical and biochemical perspective. *J R Soc Interface* **2013**, *10*, 20130396, doi:10.1098/rsif.2013.0396.
 60. Asharani, P.V.; Hande, M.P.; Valiyaveetil, S. Anti-proliferative activity of silver nanoparticles. *BMC cell biology* **2009**, *10*, 65, doi:10.1186/1471-2121-10-65.
 61. Cameron, S.J.; Hosseini, F.; Willmore, W.G. A Current Overview of the Biological and Cellular Effects of Nanosilver. *International journal of molecular sciences* **2018**, *19*, 2030, doi:10.3390/ijms19072030.
 62. Chen, Y.; Wang, Z.; Xu, M.; Wang, X.; Liu, R.; Liu, Q.; Zhang, Z.; Xia, T.; Zhao, J.; Jiang, G., et al. Nanosilver Incurs an Adaptive Shunt of Energy Metabolism Mode to Glycolysis in Tumor and Nontumor Cells. *ACS Nano* **2014**, *8*, 5813-5825, doi:10.1021/nn500719m.
 63. Lin, J.; Huang, Z.; Wu, H.; Zhou, W.; Jin, P.; Wei, P.; Zhang, Y.; Zheng, F.; Zhang, J.; Xu, J., et al. Inhibition of autophagy enhances the anticancer activity of silver nanoparticles. *Autophagy* **2014**, *10*, 2006-2020, doi:10.4161/auto.36293.
 64. Griffiths, L.; Dachs, G.U.; Bicknell, R.; Harris, A.L.; Stratford, I.J. The influence of oxygen tension and pH on the expression of platelet-derived endothelial cell growth factor/thymidine phosphorylase in human breast tumor cells grown in vitro and in vivo. *Cancer Res* **1997**, *57*, 570-572.
 65. Bellocq, A.; Suberville, S.; Philippe, C.; Bertrand, F.; Perez, J.; Fouqueray, B.; Cherqui, G.; Baud, L. Low environmental pH is responsible for the induction of nitric-oxide synthase in macrophages. Evidence for involvement of nuclear factor-kappaB activation. *J Biol Chem* **1998**, *273*, 5086-5092, doi:10.1074/jbc.273.9.5086.
 66. Shi, Q.; Abbruzzese, J.L.; Huang, S.; Fidler, I.J.; Xiong, Q.; Xie, K. Constitutive and inducible interleukin 8 expression by hypoxia and acidosis renders human pancreatic cancer cells more tumorigenic and metastatic. *Clin Cancer Res* **1999**, *5*, 3711-3721.
 67. Hunt, T.K.; Aslam, R.S.; Beckert, S.; Wagner, S.; Ghani, Q.P.; Hussain, M.Z.; Roy, S.; Sen, C.K. Aerobically derived lactate stimulates revascularization and tissue repair via redox mechanisms. *Antioxid Redox Signal* **2007**, *9*, 1115-1124, doi:10.1089/ars.2007.1674.
 68. Kato, Y.; Lambert, C.A.; Colige, A.C.; Mineur, P.; Noël, A.; Frankenne, F.; Foidart, J.M.; Baba, M.; Hata, R.; Miyazaki, K., et al. Acidic extracellular pH induces matrix metalloproteinase-9 expression in mouse metastatic melanoma cells through the

- phospholipase D-mitogen-activated protein kinase signaling. *J Biol Chem* **2005**, *280*, 10938-10944, doi:10.1074/jbc.M411313200.
69. Kato, Y.; Ozawa, S.; Miyamoto, C.; Maehata, Y.; Suzuki, A.; Maeda, T.; Baba, Y. Acidic extracellular microenvironment and cancer. *Cancer Cell International* **2013**, *13*, 89, doi:10.1186/1475-2867-13-89.
 70. Ibrahim-Hashim, A.; Estrella, V. Acidosis and cancer: from mechanism to neutralization. *Cancer Metastasis Rev* **2019**, *38*, 149-155, doi:10.1007/s10555-019-09787-4.
 71. Severin, T.; Müller, B.; Giese, G.; Uhl, B.; Wolf, B.; Hauschildt, S.; Kreutz, W. pH-dependent LAK cell cytotoxicity. *Tumour biology : the journal of the International Society for Oncodevelopmental Biology and Medicine* **1994**, *15*, 304-310, doi:10.1159/000217905.
 72. Loeffler, D.A.; Juneau, P.L.; Heppner, G.H. Natural killer-cell activity under conditions reflective of tumor micro-environment. *Int J Cancer* **1991**, *48*, 895-899, doi:10.1002/ijc.2910480617.
 73. Redegeld, F.; Filippini, A.; Sitkovsky, M. Comparative studies of the cytotoxic T lymphocyte-mediated cytotoxicity and of extracellular ATP-induced cell lysis. Different requirements in extracellular Mg²⁺ and pH. *The Journal of Immunology* **1991**, *147*, 3638-3645.
 74. Bidani, A.; Wang, C.; Saggi, S.; Heming, T. Evidence for pH sensitivity of tumor necrosis factor- α release by alveolar macrophages. *Lung* **1998**, *176*, 111-121.
 75. Araki, A.; Inoue, T.; Cragoe, E.J., Jr.; Sendo, F. Na⁺/H⁺ exchange modulates rat neutrophil mediated tumor cytotoxicity. *Cancer Res* **1991**, *51*, 3212-3216.
 76. Nakagawara, A.; Nathan, C.F.; Cohn, Z.A. Hydrogen peroxide metabolism in human monocytes during differentiation in vitro. *J Clin Invest* **1981**, *68*, 1243-1252, doi:10.1172/jci110370.
 77. Adams, D.J.; Dewhirst, M.W.; Flowers, J.L.; Gamcsik, M.P.; Colvin, O.M.; Manikumar, G.; Wani, M.C.; Wall, M.E. Camptothecin analogues with enhanced antitumor activity at acidic pH. *Cancer Chemother Pharmacol* **2000**, *46*, 263-271, doi:10.1007/s002800000157.
 78. Vukovic, V.; Tannock, I.F. Influence of low pH on cytotoxicity of paclitaxel, mitoxantrone and topotecan. *Br J Cancer* **1997**, *75*, 1167-1172, doi:10.1038/bjc.1997.201.
 79. Lotz, C.; Kelleher, D.K.; Gassner, B.; Gekle, M.; Vaupel, P.; Thews, O. Role of the tumor microenvironment in the activity and expression of the p-glycoprotein in human colon carcinoma cells. *Oncol Rep* **2007**, *17*, 239-244.
 80. Thews, O.; Dillenburg, W.; Rösch, F.; Fellner, M. PET imaging of the impact of extracellular pH and MAP kinases on the p-glycoprotein (Pgp) activity. *Advances in experimental medicine and biology* **2013**, *765*, 279-286, doi:10.1007/978-1-4614-4989-8_39.
 81. Shiozaki, A.; Ichikawa, D.; Kosuga, T.; Marunaka, Y.; Otsuji, E. Regulation of osmolality for cancer treatment. *The Journal of Physiological Sciences* **2017**, *67*, 353-360, doi:10.1007/s12576-017-0528-x.
 82. Oates, J.R.; Maani, C.V. Death and Dying. In *StatPearls*, StatPearls Publishing
- Copyright © 2021, StatPearls Publishing LLC.: Treasure Island (FL), 2021.
83. White, M.C.; Holman, D.M.; Boehm, J.E.; Peipins, L.A.; Grossman, M.; Henley, S.J. Age and cancer risk: a potentially modifiable relationship. *American journal of preventive medicine* **2014**, *46*, S7-S15, doi:10.1016/j.amepre.2013.10.029.
 84. Cinar, D.; Tas, D. Cancer in the elderly. *North Clin Istanb* **2015**, *2*, 73-80, doi:10.14744/nci.2015.72691.
 85. Siegel, R.L.; Miller, K.D.; Jemal, A. Cancer statistics, 2018. *CA: a cancer journal for clinicians* **2018**, *68*, 7-30, doi:10.3322/caac.21442.
 86. Bertram, J.S. The molecular biology of cancer. *Molecular aspects of medicine* **2000**, *21*, 167-223, doi:10.1016/s0098-2997(00)00007-8.
 87. Cahill, D.P.; Kinzler, K.W.; Vogelstein, B.; Lengauer, C. Genetic instability and darwinian selection in tumours. *Trends Cell Biol* **1999**, *9*, M57-60.

References

88. Lynch, M. Evolution of the mutation rate. *Trends Genet* **2010**, *26*, 345-352, doi:10.1016/j.tig.2010.05.003.
89. Dagogo-Jack, I.; Shaw, A.T. Tumour heterogeneity and resistance to cancer therapies. *Nature reviews. Clinical oncology* **2018**, *15*, 81-94, doi:10.1038/nrclinonc.2017.166.
90. Siddiqui, M.; Rajkumar, S.V. The high cost of cancer drugs and what we can do about it. *Mayo Clinic proceedings* **2012**, *87*, 935-943, doi:10.1016/j.mayocp.2012.07.007.
91. Hanahan, D.; Weinberg, R.A. The hallmarks of cancer. *Cell* **2000**, *100*, 57-70, doi:10.1016/s0092-8674(00)81683-9.
92. Hanahan, D.; Weinberg, R.A. Hallmarks of cancer: the next generation. *Cell* **2011**, *144*, 646-674, doi:10.1016/j.cell.2011.02.013.
93. Rowley, J.D. A New Consistent Chromosomal Abnormality in Chronic Myelogenous Leukaemia identified by Quinacrine Fluorescence and Giemsa Staining. *Nature* **1973**, *243*, 290-293, doi:10.1038/243290a0.
94. Nakada, M.; Kita, D.; Watanabe, T.; Hayashi, Y.; Teng, L.; Pyko, I.; Hamada, J.-I. Aberrant Signaling Pathways in Glioma. *Cancers (Basel)* **2011**, *3*, 3242-3278, doi:10.3390/cancers3033242.
95. Davies, M.A.; Samuels, Y. Analysis of the genome to personalize therapy for melanoma. *Oncogene* **2010**, *29*, 5545-5555, doi:10.1038/onc.2010.323.
96. Yuan, T.L.; Cantley, L.C. PI3K pathway alterations in cancer: variations on a theme. *Oncogene* **2008**, *27*, 5497-5510, doi:10.1038/onc.2008.245.
97. Ahlquist, T.; Bottillo, I.; Danielsen, S.A.; Meling, G.I.; Rognum, T.O.; Lind, G.E.; Dallapiccola, B.; Lothe, R.A. RAS signaling in colorectal carcinomas through alteration of RAS, RAF, NF1, and/or RASSF1A. *Neoplasia (New York, N.Y.)* **2008**, *10*, 680-686, doi:10.1593/neo.08312.
98. Vander Heiden, M.G.; Cantley, L.C.; Thompson, C.B. Understanding the Warburg effect: the metabolic requirements of cell proliferation. *Science* **2009**, *324*, 1029-1033, doi:10.1126/science.1160809.
99. Kim, Y.; Roh, S.; Lawler, S.; Friedman, A. miR451 and AMPK Mutual Antagonism in Glioma Cell Migration and Proliferation: A Mathematical Model. *PLoS One* **2011**, *6*, e28293, doi:10.1371/journal.pone.0028293.
100. Warburg, O. On the origin of cancer cells. *Science* **1956**, *123*, 309-314, doi:10.1126/science.123.3191.309.
101. Weinhouse, S. The Warburg hypothesis fifty years later. *Zeitschrift fur Krebsforschung und klinische Onkologie. Cancer research and clinical oncology* **1976**, *87*, 115-126, doi:10.1007/bf00284370.
102. Fantin, V.R.; St-Pierre, J.; Leder, P. Attenuation of LDH-A expression uncovers a link between glycolysis, mitochondrial physiology, and tumor maintenance. *Cancer Cell* **2006**, *9*, 425-434, doi:10.1016/j.ccr.2006.04.023.
103. Moreno-Sánchez, R.; Rodríguez-Enríquez, S.; Marín-Hernández, A.; Saavedra, E. Energy metabolism in tumor cells. *Febs j* **2007**, *274*, 1393-1418, doi:10.1111/j.1742-4658.2007.05686.x.
104. Liberti, M.V.; Locasale, J.W. The Warburg Effect: How Does it Benefit Cancer Cells? *Trends in biochemical sciences* **2016**, *41*, 211-218, doi:10.1016/j.tibs.2015.12.001.
105. Locasale, J.W.; Cantley, L.C. Metabolic flux and the regulation of mammalian cell growth. *Cell metabolism* **2011**, *14*, 443-451, doi:10.1016/j.cmet.2011.07.014.
106. Pfeiffer, T.; Schuster, S.; Bonhoeffer, S. Cooperation and competition in the evolution of ATP-producing pathways. *Science* **2001**, *292*, 504-507, doi:10.1126/science.1058079.
107. Swietach, P.; Vaughan-Jones, R.D.; Harris, A.L.; Hulikova, A. The chemistry, physiology and pathology of pH in cancer. *Philos Trans R Soc Lond B Biol Sci* **2014**, *369*, 20130099, doi:10.1098/rstb.2013.0099.
108. Gottlieb, R.A.; Nordberg, J.; Skowronski, E.; Babior, B.M. Apoptosis induced in Jurkat cells by several agents is preceded by intracellular acidification. *Proc Natl Acad Sci U S A* **1996**, *93*, 654-658, doi:10.1073/pnas.93.2.654.

109. Lagadic-Gossmann, D.; Huc, L.; Lecureur, V. Alterations of intracellular pH homeostasis in apoptosis: origins and roles. *Cell Death Differ* **2004**, *11*, 953-961, doi:10.1038/sj.cdd.4401466.
110. Enerson, B.E.; Drewes, L.R. Molecular features, regulation, and function of monocarboxylate transporters: implications for drug delivery. *J Pharm Sci* **2003**, *92*, 1531-1544, doi:10.1002/jps.10389.
111. Hinton, A.; Sennoune, S.R.; Bond, S.; Fang, M.; Reuveni, M.; Sahagian, G.G.; Jay, D.; Martinez-Zaguilan, R.; Forgac, M. Function of a subunit isoforms of the V-ATPase in pH homeostasis and in vitro invasion of MDA-MB231 human breast cancer cells. *The Journal of biological chemistry* **2009**, *284*, 16400-16408, doi:10.1074/jbc.M901201200.
112. Pouysségur, J.; Mehta-Grigoriou, F. Redox regulation of the hypoxia-inducible factor. *Biological chemistry* **2006**, *387*, 1337-1346, doi:10.1515/bc.2006.167.
113. Damaghi, M.; Wojtkowiak, J.; Gillies, R. pH Sensing and Regulation in Cancer. *Frontiers in physiology* **2013**, *4*, 370, doi:10.3389/fphys.2013.00370.
114. Hashim, A.I.; Zhang, X.; Wojtkowiak, J.W.; Martinez, G.V.; Gillies, R.J. Imaging pH and metastasis. *NMR Biomed* **2011**, *24*, 582-591, doi:10.1002/nbm.1644.
115. Helmlinger, G.; Sckell, A.; Dellian, M.; Forbes, N.S.; Jain, R.K. Acid Production in Glycolysis-impaired Tumors Provides New Insights into Tumor Metabolism. *Clinical Cancer Research* **2002**, *8*, 1284.
116. Silva, A.S.; Yunes, J.A.; Gillies, R.J.; Gatenby, R.A. The potential role of systemic buffers in reducing intratumoral extracellular pH and acid-mediated invasion. *Cancer research* **2009**, *69*, 2677-2684, doi:10.1158/0008-5472.CAN-08-2394.
117. Rozhin, J.; Sameni, M.; Ziegler, G.; Sloane, B.F. Pericellular pH affects distribution and secretion of cathepsin B in malignant cells. *Cancer Res* **1994**, *54*, 6517-6525.
118. Xu, L.; Fidler, I.J. Acidic pH-induced elevation in interleukin 8 expression by human ovarian carcinoma cells. *Cancer Res* **2000**, *60*, 4610-4616.
119. Shi, Q.; Le, X.; Wang, B.; Abbruzzese, J.L.; Xiong, Q.; He, Y.; Xie, K. Regulation of vascular endothelial growth factor expression by acidosis in human cancer cells. *Oncogene* **2001**, *20*, 3751-3756, doi:10.1038/sj.onc.1204500.
120. Swietach, P.; Vaughan-Jones, R.D.; Harris, A.L. Regulation of tumor pH and the role of carbonic anhydrase 9. *Cancer Metastasis Rev* **2007**, *26*, 299-310, doi:10.1007/s10555-007-9064-0.
121. Hanahan, D.; Folkman, J. Patterns and emerging mechanisms of the angiogenic switch during tumorigenesis. *Cell* **1996**, *86*, 353-364, doi:10.1016/s0092-8674(00)80108-7.
122. Baeriswyl, V.; Christofori, G. The angiogenic switch in carcinogenesis. *Semin Cancer Biol* **2009**, *19*, 329-337, doi:10.1016/j.semcancer.2009.05.003.
123. North, S.; Moenner, M.; Bikfalvi, A. Recent developments in the regulation of the angiogenic switch by cellular stress factors in tumors. *Cancer Lett* **2005**, *218*, 1-14, doi:10.1016/j.canlet.2004.08.007.
124. McKeown, S.R. Defining normoxia, physoxia and hypoxia in tumours-implications for treatment response. *The British journal of radiology* **2014**, *87*, 20130676, doi:10.1259/bjr.20130676.
125. Carreau, A.; El Hafny-Rahbi, B.; Matejuk, A.; Grillon, C.; Kieda, C. Why is the partial oxygen pressure of human tissues a crucial parameter? Small molecules and hypoxia. *J Cell Mol Med* **2011**, *15*, 1239-1253, doi:10.1111/j.1582-4934.2011.01258.x.
126. Jensen, R.L.; Ragel, B.T.; Whang, K.; Gillespie, D. Inhibition of hypoxia inducible factor-1alpha (HIF-1alpha) decreases vascular endothelial growth factor (VEGF) secretion and tumor growth in malignant gliomas. *J Neurooncol* **2006**, *78*, 233-247, doi:10.1007/s11060-005-9103-z.
127. Kaelin, W.G. The von Hippel-Lindau tumor suppressor protein: roles in cancer and oxygen sensing. *Cold Spring Harb Symp Quant Biol* **2005**, *70*, 159-166, doi:10.1101/sqb.2005.70.001.
128. Liao, D.; Johnson, R.S. Hypoxia: a key regulator of angiogenesis in cancer. *Cancer Metastasis Rev* **2007**, *26*, 281-290, doi:10.1007/s10555-007-9066-y.
129. McDonald, D.M.; Choyke, P.L. Imaging of angiogenesis: from microscope to clinic. *Nature medicine* **2003**, *9*, 713-725.

References

130. Hida, K.; Ohga, N.; Hida, Y.; Shindoh, M. Significance of anti-angiogenic therapy in head and neck cancer—Heterogeneity of tumor endothelium. *Japanese Dental Science Review* **2010**, *46*, 26-32, doi:<https://doi.org/10.1016/j.jdsr.2009.10.001>.
131. Thomas, L. On immunosurveillance in human cancer. *Yale J Biol Med* **1982**, *55*, 329-333.
132. Burnet, F.M. The concept of immunological surveillance. *Progress in experimental tumor research* **1970**, *13*, 1-27, doi:10.1159/000386035.
133. Kim, R.; Emi, M.; Tanabe, K. Cancer immunoediting from immune surveillance to immune escape. *Immunology* **2007**, *121*, 1-14, doi:10.1111/j.1365-2567.2007.02587.x.
134. Snyder, A.; Makarov, V.; Merghoub, T.; Yuan, J.; Zaretsky, J.M.; Desrichard, A.; Walsh, L.A.; Postow, M.A.; Wong, P.; Ho, T.S., et al. Genetic basis for clinical response to CTLA-4 blockade in melanoma. *N Engl J Med* **2014**, *371*, 2189-2199, doi:10.1056/NEJMoa1406498.
135. Beatty, G.L.; Gladney, W.L. Immune escape mechanisms as a guide for cancer immunotherapy. *Clinical cancer research : an official journal of the American Association for Cancer Research* **2015**, *21*, 687-692, doi:10.1158/1078-0432.CCR-14-1860.
136. Bruno, A.; Ferlazzo, G.; Albin, A.; Noonan, D.M. A think tank of TINK/TANKs: tumor-infiltrating/tumor-associated natural killer cells in tumor progression and angiogenesis. *J Natl Cancer Inst* **2014**, *106*, dju200, doi:10.1093/jnci/dju200.
137. Tullius, B.P.; Setty, B.A.; Lee, D.A. Natural Killer Cell Immunotherapy for Osteosarcoma. *Advances in experimental medicine and biology* **2020**, *1257*, 141-154, doi:10.1007/978-3-030-43032-0_12.
138. Pegram, H.J.; Andrews, D.M.; Smyth, M.J.; Darcy, P.K.; Kershaw, M.H. Activating and inhibitory receptors of natural killer cells. *Immunology and cell biology* **2011**, *89*, 216-224, doi:10.1038/icb.2010.78.
139. Buddingh, E.P.; Schilham, M.W.; Ruslan, S.E.N.; Berghuis, D.; Szuhai, K.; Suurmond, J.; Tamini, A.H.M.; Gelderblom, H.; Egeler, R.M.; Serra, M., et al. Chemotherapy-resistant osteosarcoma is highly susceptible to IL-15-activated allogeneic and autologous NK cells. *Cancer Immunology, Immunotherapy* **2011**, *60*, 575-586, doi:10.1007/s00262-010-0965-3.
140. Trapani, J.A. Target cell apoptosis induced by cytotoxic T cells and natural killer cells involves synergy between the pore-forming protein, perforin, and the serine protease, granzyme B. *Australian and New Zealand journal of medicine* **1995**, *25*, 793-799, doi:10.1111/j.1445-5994.1995.tb02883.x.
141. Groth, A.; Klöss, S.; von Strandmann, E.P.; Koehl, U.; Koch, J. Mechanisms of tumor and viral immune escape from natural killer cell-mediated surveillance. *Journal of innate immunity* **2011**, *3*, 344-354, doi:10.1159/000327014.
142. Sarkar, S.; Germeraad, W.T.V.; Rouschop, K.M.A.; Steeghs, E.M.P.; van Gelder, M.; Bos, G.M.J.; Wieten, L. Hypoxia induced impairment of NK cell cytotoxicity against multiple myeloma can be overcome by IL-2 activation of the NK cells. *PLoS One* **2013**, *8*, e64835-e64835, doi:10.1371/journal.pone.0064835.
143. Bellone, G.; Aste-Amezaga, M.; Trinchieri, G.; Rodeck, U. Regulation of NK cell functions by TGF-beta 1. *The Journal of Immunology* **1995**, *155*, 1066-1073.
144. Chiang, A.C.; Massagué, J. Molecular basis of metastasis. *The New England journal of medicine* **2008**, *359*, 2814-2823, doi:10.1056/NEJMra0805239.
145. Talmadge, J.E.; Fidler, I.J. AACR centennial series: the biology of cancer metastasis: historical perspective. *Cancer research* **2010**, *70*, 5649-5669, doi:10.1158/0008-5472.CAN-10-1040.
146. Miller, M.C.; Doyle, G.V.; Terstappen, L.W. Significance of Circulating Tumor Cells Detected by the CellSearch System in Patients with Metastatic Breast Colorectal and Prostate Cancer. *Journal of oncology* **2010**, *2010*, 617421, doi:10.1155/2010/617421.
147. Pasqualini, R.; Ruoslahti, E. Organ targeting in vivo using phage display peptide libraries. *Nature* **1996**, *380*, 364-366, doi:10.1038/380364a0.
148. San Juan, B.P.; Garcia-Leon, M.J.; Rangel, L.; Goetz, J.G.; Chaffer, C.L. The Complexities of Metastasis. *Cancers (Basel)* **2019**, *11*, doi:10.3390/cancers11101575.

149. Paget, S. THE DISTRIBUTION OF SECONDARY GROWTHS IN CANCER OF THE BREAST. *The Lancet* **1889**, 133, 571-573, doi:[https://doi.org/10.1016/S0140-6736\(00\)49915-0](https://doi.org/10.1016/S0140-6736(00)49915-0).
150. Vogelstein, B.; Papadopoulos, N.; Velculescu, V.E.; Zhou, S.; Diaz, L.A., Jr.; Kinzler, K.W. Cancer genome landscapes. *Science* **2013**, 339, 1546-1558, doi:10.1126/science.1235122.
151. McDonald, O.G.; Li, X.; Saunders, T.; Tryggvadottir, R.; Mentch, S.J.; Warmoes, M.O.; Word, A.E.; Carrer, A.; Salz, T.H.; Natsume, S., et al. Epigenomic reprogramming during pancreatic cancer progression links anabolic glucose metabolism to distant metastasis. *Nat Genet* **2017**, 49, 367-376, doi:10.1038/ng.3753.
152. Aytes, A.; Giacobbe, A.; Mitrofanova, A.; Ruggero, K.; Cyrta, J.; Arriaga, J.; Palomero, L.; Farran-Matas, S.; Rubin, M.A.; Shen, M.M., et al. NSD2 is a conserved driver of metastatic prostate cancer progression. *Nat Commun* **2018**, 9, 5201, doi:10.1038/s41467-018-07511-4.
153. Jiang, L.; Nick, A.M.; Sood, A.K. Fundamental Principles of Cancer Biology: Does it have relevance to the perioperative period? *Current anesthesiology reports* **2015**, 5, 250-256, doi:10.1007/s40140-015-0122-9.
154. Roma-Rodrigues, C.; Pombo, I.; Raposo, L.; Pedrosa, P.; Fernandes, A.R.; Baptista, P.V. Nanotheranostics Targeting the Tumor Microenvironment. *Frontiers in Bioengineering and Biotechnology* **2019**, 7, doi:10.3389/fbioe.2019.00197.
155. Cirri, P.; Chiarugi, P. Cancer-associated-fibroblasts and tumour cells: a diabolic liaison driving cancer progression. *Cancer Metastasis Rev* **2012**, 31, 195-208, doi:10.1007/s10555-011-9340-x.
156. Li, H.; Fan, X.; Houghton, J. Tumor microenvironment: the role of the tumor stroma in cancer. *J Cell Biochem* **2007**, 101, 805-815, doi:10.1002/jcb.21159.
157. Alizadeh, D.; Larmonier, N. Chemotherapeutic targeting of cancer-induced immunosuppressive cells. *Cancer Res* **2014**, 74, 2663-2668, doi:10.1158/0008-5472.Can-14-0301.
158. DeNardo, D.G.; Brennan, D.J.; Rexhepaj, E.; Ruffell, B.; Shiao, S.L.; Madden, S.F.; Gallagher, W.M.; Wadhvani, N.; Keil, S.D.; Junaid, S.A., et al. Leukocyte complexity predicts breast cancer survival and functionally regulates response to chemotherapy. *Cancer discovery* **2011**, 1, 54-67, doi:10.1158/2159-8274.Cd-10-0028.
159. Chouaib, S.; Kieda, C.; Benlalam, H.; Noman, M.Z.; Mami-Chouaib, F.; Rüegg, C. Endothelial cells as key determinants of the tumor microenvironment: interaction with tumor cells, extracellular matrix and immune killer cells. *Critical reviews in immunology* **2010**, 30, 529-545, doi:10.1615/critrevimmunol.v30.i6.30.
160. Morelli, C.; Barbanti-Brodano, G.; Ciannilli, A.; Campioni, K.; Boriani, S.; Tognon, M. Cell morphology, markers, spreading, and proliferation on orthopaedic biomaterials. An innovative cellular model for the "in vitro" study. *Journal of biomedical materials research. Part A* **2007**, 83, 178-183, doi:10.1002/jbm.a.31262.
161. Xu, L.; Willumeit-Römer, R.; Luthringer-Feyerabend, B.J.C. Effect of magnesium-degradation products and hypoxia on the angiogenesis of human umbilical vein endothelial cells. *Acta Biomater* **2019**, 98, 269-283, doi:10.1016/j.actbio.2019.02.018.
162. 72(2004), A.G.-. Standard Practice for Laboratory Immersion Corrosion Testing of Metals. In *ASTM International, West Conshohocken, PA*, 2004; p 8.
163. Garca, R.; P, A. Atomic Absorption Spectrometry (AAS). In *Atomic Absorption Spectroscopy*, 2012; 10.5772/25925.
164. Moldovan, M. Atomic Absorption Spectrometry—Flame☆. In *Encyclopedia of Analytical Science (Third Edition)*, Worsfold, P., Poole, C., Townshend, A., Miró, M., Eds. Academic Press: Oxford, 2019; <https://doi.org/10.1016/B978-0-12-409547-2.00022-6pp>. 129-136.
165. Wilschefski, S.C.; Baxter, M.R. Inductively Coupled Plasma Mass Spectrometry: Introduction to Analytical Aspects. *Clin Biochem Rev* **2019**, 40, 115-133, doi:10.33176/AACB-19-00024.
166. El-Sharkaway, A. Calculate the Corrected Total Cell Fluorescence (CTCF). *Calculate the Corrected Total Cell Fluorescence (CTCF)* **2016**.

References

167. Patel, S.; Miao, J.H.; Yetiskul, E.; Anokhin, A.; Majmundar, S.H. Physiology, Carbon Dioxide Retention. In *StatPearls*, Treasure Island (FL), 2021.
168. Benner, A.; Lewallen, N.; Sharma, S. Physiology, Carbon Dioxide Response Curve. In *StatPearls*, Treasure Island (FL), 2021.
169. Hulkower, K.I.; Herber, R.L. Cell migration and invasion assays as tools for drug discovery. *Pharmaceutics* **2011**, *3*, 107-124, doi:10.3390/pharmaceutics3010107.
170. Xu, L.; Willumeit-Romer, R.; Luthringer-Feyerabend, B.J.C. Effect of magnesium-degradation products and hypoxia on the angiogenesis of human umbilical vein endothelial cells. *Acta Biomater* **2019**, *98*, 269-283, doi:10.1016/j.actbio.2019.02.018.
171. Globig, P.; Willumeit-Romer, R.; Martini, F.; Mazzoni, E.; Luthringer-Feyerabend, B.J.C. Optimizing an Osteosarcoma-Fibroblast Coculture Model to Study Antitumoral Activity of Magnesium-Based Biomaterials. *Int J Mol Sci* **2020**, *21*, doi:10.3390/ijms21145099.
172. Salvatore, V.; Focaroli, S.; Teti, G.; Mazzotti, A.; Falconi, M. Changes in the gene expression of co-cultured human fibroblast cells and osteosarcoma cells: the role of microenvironment. *Oncotarget* **2015**, *6*, 28988-28998, doi:10.18632/oncotarget.4902.
173. Martinez-Outschoorn, U.E.; Balliet, R.M.; Rivadeneira, D.B.; Chiavarina, B.; Pavlides, S.; Wang, C.; Whitaker-Menezes, D.; Daumer, K.M.; Lin, Z.; Witkiewicz, A.K., et al. Oxidative stress in cancer associated fibroblasts drives tumor-stroma co-evolution: A new paradigm for understanding tumor metabolism, the field effect and genomic instability in cancer cells. *Cell Cycle* **2010**, *9*, 3256-3276, doi:10.4161/cc.9.16.12553.
174. Angelucci, C.; Maulucci, G.; Lama, G.; Proietti, G.; Colabianchi, A.; Papi, M.; Maiorana, A.; De Spirito, M.; Micera, A.; Balzamino, O.B., et al. Epithelial-Stromal Interactions in Human Breast Cancer: Effects on Adhesion, Plasma Membrane Fluidity and Migration Speed and Directness. *PLoS One* **2012**, *7*, e50804, doi:10.1371/journal.pone.0050804.
175. Fujiwara, M.; Kanayama, K.; Hirokawa, Y.S.; Shiraishi, T. ASF-4-1 fibroblast-rich culture increases chemoresistance and mTOR expression of pancreatic cancer BxPC-3 cells at the invasive front in vitro, and promotes tumor growth and invasion in vivo. *Oncol Lett* **2016**, *11*, 2773-2779, doi:10.3892/ol.2016.4289.
176. Kuen, J.; Darowski, D.; Kluge, T.; Majety, M. Pancreatic cancer cell/fibroblast co-culture induces M2 like macrophages that influence therapeutic response in a 3D model. *PLoS One* **2017**, *12*, e0182039-e0182039, doi:10.1371/journal.pone.0182039.
177. Burmester, A.; Luthringer, B.; Willumeit, R.; Feyerabend, F. Comparison of the reaction of bone-derived cells to enhanced MgCl₂-salt concentrations. *Biomater* **2014**, *4*, e967616, doi:10.4161/21592527.2014.967616.
178. Burmester, A.; Willumeit-Romer, R.; Feyerabend, F. Behavior of bone cells in contact with magnesium implant material. *J Biomed Mater Res B Appl Biomater* **2017**, *105*, 165-179, doi:10.1002/jbm.b.33542.
179. Czekanska, E.M.; Stoddart, M.J.; Richards, R.G.; Hayes, J.S. In search of an osteoblast cell model for in vitro research. *Eur Cell Mater* **2012**, *24*, 1-17, doi:10.22203/ecm.v024a01.
180. Czekanska, E.M.; Stoddart, M.J.; Ralphs, J.R.; Richards, R.G.; Hayes, J.S. A phenotypic comparison of osteoblast cell lines versus human primary osteoblasts for biomaterials testing. *Journal of biomedical materials research. Part A* **2014**, *102*, 2636-2643, doi:10.1002/jbm.a.34937.
181. Rodan, S.B.; Imai, Y.; Thiede, M.A.; Wesolowski, G.; Thompson, D.; Bar-Shavit, Z.; Shull, S.; Mann, K.; Rodan, G.A. Characterization of a human osteosarcoma cell line (Saos-2) with osteoblastic properties. *Cancer Res* **1987**, *47*, 4961-4966.
182. Bilbe, G.; Roberts, E.; Birch, M.; Evans, D.B. PCR phenotyping of cytokines, growth factors and their receptors and bone matrix proteins in human osteoblast-like cell lines. *Bone* **1996**, *19*, 437-445, doi:[https://doi.org/10.1016/S8756-3282\(96\)00254-2](https://doi.org/10.1016/S8756-3282(96)00254-2).
183. Kalluri, R.; Zeisberg, M. Fibroblasts in cancer. *Nature Reviews Cancer* **2006**, *6*, 392-401, doi:10.1038/nrc1877.

184. Kannan, M.B.; Yamamoto, A.; Khakbaz, H. Influence of living cells (L929) on the biodegradation of magnesium-calcium alloy. *Colloids Surf B Biointerfaces* **2015**, *126*, 603-606, doi:10.1016/j.colsurfb.2015.01.015.
185. Brooks, E.K.; Tobias, M.E.; Yang, S.; Bone, L.B.; Ehrensberger, M.T. Influence of MC3T3-E1 preosteoblast culture on the corrosion of a T6-treated AZ91 alloy. *Journal of Biomedical Materials Research Part B: Applied Biomaterials* **2016**, *104*, 253-262, doi:<https://doi.org/10.1002/jbm.b.33378>.
186. Zhang, J.; Hiromoto, S.; Yamazaki, T.; Niu, J.; Huang, H.; Jia, G.; Li, H.; Ding, W.; Yuan, G. Effect of macrophages on in vitro corrosion behavior of magnesium alloy. *Journal of Biomedical Materials Research Part A* **2016**, *104*, 2476-2487, doi:<https://doi.org/10.1002/jbm.a.35788>.
187. Wagener, V.; Schilling, A.; Mainka, A.; Hennig, D.; Gerum, R.; Kelch, M.L.; Keim, S.; Fabry, B.; Virtanen, S. Cell Adhesion on Surface-Functionalized Magnesium. *ACS Appl Mater Interfaces* **2016**, *8*, 11998-12006, doi:10.1021/acsami.6b01747.
188. Seuss, F.; Seuss, S.; Turhan, M.C.; Fabry, B.; Virtanen, S. Corrosion of Mg alloy AZ91D in the presence of living cells. *Journal of Biomedical Materials Research Part B: Applied Biomaterials* **2011**, *99B*, 276-281, doi:10.1002/jbm.b.31896.
189. Ahmad Agha, N.; Willumeit-Römer, R.; Laipple, D.; Luthringer, B.; Feyerabend, F. The Degradation Interface of Magnesium Based Alloys in Direct Contact with Human Primary Osteoblast Cells. *PLoS One* **2016**, *11*, e0157874, doi:10.1371/journal.pone.0157874.
190. Wong, H.M.; Yeung, K.W.K.; Lam, K.O.; Tam, V.; Chu, P.K.; Luk, K.D.K.; Cheung, K.M.C. A biodegradable polymer-based coating to control the performance of magnesium alloy orthopaedic implants. *Biomaterials* **2010**, *31*, 2084-2096, doi:<https://doi.org/10.1016/j.biomaterials.2009.11.111>.
191. Keim, S.; Brunner, J.G.; Fabry, B.; Virtanen, S. Control of magnesium corrosion and biocompatibility with biomimetic coatings. *J Biomed Mater Res B Appl Biomater* **2011**, *96*, 84-90, doi:10.1002/jbm.b.31742.
192. Jo, J.-H.; Kang, B.-G.; Shin, K.-S.; Kim, H.-E.; Hahn, B.-D.; Park, D.-S.; Koh, Y.-H. Hydroxyapatite coating on magnesium with MgF₂ interlayer for enhanced corrosion resistance and biocompatibility. *Journal of Materials Science: Materials in Medicine* **2011**, *22*, 2437-2447, doi:10.1007/s10856-011-4431-3.
193. Lu, P.; Cao, L.; Liu, Y.; Xu, X.; Wu, X. Evaluation of magnesium ions release, biocorrosion, and hemocompatibility of MAO/PLLA-modified magnesium alloy WE42. *J Biomed Mater Res B Appl Biomater* **2011**, *96*, 101-109, doi:10.1002/jbm.b.31744.
194. Gu, X.N.; Li, N.; Zheng, Y.F.; Ruan, L. In vitro degradation performance and biological response of a Mg-Zn-Zr alloy. *Materials Science and Engineering: B* **2011**, *176*, 1778-1784, doi:<https://doi.org/10.1016/j.mseb.2011.05.032>.
195. Huan, Z.G.; Leeflang, M.A.; Zhou, J.; Fratila-Apachitei, L.E.; Duszczyk, J. In vitro degradation behavior and cytocompatibility of Mg-Zn-Zr alloys. *J Mater Sci Mater Med* **2010**, *21*, 2623-2635, doi:10.1007/s10856-010-4111-8.
196. Liu, Z.; Schade, R.; Luthringer, B.; Hort, N.; Rothe, H.; Muller, S.; Liefelth, K.; Willumeit-Römer, R.; Feyerabend, F. Influence of the Microstructure and Silver Content on Degradation, Cytocompatibility, and Antibacterial Properties of Magnesium-Silver Alloys In Vitro. *Oxid Med Cell Longev* **2017**, *2017*, 8091265, doi:10.1155/2017/8091265.
197. Gonzalez, J.; Hou, R.Q.; Nidadavolu, E.P.S.; Willumeit-Römer, R.; Feyerabend, F. Magnesium degradation under physiological conditions - Best practice. *Bioact Mater* **2018**, *3*, 174-185, doi:10.1016/j.bioactmat.2018.01.003.
198. Fischer, J.; Prosenc, M.H.; Wolff, M.; Hort, N.; Willumeit, R.; Feyerabend, F. Interference of magnesium corrosion with tetrazolium-based cytotoxicity assays. *Acta Biomater* **2010**, *6*, 1813-1823, doi:10.1016/j.actbio.2009.10.020.
199. Kumari, S.; Badana, A.K.; G, M.M.; G, S.; Malla, R. Reactive Oxygen Species: A Key Constituent in Cancer Survival. *Biomark Insights* **2018**, *13*, 1177271918755391, doi:10.1177/1177271918755391.

References

200. Raza, M.H.; Siraj, S.; Arshad, A.; Waheed, U.; Aldakheel, F.; Alduraywish, S.; Arshad, M. ROS-modulated therapeutic approaches in cancer treatment. *J Cancer Res Clin Oncol* **2017**, *143*, 1789-1809, doi:10.1007/s00432-017-2464-9.
201. Diao, Q.X.; Zhang, J.Z.; Zhao, T.; Xue, F.; Gao, F.; Ma, S.M.; Wang, Y. Vitamin E promotes breast cancer cell proliferation by reducing ROS production and p53 expression. *Eur Rev Med Pharmacol Sci* **2016**, *20*, 2710-2717.
202. Urruticoechea, A.; Smith, I.E.; Dowsett, M. Proliferation marker Ki-67 in early breast cancer. *J Clin Oncol* **2005**, *23*, 7212-7220, doi:10.1200/JCO.2005.07.501.
203. Soares, A.; Govender, L.; Hughes, J.; Mavakla, W.; de Kock, M.; Barnard, C.; Pienaar, B.; Janse van Rensburg, E.; Jacobs, G.; Khomba, G., et al. Novel application of Ki67 to quantify antigen-specific in vitro lymphoproliferation. *Journal of immunological methods* **2010**, *362*, 43-50, doi:10.1016/j.jim.2010.08.007.
204. Perou, C.M.; Jeffrey, S.S.; van de Rijn, M.; Rees, C.A.; Eisen, M.B.; Ross, D.T.; Pergamenschikov, A.; Williams, C.F.; Zhu, S.X.; Lee, J.C., et al. Distinctive gene expression patterns in human mammary epithelial cells and breast cancers. *Proc Natl Acad Sci U S A* **1999**, *96*, 9212-9217, doi:10.1073/pnas.96.16.9212.
205. Nishimura, R.; Osako, T.; Okumura, Y.; Hayashi, M.; Toyozumi, Y.; Arima, N. Ki-67 as a prognostic marker according to breast cancer subtype and a predictor of recurrence time in primary breast cancer. *Exp Ther Med* **2010**, *1*, 747-754, doi:10.3892/etm.2010.133.
206. Zan, R.; Ji, W.; Qiao, S.; Wu, H.; Wang, W.; Ji, T.; Yang, B.; Zhang, S.; Luo, C.; Song, Y., et al. Biodegradable magnesium implants: a potential scaffold for bone tumor patients. *Science China Materials* **2021**, *64*, 1007-1020, doi:10.1007/s40843-020-1509-2.
207. Aguirre-Ghiso, J.A. Models, mechanisms and clinical evidence for cancer dormancy. *Nature reviews. Cancer* **2007**, *7*, 834-846, doi:10.1038/nrc2256.
208. Sang, L.; Collier, H.A.; Roberts, J.M. Control of the reversibility of cellular quiescence by the transcriptional repressor HES1. *Science* **2008**, *321*, 1095-1100, doi:10.1126/science.1155998.
209. Padró, M.; Louie, R.J.; Lananna, B.V.; Krieg, A.J.; Timmerman, L.A.; Chan, D.A. Genome-independent hypoxic repression of estrogen receptor alpha in breast cancer cells. *BMC Cancer* **2017**, *17*, 203, doi:10.1186/s12885-017-3140-9.
210. Lee, H.R.; Leslie, F.; Azarin, S.M. A facile in vitro platform to study cancer cell dormancy under hypoxic microenvironments using CoCl₂. *J Biol Eng* **2018**, *12*, 12, doi:10.1186/s13036-018-0106-7.
211. Bragado, P.; Sosa, M.S.; Keely, P.; Condeelis, J.; Aguirre-Ghiso, J.A. Microenvironments dictating tumor cell dormancy. *Recent results in cancer research. Fortschritte der Krebsforschung. Progres dans les recherches sur le cancer* **2012**, *195*, 25-39, doi:10.1007/978-3-642-28160-0_3.
212. Naumov, G.N.; Townson, J.L.; MacDonald, I.C.; Wilson, S.M.; Bramwell, V.H.; Groom, A.C.; Chambers, A.F. Ineffectiveness of doxorubicin treatment on solitary dormant mammary carcinoma cells or late-developing metastases. *Breast Cancer Res Treat* **2003**, *82*, 199-206, doi:10.1023/B:BREA.0000004377.12288.3c.
213. Bi, M.; Naczki, C.; Koritzinsky, M.; Fels, D.; Blais, J.; Hu, N.; Harding, H.; Novoa, I.; Varia, M.; Raleigh, J., et al. ER stress-regulated translation increases tolerance to extreme hypoxia and promotes tumor growth. *EMBO J* **2005**, *24*, 3470-3481, doi:10.1038/sj.emboj.7600777.
214. Dandekar, A.; Mendez, R.; Zhang, K. Cross Talk Between ER Stress, Oxidative Stress, and Inflammation in Health and Disease. In *Stress Responses: Methods and Protocols*, Osowski, C.M., Ed. Springer New York: New York, NY, 2015; 10.1007/978-1-4939-2522-3_15pp. 205-214.
215. Li, X.; Zhang, K.; Li, Z. Unfolded protein response in cancer: the physician's perspective. *J Hematol Oncol* **2011**, *4*, 8-8, doi:10.1186/1756-8722-4-8.
216. Harding, H.P.; Zhang, Y.; Ron, D. Protein translation and folding are coupled by an endoplasmic-reticulum-resident kinase. *Nature* **1999**, *397*, 271-274, doi:10.1038/16729.

217. Szegezdi, E.; Logue, S.E.; Gorman, A.M.; Samali, A. Mediators of endoplasmic reticulum stress-induced apoptosis. *EMBO reports* **2006**, *7*, 880-885, doi:10.1038/sj.embor.7400779.
218. Datto, M.B.; Li, Y.; Panus, J.F.; Howe, D.J.; Xiong, Y.; Wang, X.F. Transforming growth factor beta induces the cyclin-dependent kinase inhibitor p21 through a p53-independent mechanism. *Proceedings of the National Academy of Sciences of the United States of America* **1995**, *92*, 5545-5549, doi:10.1073/pnas.92.12.5545.
219. Derynck, R.; Akhurst, R.J.; Balmain, A. TGF- β signaling in tumor suppression and cancer progression. *Nature Genetics* **2001**, *29*, 117-129, doi:10.1038/ng1001-117.
220. Spencer, S.L.; Cappell, S.D.; Tsai, F.-C.; Overton, K.W.; Wang, C.L.; Meyer, T. The proliferation-quiescence decision is controlled by a bifurcation in CDK2 activity at mitotic exit. *Cell* **2013**, *155*, 369-383, doi:10.1016/j.cell.2013.08.062.
221. Luppi, F.; Longo, A.M.; de Boer, W.I.; Rabe, K.F.; Hiemstra, P.S. Interleukin-8 stimulates cell proliferation in non-small cell lung cancer through epidermal growth factor receptor transactivation. *Lung Cancer* **2007**, *56*, 25-33, doi:10.1016/j.lungcan.2006.11.014.
222. Ning, Y.; Manegold, P.C.; Hong, Y.K.; Zhang, W.; Pohl, A.; Lurje, G.; Winder, T.; Yang, D.; LaBonte, M.J.; Wilson, P.M., et al. Interleukin-8 is associated with proliferation, migration, angiogenesis and chemosensitivity in vitro and in vivo in colon cancer cell line models. *International journal of cancer* **2011**, *128*, 2038-2049, doi:10.1002/ijc.25562.
223. Xu, L.; Fidler, I.J. Interleukin 8: an autocrine growth factor for human ovarian cancer. *Oncol Res* **2000**, *12*, 97-106, doi:10.3727/096504001108747567.
224. Mussano, F.; Genova, T.; Corsalini, M.; Schierano, G.; Pettini, F.; Di Venere, D.; Carossa, S. Cytokine, Chemokine, and Growth Factor Profile Characterization of Undifferentiated and Osteoinduced Human Adipose-Derived Stem Cells. *Stem Cells International* **2017**, *2017*, 6202783, doi:10.1155/2017/6202783.
225. Yeh, A.C.; Ramaswamy, S. Mechanisms of Cancer Cell Dormancy--Another Hallmark of Cancer? *Cancer Res* **2015**, *75*, 5014-5022, doi:10.1158/0008-5472.can-15-1370.
226. Lamaka, S.V.; Gonzalez, J.; Mei, D.; Feyerabend, F.; Willumeit-Römer, R.; Zheludkevich, M.L. Local pH and Its Evolution Near Mg Alloy Surfaces Exposed to Simulated Body Fluids. *Advanced Materials Interfaces* **2018**, *5*, 1800169, doi:10.1002/admi.201800169.
227. Yun, Y.; Dong, Z.; Tan, Z.; Schulz, M.J. Development of an electrode cell impedance method to measure osteoblast cell activity in magnesium-conditioned media. *Anal Bioanal Chem* **2010**, *396*, 3009-3015, doi:10.1007/s00216-010-3521-2.
228. Ceccarini, C.; Eagle, H. pH as a determinant of cellular growth and contact inhibition. *Proceedings of the National Academy of Sciences of the United States of America* **1971**, *68*, 229-233, doi:10.1073/pnas.68.1.229.
229. Neri, D.; Supuran, C.T. Interfering with pH regulation in tumours as a therapeutic strategy. *Nature Reviews Drug Discovery* **2011**, *10*, 767-777, doi:10.1038/nrd3554.
230. Tiryaki, G.R.; Atterbom, H.A. The effects of sodium bicarbonate and sodium citrate on 600 m running time of trained females. *J Sports Med Phys Fitness* **1995**, *35*, 194-198.
231. White, C.R.; Seymour, R.S. Allometric scaling of mammalian metabolism. *Journal of Experimental Biology* **2005**, *208*, 1611, doi:10.1242/jeb.01501.
232. McCarty, M.F.; Whitaker, J. Manipulating tumor acidification as a cancer treatment strategy. *Alternative medicine review : a journal of clinical therapeutic* **2010**, *15*, 264-272.
233. Chao, M.; Wu, H.; Jin, K.; Li, B.; Wu, J.; Zhang, G.; Yang, G.; Hu, X. A nonrandomized cohort and a randomized study of local control of large hepatocarcinoma by targeting intratumoral lactic acidosis. *Elife* **2016**, *5*, doi:10.7554/eLife.15691.
234. Ludwig, M.G.; Vanek, M.; Guerini, D.; Gasser, J.A.; Jones, C.E.; Junker, U.; Hofstetter, H.; Wolf, R.M.; Seuwen, K. Proton-sensing G-protein-coupled receptors. *Nature* **2003**, *425*, 93-98, doi:10.1038/nature01905.

References

235. Wiley, S.Z.; Sriram, K.; Salmerón, C.; Insel, P.A. GPR68: An Emerging Drug Target in Cancer. *International journal of molecular sciences* **2019**, *20*, 559, doi:10.3390/ijms20030559.
236. Huang, W.C.; Swietach, P.; Vaughan-Jones, R.D.; Ansoorge, O.; Glitsch, M.D. Extracellular acidification elicits spatially and temporally distinct Ca²⁺ signals. *Curr Biol* **2008**, *18*, 781-785, doi:10.1016/j.cub.2008.04.049.
237. Pilon-Thomas, S.; Kodumudi, K.N.; El-Kenawi, A.E.; Russell, S.; Weber, A.M.; Luddy, K.; Damaghi, M.; Wojtkowiak, J.W.; Mulé, J.J.; Ibrahim-Hashim, A., et al. Neutralization of Tumor Acidity Improves Antitumor Responses to Immunotherapy. *Cancer research* **2016**, *76*, 1381-1390, doi:10.1158/0008-5472.CAN-15-1743.
238. Wu, Y.; He, G.; Zhang, Y.; Liu, Y.; Li, M.; Wang, X.; Li, N.; Li, K.; Zheng, G.; Zheng, Y., et al. Unique antitumor property of the Mg-Ca-Sr alloys with addition of Zn. *Sci Rep* **2016**, *6*, 21736, doi:10.1038/srep21736.
239. Fischer, J.; Pröfrock, D.; Hort, N.; Willumeit, R.; Feyerabend, F. Improved cytotoxicity testing of magnesium materials. *Materials Science and Engineering: B* **2011**, *176*, 830-834, doi:<https://doi.org/10.1016/j.mseb.2011.04.008>.
240. Wang, J.; Witte, F.; Xi, T.; Zheng, Y.; Yang, K.; Yang, Y.; Zhao, D.; Meng, J.; Li, Y.; Li, W., et al. Recommendation for modifying current cytotoxicity testing standards for biodegradable magnesium-based materials. *Acta Biomater* **2015**, *21*, 237-249, doi:10.1016/j.actbio.2015.04.011.
241. Kunimasa, K.; Goto, T. Immunosurveillance and Immunoediting of Lung Cancer: Current Perspectives and Challenges. *International Journal of Molecular Sciences* **2020**, *21*, 597.
242. Howe, M.K.; Dowdell, K.; Roy, A.; Niemela, J.E.; Wilson, W.; McElwee, J.J.; Hughes, J.D.; Cohen, J.I. Magnesium Restores Activity to Peripheral Blood Cells in a Patient With Functionally Impaired Interleukin-2-Inducible T Cell Kinase. *Front Immunol* **2019**, *10*, 2000, doi:10.3389/fimmu.2019.02000.
243. Chaigne-Delalande, B.; Li, F.-Y.; O'Connor, G.M.; Lukacs, M.J.; Jiang, P.; Zheng, L.; Shatzer, A.; Biancalana, M.; Pittaluga, S.; Matthews, H.F., et al. Mg²⁺ regulates cytotoxic functions of NK and CD8 T cells in chronic EBV infection through NKG2D. *Science (New York, N.Y.)* **2013**, *341*, 186-191, doi:10.1126/science.1240094.
244. Wang, J.; Matosevic, S. Functional and metabolic targeting of natural killer cells to solid tumors. *Cellular oncology (Dordrecht)* **2020**, *43*, 577-600, doi:10.1007/s13402-020-00523-7.
245. Keating, S.E.; Zaiatz-Bittencourt, V.; Loftus, R.M.; Keane, C.; Brennan, K.; Finlay, D.K.; Gardiner, C.M. Metabolic Reprogramming Supports IFN- γ Production by CD56bright NK Cells. *J Immunol* **2016**, *196*, 2552-2560, doi:10.4049/jimmunol.1501783.
246. Gong, J.H.; Maki, G.; Klingemann, H.G. Characterization of a human cell line (NK-92) with phenotypical and functional characteristics of activated natural killer cells. *Leukemia* **1994**, *8*, 652-658.
247. Smyth, M.J.; Swann, J.; Kelly, J.M.; Cretney, E.; Yokoyama, W.M.; Diefenbach, A.; Sayers, T.J.; Hayakawa, Y. NKG2D recognition and perforin effector function mediate effective cytokine immunotherapy of cancer. *The Journal of experimental medicine* **2004**, *200*, 1325-1335, doi:10.1084/jem.20041522.
248. Diao, B.; Huang, X.; Guo, S.; Yang, C.; Liu, G.; Chen, Y.; Wu, Y. MAGT1-mediated disturbance of Mg²⁺ homeostasis lead to exhausted of HBV-infected NK and CD8⁺ T cells. *Scientific Reports* **2017**, *7*, 13594, doi:10.1038/s41598-017-11522-4.
249. Jin, H.-s.; Choi, D.-s.; Ko, M.; Kim, D.; Lee, D.-h.; Lee, S.; Lee, A.Y.; Kang, S.G.; Kim, S.H.; Jung, Y., et al. Extracellular pH modulating injectable gel for enhancing immune checkpoint inhibitor therapy. *Journal of Controlled Release* **2019**, *315*, 65-75, doi:<https://doi.org/10.1016/j.jconrel.2019.10.041>.
250. Damgaci, S.; Ibrahim-Hashim, A.; Enriquez-Navas, P.M.; Pilon-Thomas, S.; Guvenis, A.; Gillies, R.J. Hypoxia and acidosis: immune suppressors and therapeutic targets. *Immunology* **2018**, *154*, 354-362, doi:10.1111/imm.12917.
251. Pötzl, J.; Roser, D.; Bankel, L.; Hömberg, N.; Geishauser, A.; Brenner, C.; Weigand, M.; Röcken, M.; Mocikat, R. Reversal of tumor acidosis by systemic buffering

- reactivates NK cells to express IFN- γ and induces NK cell-dependent lymphoma control without other immunotherapies: NK cell- and pH-dependent lymphoma suppression. *International Journal of Cancer* **2017**, *140*, doi:10.1002/ijc.30646.
252. Boivin, W.A.; Cooper, D.M.; Hiebert, P.R.; Granville, D.J. Intracellular versus extracellular granzyme B in immunity and disease: challenging the dogma. *Laboratory Investigation* **2009**, *89*, 1195-1220, doi:10.1038/labinvest.2009.91.
 253. de Armas, L.R.; Podack, E.R. Chapter Sixteen - Natural killer cytolytic activity. In *Natural Killer Cells*, Lotze, M.T., Thomson, A.W., Eds. Academic Press: San Diego, 2010; <https://doi.org/10.1016/B978-0-12-370454-2.00016-8pp>. 215-227.
 254. Zhu, D.; You, J.; Zhao, N.; Xu, H. Magnesium Regulates Endothelial Barrier Functions through TRPM7, MagT1, and S1P1. *Adv Sci (Weinh)* **2019**, *6*, 1901166-1901166, doi:10.1002/advs.201901166.
 255. Cullere, X.; Shaw, S.K.; Andersson, L.; Hirahashi, J.; Lusinskas, F.W.; Mayadas, T.N. Regulation of vascular endothelial barrier function by Epac, a cAMP-activated exchange factor for Rap GTPase. *Blood* **2005**, *105*, 1950-1955, doi:10.1182/blood-2004-05-1987.
 256. Murakami, M.; Nguyen, L.T.; Zhuang, Z.W.; Moodie, K.L.; Carmeliet, P.; Stan, R.V.; Simons, M. The FGF system has a key role in regulating vascular integrity. *J Clin Invest* **2008**, *118*, 3355-3366, doi:10.1172/jci35298.
 257. Salazar, N.; Zabel, B.A. Support of Tumor Endothelial Cells by Chemokine Receptors. *Frontiers in immunology* **2019**, *10*, 147-147, doi:10.3389/fimmu.2019.00147.
 258. Han, H.-S.; Jun, I.; Seok, H.-K.; Lee, K.-S.; Lee, K.; Witte, F.; Mantovani, D.; Kim, Y.-C.; Glyn-Jones, S.; Edwards, J.R. Biodegradable Magnesium Alloys Promote Angio-Osteogenesis to Enhance Bone Repair. *Advanced Science* **2020**, *7*, 2000800, doi:<https://doi.org/10.1002/advs.202000800>.
 259. Banai, S.; Haggroth, L.; Epstein, S.E.; Casscells, W. Influence of extracellular magnesium on capillary endothelial cell proliferation and migration. *Circ Res* **1990**, *67*, 645-650, doi:10.1161/01.res.67.3.645.
 260. Maier, J.A.; Malpuech-Brugère, C.; Zimowska, W.; Rayssiguier, Y.; Mazur, A. Low magnesium promotes endothelial cell dysfunction: implications for atherosclerosis, inflammation and thrombosis. *Biochim Biophys Acta* **2004**, *1689*, 13-21, doi:10.1016/j.bbadis.2004.01.002.
 261. Zhao, N.; Zhu, D. Endothelial responses of magnesium and other alloying elements in magnesium-based stent materials. *Metallomics : integrated biometal science* **2015**, *7*, 118-128, doi:10.1039/c4mt00244j.
 262. Liu, C.; Fu, X.; Pan, H.; Wan, P.; Wang, L.; Tan, L.; Wang, K.; Zhao, Y.; Yang, K.; Chu, P.K. Biodegradable Mg-Cu alloys with enhanced osteogenesis, angiogenesis, and long-lasting antibacterial effects. *Scientific Reports* **2016**, *6*, 27374, doi:10.1038/srep27374.
 263. Pan, S.; An, L.; Meng, X.; Li, L.; Ren, F.; Guan, Y. MgCl(2) and ZnCl(2) promote human umbilical vein endothelial cell migration and invasion and stimulate epithelial-mesenchymal transition via the Wnt/ β -catenin pathway. *Exp Ther Med* **2017**, *14*, 4663-4670, doi:10.3892/etm.2017.5144.
 264. Maier, J.A.M.; Bernardini, D.; Rayssiguier, Y.; Mazur, A. High concentrations of magnesium modulate vascular endothelial cell behaviour in vitro. *Biochimica et Biophysica Acta (BBA) - Molecular Basis of Disease* **2004**, *1689*, 6-12, doi:<https://doi.org/10.1016/j.bbadis.2004.02.004>.
 265. Gao, P.; Fan, B.; Yu, X.; Liu, W.; Wu, J.; Shi, L.; Yang, D.; Tan, L.; Wan, P.; Hao, Y., et al. Biofunctional magnesium coated Ti6Al4V scaffold enhances osteogenesis and angiogenesis in vitro and in vivo for orthopedic application. *Bioactive Materials* **2020**, *5*, 680-693, doi:<https://doi.org/10.1016/j.bioactmat.2020.04.019>.
 266. Ritch, S.J.; Brandhagen, B.N.; Goyeneche, A.A.; Telleria, C.M. Advanced assessment of migration and invasion of cancer cells in response to mifepristone therapy using double fluorescence cytochemical labeling. *BMC Cancer* **2019**, *19*, 376, doi:10.1186/s12885-019-5587-3.

References

267. Callier, V. Divide or Conquer. *Scientific American* **2016**, *314*, 17, doi:10.1038/scientificamerican0116-17.
268. Miyazaki, K.; Oyanagi, J.; Hoshino, D.; Togo, S.; Kumagai, H.; Miyagi, Y. Cancer cell migration on elongate protrusions of fibroblasts in collagen matrix. *Scientific Reports* **2019**, *9*, 292, doi:10.1038/s41598-018-36646-z.
269. Waldeland, J.O.; Polacheck, W.J.; Evje, S. Collective tumor cell migration in the presence of fibroblasts. *Journal of biomechanics* **2020**, *100*, 109568, doi:10.1016/j.jbiomech.2019.109568.
270. Roomi, M.; Monterrey, J.; Kalinovsky, T.; Rath, M.; Niedzwiecki, A. Patterns of MMP-2 and MMP-9 expression in human cancer cell lines. *Oncology reports* **2009**, *21* 5, 1323-1333.
271. Hoppner, K.J.; Matrisian, L.M.; Jensen, R.A.; Rodgers, W.H. Expression of most matrix metalloproteinase family members in breast cancer represents a tumor-induced host response. *The American journal of pathology* **1996**, *149*, 273-282.
272. Boyd, R.S.; Balkwill, F.R. MMP-2 release and activation in ovarian carcinoma: the role of fibroblasts. *British Journal of Cancer* **1999**, *80*, 315-321, doi:10.1038/sj.bjc.6690357.
273. Aoki, M.; Koga, K.; Miyazaki, M.; Hamasaki, M.; Koshikawa, N.; Oyama, M.; Kozuka-Hata, H.; Seiki, M.; Toole, B.P.; Nabeshima, K. CD73 complexes with emmprin to regulate MMP-2 production from co-cultured sarcoma cells and fibroblasts. *BMC Cancer* **2019**, *19*, 912, doi:10.1186/s12885-019-6127-x.
274. Saad, S.; Gottlieb, D.; Bradstock, K.; Overall, C.; Bendall, L. Saad S, Gottlieb DJ, Bradstock KF, Overall CM, Bendall LJ Cancer cell-associated fibronectin induces release of matrix metalloproteinase-2 from normal fibroblasts. *Cancer Res* **2002**, *62*, 283-289. *Cancer research* **2002**, *62*, 283-289.
275. Himelstein, B.P.; Canete-Soler, R.; Bernhard, E.J.; Muschel, R.J. Induction of fibroblast 92 kDa gelatinase/type IV collagenase expression by direct contact with metastatic tumor cells. *J Cell Sci* **1994**, *107* (Pt 2), 477-486.
276. Pagès, N.; Gogly, B.; Godeau, G.; Igondjo-Tchen, S.; Maurois, P.; Durlach, J.; Bac, P. Structural alterations of the vascular wall in magnesium-deficient mice. A possible role of gelatinases A (MMP-2) and B (MMP-9). *Magnesium research* **2003**, *16*, 43-48.
277. Yun, Y.; Dong, Z.; Tan, Z.; Schulz, M.J. Development of an electrode cell impedance method to measure osteoblast cell activity in magnesium-conditioned media. *Analytical and Bioanalytical Chemistry* **2010**, *396*, 3009-3015, doi:10.1007/s00216-010-3521-2.
278. Martínez-Zaguilán, R.; Seftor, E.A.; Seftor, R.E.B.; Chu, Y.-W.; Gillies, R.J.; Hendrix, M.J.C. Acidic pH enhances the invasive behavior of human melanoma cells. *Clin Exp Metastasis* **1996**, *14*, 176-186, doi:10.1007/BF00121214.
279. Razaq, S.; Wilkins, R.J.; Urban, J.P.G. The effect of extracellular pH on matrix turnover by cells of the bovine nucleus pulposus. *European spine journal : official publication of the European Spine Society, the European Spinal Deformity Society, and the European Section of the Cervical Spine Research Society* **2003**, *12*, 341-349, doi:10.1007/s00586-003-0582-3.
280. Amberg, R.; Elad, A.; Beuer, F.; Vogt, C.; Bode, J.; Witte, F. Effect of physical cues of altered extract media from biodegradable magnesium implants on human gingival fibroblasts. *Acta Biomater* **2019**, *98*, 186-195, doi:10.1016/j.actbio.2019.07.022.
281. Zan, R.; Ji, W.; Qiao, S.; Wu, H.; Wang, W.; Ji, T.; Yang, B.; Zhang, S.; Luo, C.; Song, Y., et al. Biodegradable magnesium implants: a potential scaffold for bone tumor patients. *Science China Materials* **2020**, 10.1007/s40843-020-1509-2, doi:10.1007/s40843-020-1509-2.
282. Santos, J.; Hussain, F. Magnesium Chloride increases apoptosis and decreases prostate cancer cells migration. *Functional Foods in Health and Disease* **2018**, *8*, 62-78, doi:10.31989/ffhd.v8i1.368.
283. Estrella, V.; Chen, T.; Lloyd, M.; Wojtkowiak, J.; Cornnell, H.H.; Ibrahim-Hashim, A.; Bailey, K.; Balagurunathan, Y.; Rothberg, J.M.; Sloane, B.F., et al. Acidity generated by the tumor microenvironment drives local invasion. *Cancer Res* **2013**, *73*, 1524-1535, doi:10.1158/0008-5472.Can-12-2796.

284. El-Kenawi, A.; Gatenbee, C.; Robertson-Tessi, M.; Bravo, R.; Dhillon, J.; Balagurunathan, Y.; Berglund, A.; Vishvakarma, N.; Ibrahim-Hashim, A.; Choi, J., et al. Acidity promotes tumour progression by altering macrophage phenotype in prostate cancer. *British Journal of Cancer* **2019**, *121*, 556-566, doi:10.1038/s41416-019-0542-2.
285. Robey, I.F.; Baggett, B.K.; Kirkpatrick, N.D.; Roe, D.J.; Dosesco, J.; Sloane, B.F.; Hashim, A.I.; Morse, D.L.; Raghunand, N.; Gatenby, R.A., et al. Bicarbonate increases tumor pH and inhibits spontaneous metastases. *Cancer Res* **2009**, *69*, 2260-2268, doi:10.1158/0008-5472.Can-07-5575.
286. Ibrahim Hashim, A.; Cornnell, H.H.; Coelho Ribeiro Mde, L.; Abrahams, D.; Cunningham, J.; Lloyd, M.; Martinez, G.V.; Gatenby, R.A.; Gillies, R.J. Reduction of metastasis using a non-volatile buffer. *Clin Exp Metastasis* **2011**, *28*, 841-849, doi:10.1007/s10585-011-9415-7.
287. Friedl, P.; Alexander, S. Cancer invasion and the microenvironment: plasticity and reciprocity. *Cell* **2011**, *147*, 992-1009, doi:10.1016/j.cell.2011.11.016.
288. Mogilner, A.; Oster, G. Cell motility driven by actin polymerization. *Biophys J* **1996**, *71*, 3030-3045, doi:10.1016/s0006-3495(96)79496-1.
289. Pollard, T.D.; Borisy, G.G. Cellular motility driven by assembly and disassembly of actin filaments. *Cell* **2003**, *112*, 453-465, doi:10.1016/s0092-8674(03)00120-x.
290. Stroka, K.M.; Jiang, H.; Chen, S.-H.; Tong, Z.; Wirtz, D.; Sun, S.X.; Konstantopoulos, K. Water permeation drives tumor cell migration in confined microenvironments. *Cell* **2014**, *157*, 611-623, doi:10.1016/j.cell.2014.02.052.
291. Bisi, S.; Disanza, A.; Malinverno, C.; Frittoli, E.; Palamidessi, A.; Scita, G. Membrane and actin dynamics interplay at lamellipodia leading edge. *Current Opinion in Cell Biology* **2013**, *25*, 565-573, doi:<https://doi.org/10.1016/j.ceb.2013.04.001>.
292. Papadopoulos, M.C.; Saadoun, S. Key roles of aquaporins in tumor biology. *Biochimica et Biophysica Acta (BBA) - Biomembranes* **2015**, *1848*, 2576-2583, doi:<https://doi.org/10.1016/j.bbamem.2014.09.001>.
293. Feyerabend, F.; Fischer, J.; Holtz, J.; Witte, F.; Willumeit, R.; Drücker, H.; Vogt, C.; Hort, N. Evaluation of short-term effects of rare earth and other elements used in magnesium alloys on primary cells and cell lines. *Acta Biomaterialia* **2010**, *6*, 1834-1842, doi:<https://doi.org/10.1016/j.actbio.2009.09.024>.
294. Gao, S.; Chen, D.; Li, Q.; Ye, J.; Jiang, H.; Amatore, C.; Wang, X. Near-infrared fluorescence imaging of cancer cells and tumors through specific biosynthesis of silver nanoclusters. *Scientific Reports* **2014**, *4*, 4384, doi:10.1038/srep04384.
295. Franco-Molina, M.A.; Mendoza-Gamboa, E.; Sierra-Rivera, C.A.; Gomez-Flores, R.A.; Zapata-Benavides, P.; Castillo-Tello, P.; Alcocer-Gonzalez, J.M.; Miranda-Hernandez, D.F.; Tamez-Guerra, R.S.; Rodriguez-Padilla, C. Antitumor activity of colloidal silver on MCF-7 human breast cancer cells. *J Exp Clin Cancer Res* **2010**, *29*, 148, doi:10.1186/1756-9966-29-148.
296. Wolf, F.I.; Cittadini, A.R.; Maier, J.A. Magnesium and tumors: ally or foe? *Cancer Treat Rev* **2009**, *35*, 378-382, doi:10.1016/j.ctrv.2009.01.003.
297. Anghileri, L.J. Magnesium, calcium and cancer. *Magnesium research* **2009**, *22*, 247-255, doi:10.1684/mrh.2009.0173.
298. Koppenol, W.H.; Bounds, P.L.; Dang, C.V. Otto Warburg's contributions to current concepts of cancer metabolism. *Nat Rev Cancer* **2011**, *11*, 325-337, doi:10.1038/nrc3038.
299. Gunther, T. Comment on the number of Mg²⁺-activated enzymes. *Magnesium research* **2008**, *21*, 185-187.
300. Clapham, D.E. Calcium Signaling. *Cell* **2007**, *131*, 1047-1058, doi:<https://doi.org/10.1016/j.cell.2007.11.028>.
301. Pereira, M.; Millot, J.-M.; Sebille, S.; Manfait, M. Inhibitory effects of extracellular Mg²⁺ on intracellular Ca²⁺ dynamic changes and thapsigargin-induced apoptosis in human cancer MCF7 cells. *Molecular and Cellular Biochemistry* **2002**, *229*, 163-171, doi:10.1023/A:1017972622312.

References

302. Gerweck, L.E.; Kozin, S.V.; Stocks, S.J. The pH partition theory predicts the accumulation and toxicity of doxorubicin in normal and low-pH-adapted cells. *Br J Cancer* **1999**, *79*, 838-842, doi:10.1038/sj.bjc.6690134.
303. Raghunand, N.; He, X.; van Sluis, R.; Mahoney, B.; Baggett, B.; Taylor, C.W.; Paine-Murrieta, G.; Roe, D.; Bhujwala, Z.M.; Gillies, R.J. Enhancement of chemotherapy by manipulation of tumour pH. *Br J Cancer* **1999**, *80*, 1005-1011, doi:10.1038/sj.bjc.6690455.
304. Damen, M.P.F.; van Rheenen, J.; Scheele, C.L.G.J. Targeting dormant tumor cells to prevent cancer recurrence. *The FEBS Journal* *n/a*, doi:<https://doi.org/10.1111/febs.15626>.
305. Pajic, M.; Blatter, S.; Guyader, C.; Gonggrijp, M.; Kersbergen, A.; Küçükosmanoğlu, A.; Sol, W.; Drost, R.; Jonkers, J.; Borst, P., et al. Selected Alkylating Agents Can Overcome Drug Tolerance of G(0)-like Tumor Cells and Eradicate BRCA1-Deficient Mammary Tumors in Mice. *Clin Cancer Res* **2017**, *23*, 7020-7033, doi:10.1158/1078-0432.ccr-17-1279.
306. Davies, C.; Pan, H.; Godwin, J.; Gray, R.; Arriagada, R.; Raina, V.; Abraham, M.; Medeiros Alencar, V.H.; Badran, A.; Bonfill, X., et al. Long-term effects of continuing adjuvant tamoxifen to 10 years versus stopping at 5 years after diagnosis of oestrogen receptor-positive breast cancer: ATLAS, a randomised trial. *Lancet* **2013**, *381*, 805-816, doi:10.1016/s0140-6736(12)61963-1.
307. Luthringer, B.J.; Feyerabend, F.; Willumeit-Römer, R. Magnesium-based implants: a mini-review. *Magnesium research* **2014**, *27*, 142-154, doi:10.1684/mrh.2015.0375.
308. Tie, D.; Feyerabend, F.; Mueller, W.-D.; Schade, R.; Liefeith, K.; Kainer, K.; Willumeit, R. Antibacterial biodegradable Mg-Ag alloys. *European cells & materials* **2013**, *25*, 284-298, doi:10.22203/eCM.v025a20.

List of Figures

Figure 1. Cancer progression to organ failure.....	5
Figure 2. Main proliferation signaling pathways.....	7
Figure 3. Different energy production of cancer cells and differentiated tissue..	8
Figure 4. Mechanisms of cancer cell evasion from NK cells.....	11
Figure 5. “The complex context of tumor microenvironment”, by Roma-Rodrigues <i>et al.</i> [154], licensed under CC BY 4.0. More on https://creativecommons.org/licenses/by/4.0/	12
Figure 6. Basic set-up of AAS to measure Mg content in the supernatant.....	18
Figure 7. Basic set-up of ICP-MS to measure Mg and Ag content simultaneously in the supernatant.....	20
Figure 8. Principle of the color reaction to measure LDH content.....	21
Figure 9. Illustration of live and dead cell discrimination by flow cytometry.....	22
Figure 10. Schematic illustration of the different Ki-67 expression during the cell cycle.....	23
Figure 11. Procedures of two sandwich ELISA.....	24
Figure 12. Procedure of the scratch assay.....	27
Figure 13. 3D cell invasion assay.....	27
Figure 14. Conditioned media preparation and application.....	30
Figure 15. Procedure to measure endothelial cell permeability.....	31
Figure 16. Principle to measure the tube formation ability of endothelial cells.....	32
Figure 17. Cell viability of Saos-eGFP and RF Fibroblasts on Mg-based materials.....	34
Figure 18. Mean degradation rate, pH and osmolality on material with and without cells.....	35
Figure 19. Magnesium and silver concentrations in the supernatant of degrading Mg and Mg-6Ag.....	35
Figure 20. Cytotoxicity of Mg-based materials towards the osteosarcoma-fibroblast coculture under normoxia.....	37
Figure 21. Oxidative stress and apoptosis in response to Mg-based material degradation.....	38
Figure 22. The influence of Mg and Mg-6Ag on Ki-67 expression in the coculture.....	40
Figure 23. Reversibility of the cancer cell associated dormancy-like phenotype.....	41
Figure 24. The effect of protein kinase RNA-like endoplasmic reticulum kinase (PERK) inhibition on cancer cell proliferation.....	42
Figure 25. Measurement of IL-8 and phosphorylated SMAD2/SMAD3 complex concentrations.....	43
Figure 26. Single parameters of Mg degradation influencing cell viability.....	44
Figure 27. Influence of single parameters of Mg degradation on cell proliferation.....	45
Figure 28. Cell migration in response to Mg-based materials.....	47
Figure 29. Cell invasion through an ECM gel matrix in response to Mg-based materials.....	48
Figure 30. Quantification of invaded cells in response to Mg-based materials after 72 h.....	49
Figure 31. Quantification of metastases-associated cytokines in the supernatant.....	50
Figure 32. Cell migration in response to single parameters of Mg degradation.....	52
Figure 33. Influence of natural killer cells on coculture cell numbers on Mg-based materials.....	53
Figure 34. Supernatant granzyme B concentration during incubation of the coculture with natural killer cells.....	55
Figure 35. Supernatant perforin concentration during incubation of the coculture with natural killer cells.....	56
Figure 36. Permeability of endothelial cells incubated with conditioned medium.....	58
Figure 37. Proliferation of HUVEC incubated with conditioned medium.....	59
Figure 38. Quantification of VEGF in the supernatant of endothelial cells.....	60
Figure 39. Migration of endothelial cells incubated with conditioned medium.....	61

References

Figure 40. Endothelial cell tube formation in response to conditioned medium.	62
Figure 41. MDR of Mg-6Ag T6 heat treatment for 7-15 min at 200 °C.	63
Figure 42. Differences of pH and osmolality values of T6 treated and untreated (UT) Mg-6Ag..	64
Figure 43. Cell viability of Mg-6Ag T6 heat-treated samples.	65
Figure 44. Summary of the impact of Mg-based materials on selected cancer hallmarks.	74
Figure S1. Mg-6Ag T6 heat treatment for 2-20 h at 320 °C.....	98
Figure S2. Mg-6Ag T6 heat treatment for 2 h at 200-300 °C.....	99
Figure S3. Mg-6Ag T6 heat treatment for 5-60 min at 200 °C.....	100
Figure S4. Cell viability of Saos-eGFP and RF Fibroblasts under increasing Mg and Ag concentrations.....	101
Figure S5. Magnesium silver concentrations in the supernatant of fast-degrading Mg-6Ag..	102
Figure S6. Cell viability of Saos-eGFP and RF Fibroblasts under increasing Mg and Ag concentrations.....	103

List of Tables

Table 1. Overview of analyses and corresponding used materials.....	15
Table 2. Chemical analyses of the used Mg and Mg-6Ag materials.....	16
Table 3. Used cell lines and specifications.	16
Table 4. Flame AAS parameters	19
Table 5. Excitation and emission wavelengths for ROS and caspase-3 visualization in the coculture.....	22
Table 6. Excitation and emission wavelengths for Ki-67 visualization in the coculture.	24
Table 7. ELISA types to quantify IL-8 and P-SMAD2/SMAD3.....	25
Table 8. ELISA types to quantify MMP-2, MMP-9, and TIMP-1.	28
Table 9. ELISA types to quantify granzyme B and perforin.	29
Table 10. Concentration of Mg, osmolality and pH of single parameter solutions in comparison to the glass control (cell culture medium), and degrading Mg discs.	44
Table 11. Supernatant Mg concentration (in mM) in conditioned media.....	57

Appendix

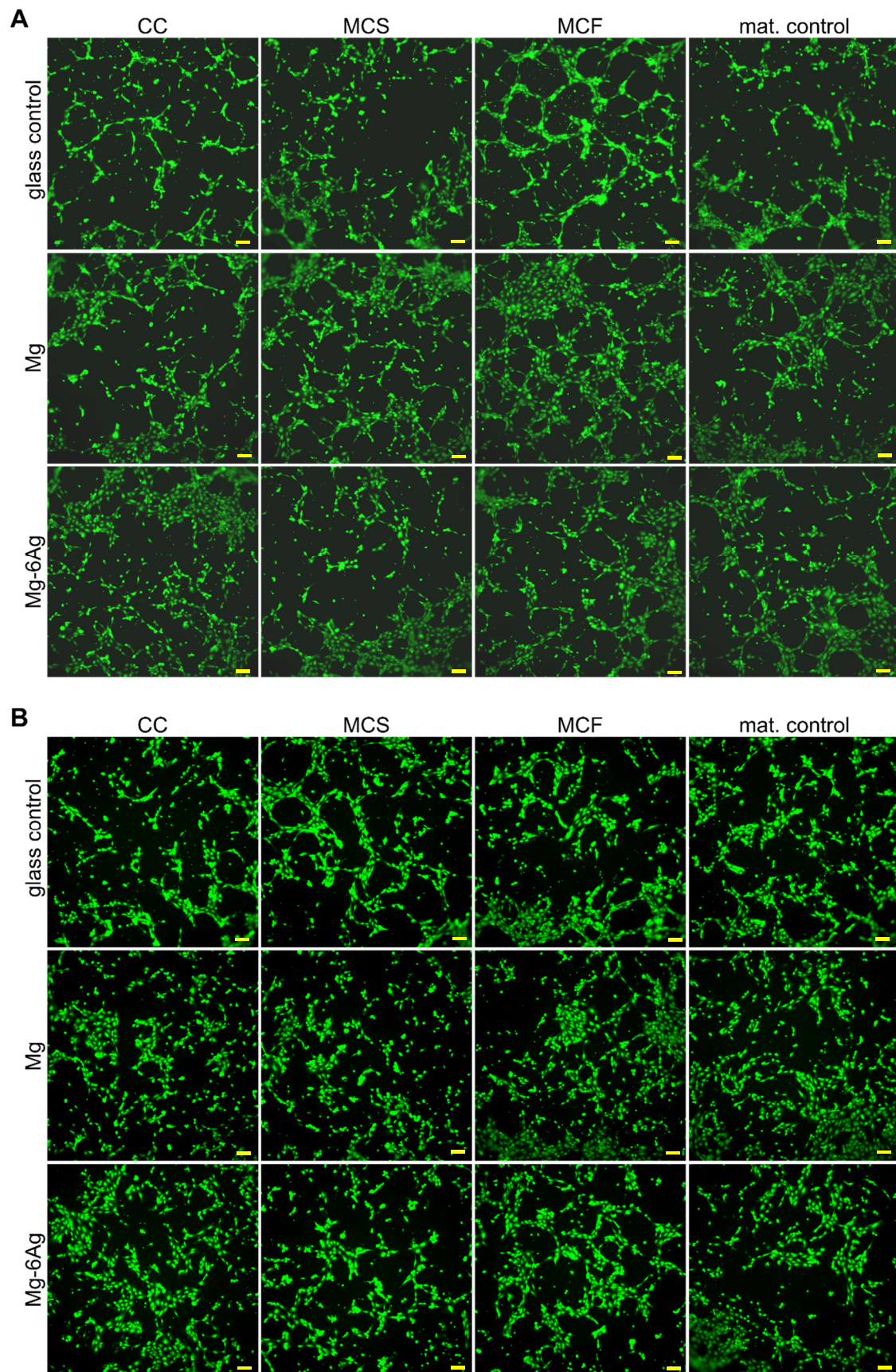


Figure S1. HUVEC form tube-like structures on basement membrane. HUVEC under (A) normoxia and (B) hypoxia were stained with calcein-AM 6 h after seeding. Scale bar is 100 μm .

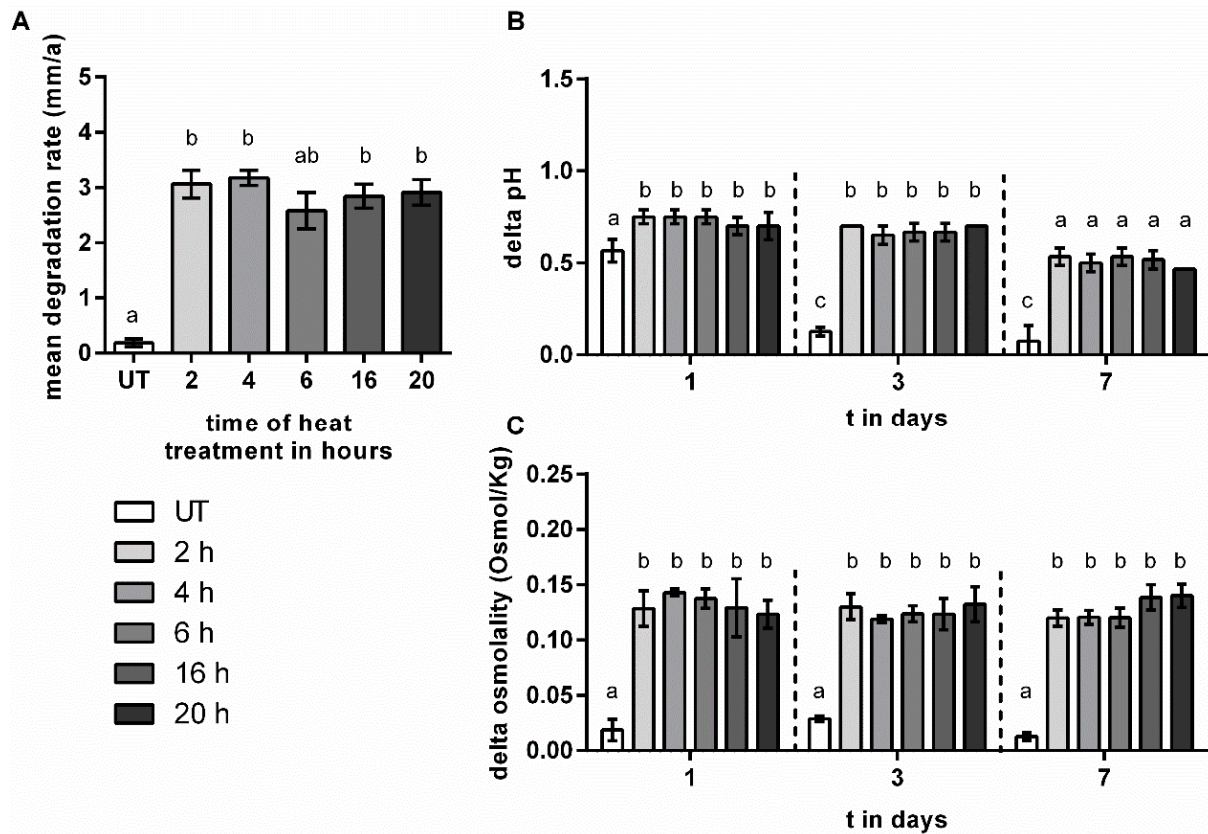


Figure S2. Mg-6Ag T6 heat treatment for 2-20 h at 320 °C. (A) Determination of MDR after seven days and differences of (B) pH and (C) osmolality values of T6 treated and untreated (UT) Mg-6Ag. Delta pH and osmolality values represent the difference between T6 treated samples and medium and were calculated as described in chapter 3.3. All three parameters are presented as the mean \pm SD from one experiment with six samples each. Bars with a different lowercase letters showed statistically significant differences obtained via a two-way ANOVA with Tukey's multiple comparison test ($n=6$). Same letter = $p < 0.05$.

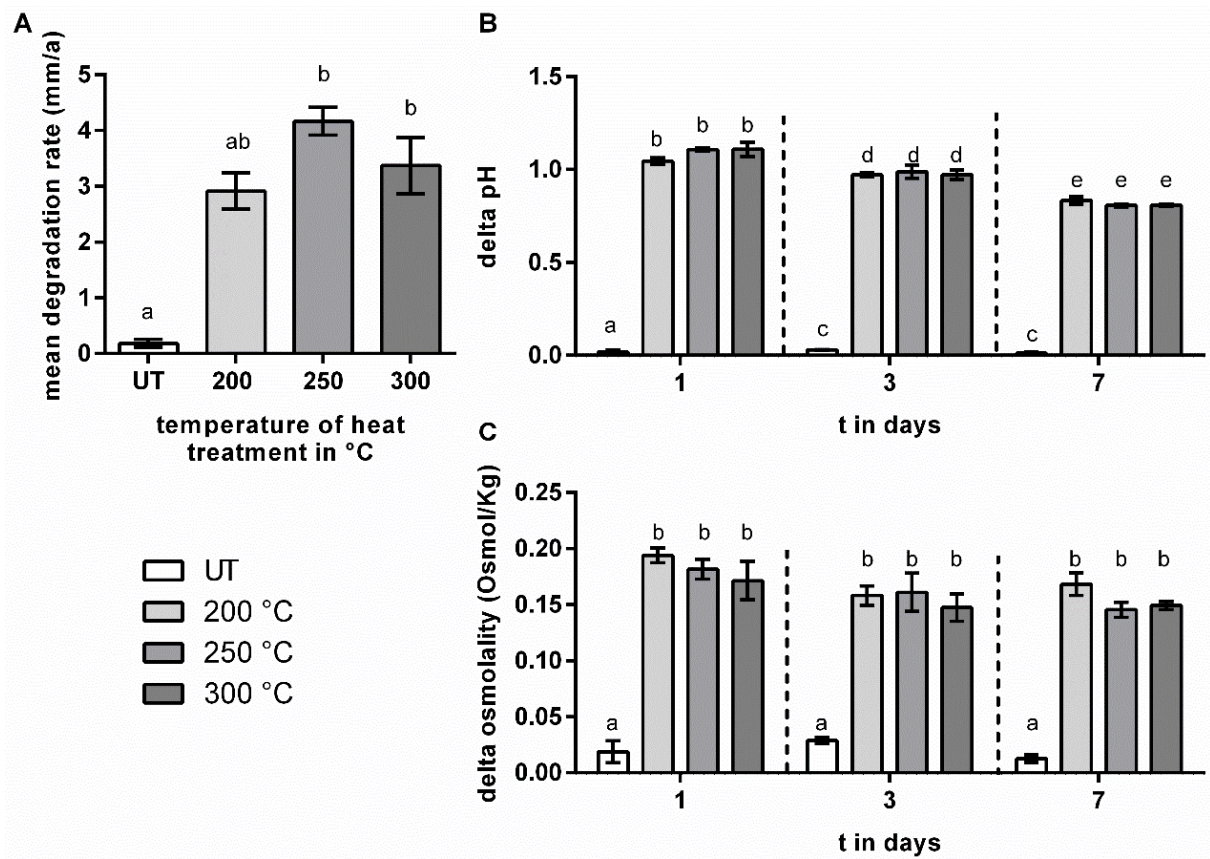


Figure S3. Mg-6Ag T6 heat treatment for 2 h at 200-300 °C. (A) Determination of MDR after seven days and differences of (B) pH and (C) osmolality values of T6 treated and untreated (UT) Mg-6Ag. Delta pH and osmolality values represent the difference between T6 treated samples and medium and were calculated as described in chapter 3.3. All three parameters are presented as the mean \pm SD from one experiment with six samples each. Bars with a different lowercase letters showed statistically significant differences obtained via a two-way ANOVA with Tukey's multiple comparison test ($n=6$). Same letter = $p < 0.05$.

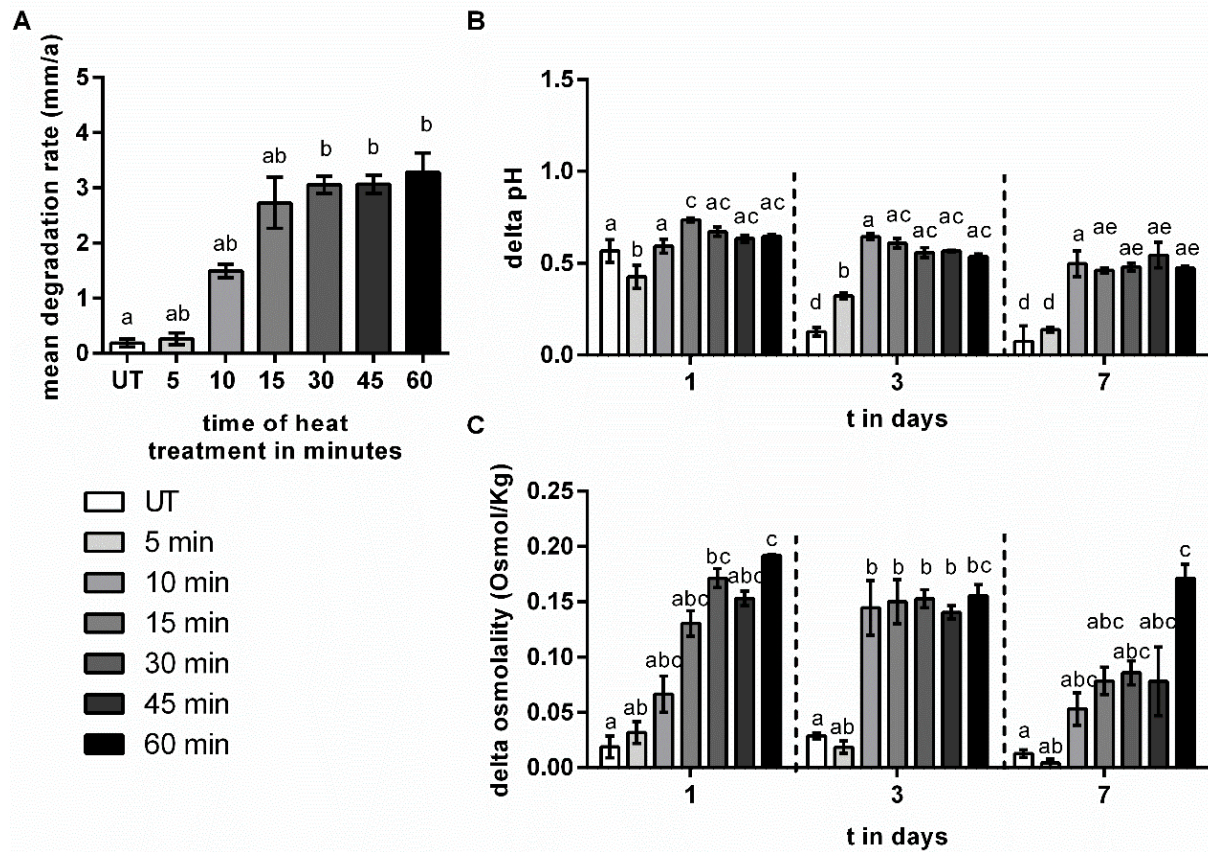


Figure S4. Mg-6Ag T6 heat treatment for 5-60 min at 200 °C. (A) Determination of MDR after seven days and differences of (B) pH and (C) osmolality values of T6 treated and untreated (UT) Mg-6Ag. Delta pH and osmolality values represent the difference between T6 treated samples and medium and were calculated as described in chapter 3.3. All three parameters are presented as the mean \pm SD from one experiment with six samples each. Bars with a different lowercase letters showed statistically significant differences obtained via a two-way ANOVA with Tukey's multiple comparison test ($n=6$). Same letter = $p < 0.05$.

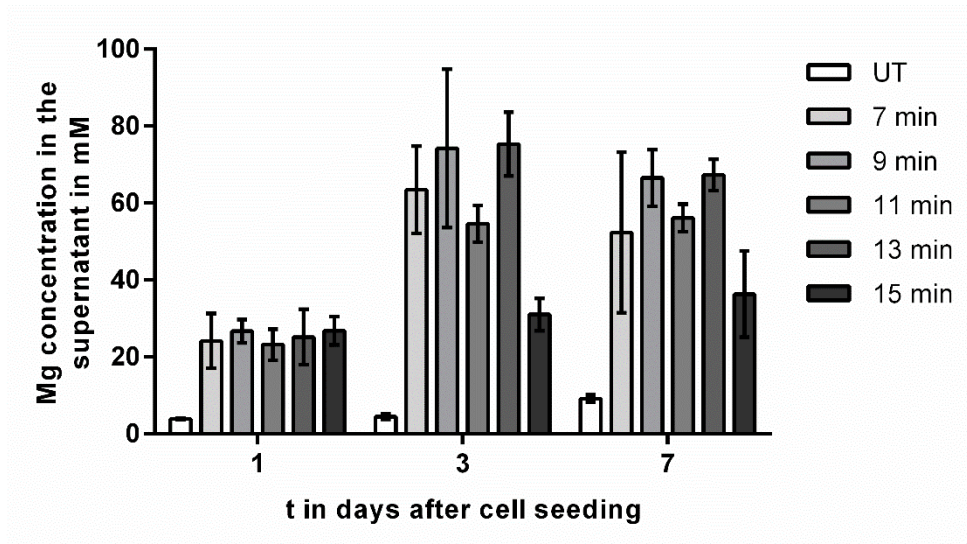


Figure S5. Magnesium silver concentrations in the supernatant of fast-degrading Mg-6Ag. Supernatant Mg concentration resulting from Mg-6Ag degradation was quantified by AAS. Resulting supernatant concentrations of Mg are presented as the mean \pm SD. Statistically significant differences between concentrations at the indicated time points were obtained via a Kruskal-Wallis H test with Dunn's multiple comparison test ($n=3$).

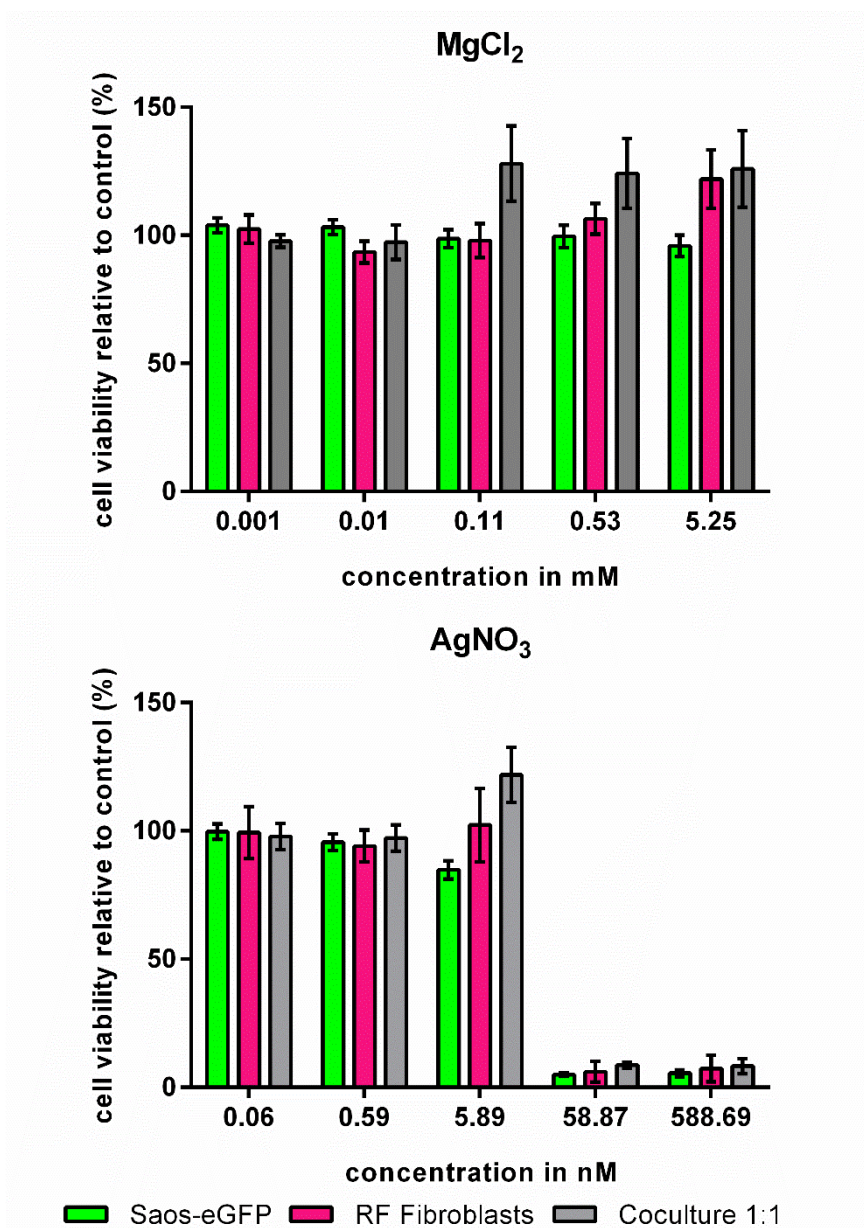


Figure S6. Cell viability of Saos-eGFP and RF Fibroblasts under increasing Mg and Ag concentrations. Tumor and healthy cells were seeded into 96-well plates and allowed to adhere. Then, MgCl₂ and AgNO₃ solutions with indicated concentrations were prepared in cell culture medium and added to the cells. After seven days, medium was aspirated and fresh medium with MTT (1:10 ratio) was added for 4 h at 37 °C. Then, sodium dodecyl sulfate (SDS) was added (1:1 ratio) and incubated over night at 37 °C. The absorbance was measured with a plate reader (Sunrise™ Tecan microplate reader; Tecan, Männedorf, Switzerland) at a wavelength of 570 nm with a reference wavelength of 655 nm.

Appendix

List of hazardous substances

Name	GHS	Hazard statements	Precautionary statements
2-[4-(2,4,4-trimethylpentan-2-yl)phenoxy]ethanol (Triton-X 100)	GHS05	302-318-411	273-280-305+351+338
3,3',5,5'-Tetramethylbenzidin (TMB)	GHS07	315-319-335	261-305+351+338
Acetone	GHS02, GHS07	225-319-336	210-240-305+351+338-403+233
Bisbenzimidazole	GHS05, GHS07	302-314-335	261-280-305+351+338-310
Chloroform	GHS06, GHS08	302-331-315-319-351-361d-336-372	261-281-305+351+338-311
Chromic acid	GHS03, GHS05, GHS06, GHS08, GHS09	271-301+311-330-314-317-334-335-340-350-361f-372-410	221-283-301+310-303+361+353-305+351+338-310-320-405-501
Crystal violet	GHS05, GHS07, GHS08, GHS09	302-318-351-410	273-280-305+351+338
Ethanol	GHS02, GHS07	225-319	210-240-305+351+338-403+233
Hydrochloric acid	GHS05, GHS07	290-314-335	280-303+361+353-305+351+338+310
Hydrogen peroxide	GHS03, GHS05, GHS07	271-302-314-332-335-412	280-305+351+338-310
Menadione	GHS07	302-315-319-335	261-305+351+338
Mitomycin c	GHS06, GHS08	300-351	270-280-301+310-405
n-hexane	GHS02, GHS07, GHS06, GHS09	225-304-361f-373-315-336-411	210-240-273-301+310-331-302+352-403+235
Nitric acid	GHS03, GHS05, GHS06	272-290-314-331	221-280-303+361+353-304+340-305+351+338-310
Paraformaldehyde	GHS02, GHS05, GHS07, GHS08	228-302+332-315-317-318-335-350	201-210-280-302+352-305+351+338

Sodium hydroxide	GHS05	290-314	280-301+330+331-305+351+338-308+310
Sodium hypochlorite	GHS05, GHS09	290-314-410	260-273-280-301+330+331-303+361+353-305+351+338-310-501
Sulfuric acid	GHS05	290-314	280-301+330+331-303+361+353-305+351+338+310

Danksagung

Ich möchte an dieser Stelle allen Beteiligten einen großen Dank aussprechen, die mich während meiner Promotionszeit und der Anfertigung der Doktorarbeit unterstützt haben.

Zuallererst gilt mein ganz besonderer Dank Prof. Dr. Regine Willumeit-Römer nicht nur für die Möglichkeit in ihrem Institut zu arbeiten, sondern auch für die exzellente wissenschaftliche Betreuung am Helmholtz Zentrum Hereon.

Weiterhin bedanke ich mich sehr bei Prof. Dr. Hartmut Schlüter für die Betreuung, die Einwilligung ein Gutachten für diese Arbeit zu erstellen und als Ansprechpartner an der Universität Hamburg.

Auch Dr. Bérengère Luthringer-Feyerabend möchte ich meinen Dank für die praktische Betreuung aussprechen. Neben intensiven fachlichen Diskussionen konnte sie so manch aufmunternde Worte finden.

Zudem möchte ich mich bei allen Mitarbeitern des Instituts für Metallische Biomaterialien für Hilfestellungen und wertvolle Hinweise bedanken. Bei Dr. Heike Helmholtz möchte ich mich für Denkanstöße und die AAS Messungen bedanken. Dr. Katharina Philipp und Annette Havelberg danke ich für administrative und moralische Unterstützungen. Bei Monika Luczak, Anke Schuster, Nils Holländer und Melina Mohrdick möchte ich mich für die Unterstützung im Labor, die wertvollen Tipps und das angenehme Arbeitsklima bedanken.

Diese Arbeit entstand im Rahmen einer „Helmholtz-RSF Joint Research Group“, einer Kooperation der Helmholtz-Gemeinschaft und der Russian Science Foundation (RSF), bei denen ich mich für die finanzielle Unterstützung bedanken möchte. Weiter möchte ich mich bei den folgenden Wissenschaftlern dieser Kooperation vom NUST MISIS und N.N. Blokhin Russian Cancer Research Center aus Moskau für die informativen Diskussionen, anregende Kooperation und Gastfreundschaft bedanken: Prof. Dr. Yuri Estrin, Prof. Dr. Boris Straumal, Prof. Dr. Sergey Dobatkin, Prof. Dr. Mikhail Kiselevsky, Dr. Natalia Anisimova und Dr. Natalia Martynenko. Von der Seite des Helmholtz Zentrums Hereon möchte ich in diesem Zusammenhang nebst vorgenannten auch Dr. Thomas Ebel, Dr. Björn Wiese und Khausik Narasimhan meinen Dank für die Zusammenarbeit aussprechen.

Neben der fachlichen Unterstützung durch Betreuer und Mitarbeiter möchte ich an dieser Stelle auch die Unterstützung durch Freunde und Familie hervorheben. Ich danke meinen Freunden Ferdinand, Konstantin, Lucas, Johannes, sowie Ben und Henrik. Bei meiner gesamten Familie, insbesondere bei meinen Eltern Ricarda Globig und Ralf Globig, sowie bei meiner Schwester Stephanie Globig bedanke ich mich für die bedingungslose Rückhalt während meiner Studienzeit und darüber hinaus. Zuletzt möchte ich mich auch bei meiner besseren Hälfte Reneé Unbehau bedanken, die selbst auch in dieser Situation war und mich durch ihre fachliche Hilfe, Geduld und Motivation immer unterstützt hat.

Eidesstattliche Versicherung / Declaration on oath

Hiermit versichere ich an Eides statt, die vorliegende Dissertation selbst verfasst und keine anderen als die angegebenen Hilfsmittel benutzt zu haben. Die eingereichte schriftliche Fassung entspricht der auf dem elektronischen Speichermedium. Ich versichere, dass diese Dissertation nicht in einem früheren Promotionsverfahren eingereicht wurde.

Hamburg, den|City, date

Unterschrift|Signature